Chair of Ceramics

Doctoral Thesis

Simulation of refractory wear by melts and calculation of wear parameters

Jeronimo Guarco

September 2022

MONTANUNIVERSITÄT LEOBEN
www.unileoben.ac.at

AFFIDAVIT

I declare on oath that I wrote this thesis independently, did not use other than the specified sources and aids, and did not otherwise use any unauthorized aids.

I declare that I have read, understood, and complied with the guidelines of the senate of the Montanuniversität Leoben for "Good Scientific Practice".

Furthermore, I declare that the electronic and printed version of the submitted thesis are identical, both, formally and with regard to content.

Date 19.09.2022

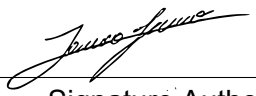

Signature Author
Jeronimo Guarco

ACKNOWLEDGMENTS

This work is the output of my research activities at K1-MET and the Chair of Ceramics, Montanuniversität Leoben. I thankfully acknowledge the financial support from the K1-MET competence center under the scope of the project “Continuous refractory wear” and likewise the financial support from the K2 Center “Integrated Computational Material, Process and Product Engineering (IC-MPPE)” under the scope of the project “Fundamentals of refractory corrosion – advanced testing methods and evaluation procedures”.

Firstly, I would like to express my gratitude to my supervisor Prof. Dr. Harald Harmuth not only for providing me the opportunity to conduct my doctoral studies in Leoben but also for the continuous support, expert guidance, and fruitful discussions that shaped this work. I especially want to thank him for his detailed revisions and for allowing me to follow my mathematical inclinations.

I am grateful to my colleagues in the Chair of Ceramics, especially project manager Dr. Sandra Vollmann for her support and the discussions and Dr. Burhanuddin for conducting the experiments that support this thesis and helping me navigate the world of ceramics.

I also want to thank my family and friends from around the world who have always believed in me and listened to me patiently talk about my work.

KURZFASSUNG

Diese Arbeit beschäftigt sich mit der Simulation von Lösungskorrosion und Erosion von feuerfesten Baustoffen durch Schmelzen und mit der Berechnung von Verschleißparametern. Die experimentelle Grundlage bildet das Fingertest-Experiment, wobei ein hochmodernes Gerät verwendet wird. Dieses ermöglicht die Vermessung der Probenoberfläche bei Prüftemperaturen mittels Laser. Die Lasermessung der verschlissenen Probenoberfläche liefert die Erosions-/Korrosionsprofile, die für die Modellvalidierung und inverse Berechnung der Verschleißparameter verwendet werden. Strömungssimulation (Computational Fluid Dynamics) wird zur Berechnung des durch die Rotation der Probe in der Schmelze induzierten Strömungsfeldes eingesetzt. Das erstellte Modell für die Lösungskorrosion stellt eine Verbesserung zur Literatur dar, da es den Effekt der Stefan-Geschwindigkeit auf die effektive Diffusionsgrenzschichtdicke und den konvektiven Anteil des Stoffstroms berücksichtigt. Darüber hinaus wird auf Basis der Grenzschichttheorie ein asymptotischer Ansatz für große Schmidt-Zahlen verwendet, um den Rechenaufwand im Modell zu reduzieren. Das Modell wurde erfolgreich mittels dokumentierten Stofftransportgleichungen verifiziert und durch Vergleich mit den Fingertest-Experimenten validiert. Die Bestimmung der effektiven binären Diffusionskoeffizienten wurde durch zwei Methoden durchgeführt: aus der experimentellen durchschnittlichen Stoffstromdichte und durch Kurvenanpassung der simulierten Auflösungskurven an die experimentelle. Die Ergebnisse stimmten mit den in der Literatur präsentierten Ergebnissen sowie mit weiteren überein, die unabhängig von den hier durchgeführten Experimenten durch in-situ Schmelzversuche mit dem konfokalen Laserscanningmikroskop und zugehöriger Hochtemperaturkammer durchgeführt wurden. Das Modell für Erosion feuerfester Baustoffe berücksichtigt die zeitliche Änderung der Probengeometrie, das Ergebnis ist ein simuliertes Erosionsprofil. Das verwendete Erosionsgesetz ist eine Funktion der Wandschubspannung und beruht auf einer Analogie zur Bodenerosion. Ein inverses Berechnungsverfahren zur Bestimmung der Erosionsparameter wurde programmiert und zunächst mit künstlich erzeugten Erosionsprofilen getestet. Das Testproblem zeigte die Durchführbarkeit einer inversen Berechnung mit einem zweiparametrigen Erosionsgesetz. Anschließend wurde das inverse Problem erfolgreich zur Berechnung der Erosionsparameter bei der Erosion einer grobkeramischen Feuerfestprobe aus Aluminiumoxid angewendet.

ABSTRACT

This work focuses on simulation of dissolution and erosion of refractory materials by melts and on calculation of wear parameters. The experimental basis is given by the finger-test experiment for which a state-of-the-art device is used. Laser scanning of the worn surface of the sample after the experimental steps provides the erosion/corrosion profiles used for model validation and inverse calculation of wear parameters. Computational fluid dynamics is employed for resolution of the flow-field induced by the rotation of the sample in the melt. The dissolution model represents an improvement to the literature because it includes the effect of the Stefan velocity in the species boundary layer thickness and the convective part of the dissolution mass flux. Moreover, an asymptotic boundary layer approach for large Schmidt numbers is employed for reducing the computational needs in the model. The model was successfully verified against documented mass transfer equations and validation was obtained by comparison with the finger-test experiments. The determination of effective binary diffusivity was conducted by two methods: from the experimental average mass flux density and by curve fitting of the simulated dissolution curves to the experimental one. The results agreed with results presented in the literature and to those derived independently by confocal laser microscopical investigations. The model for refractory erosion accounts for the change of the sample geometry with time and the simulation output is a simulated erosion profile. The erosion law was a function of the wall shear stress and was based on an analogy between refractories and soils. An inverse calculation procedure for determination of the erosion parameters was programmed and tested firstly with artificially generated erosion profiles. The test-problem revealed the feasibility of inverse calculation with a two-parameter erosion law. Later, the inverse problem was successfully applied for inverse calculation of the erosion parameters in the erosion of an alumina coarse grain refractory sample.

Contents

Table of figures

1 Problem definition

Refractories are an essential component in pyroprocessing and are thus exposed to very harsh conditions that cause wear. This wear is frequently associated to process costs and safety issues, and furthermore, it can have an impact on the quality of the product; therefore, investigations of refractory wear are essential.

Refractory wear can be classified as of continuous type, where a material mass loss vs. time representation shows a continuous function, or it can also be of discontinuous type, where the former is not observed. This work addresses refractory wear by melts, and two continuous wear mechanisms are considered, namely dissolution and erosion.

For dissolution, many quantitative studies can be found in the literature; in many of them, the evaluation methods are lacking. This can be due to an unfitting computation of the species boundary layer thickness due to the employment of approximated equations for geometries that do not exactly match the experimental set-up investigated. It can also ow to lacking consideration of dissolution-related phenomena such as the effect of the Stefan velocity on the boundary layer thickness and accounting for large Schmidt numbers. These can lead to poor estimation of diffusivities or other dissolution related parameters.

On the other hand, erosion has been mostly studied on a qualitative basis from service conditions, but no sound quantitative methods have been presented in the literature. The aim of this work is to develop simulation models in continuous refractory wear and evaluation methods for calculation of relevant wear parameter for the particular case.

2 Introduction

Both erosion and dissolution of refractory materials are mechanisms of continuous wear by melts. The dissolution of refractory materials is very frequently dominated by the species diffusion in the liquid [1]–[3]. On the other hand, the erosion occurs by grain detachment as a result of the shear stresses that the flow field exercises on the sample. This process generally necessitates a preconditioning corrosion by the infiltrated liquid. Figure 1 presents a schematic description of the aforementioned processes.

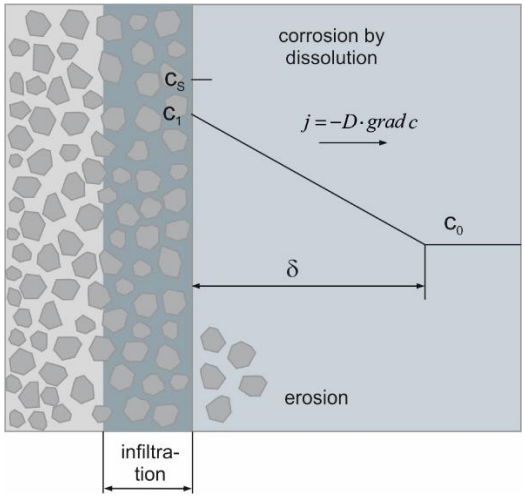

Figure 1. Schematic representation of wear mechanisms of refractories

This thesis deals with simulations of both dissolution and erosion processes. Here a cumulative dissertation based on five journal papers is presented and therefore, some parts of the text will directly quote from publications I to V listed in section 6. Figure 2 presents a flowchart of the publications that support this thesis. Publication I introduces a methodology for calculation of mass transfer coefficients in dissolution of dense ceramic materials by liquid melts based on Computational Fluid Dynamics (CFD) simulations of rotating finger test experiments together with an asymptotic boundary layer approach for calculation of species diffusive flux. Publication II extends the method presented in Publication I for calculation of effective binary diffusivities from real experiments and it considers the actual shape of the corroded samples for the simulation domain. In Publication III, the dissolution of an alumina dense ceramic sample is studied with rotating finger test experiments and effective binary diffusivities are calculated and compared to reported values in literature. Publication IV, makes use of multiple evaluation of real experiments and delivers a Sherwood correlation for finger-test experiments useful for determination of effective binary diffusivities and other dissolution related parameters. Lastly,

Publication V presents a mathematical method for calculation of erosion parameters from experimental erosion profiles.

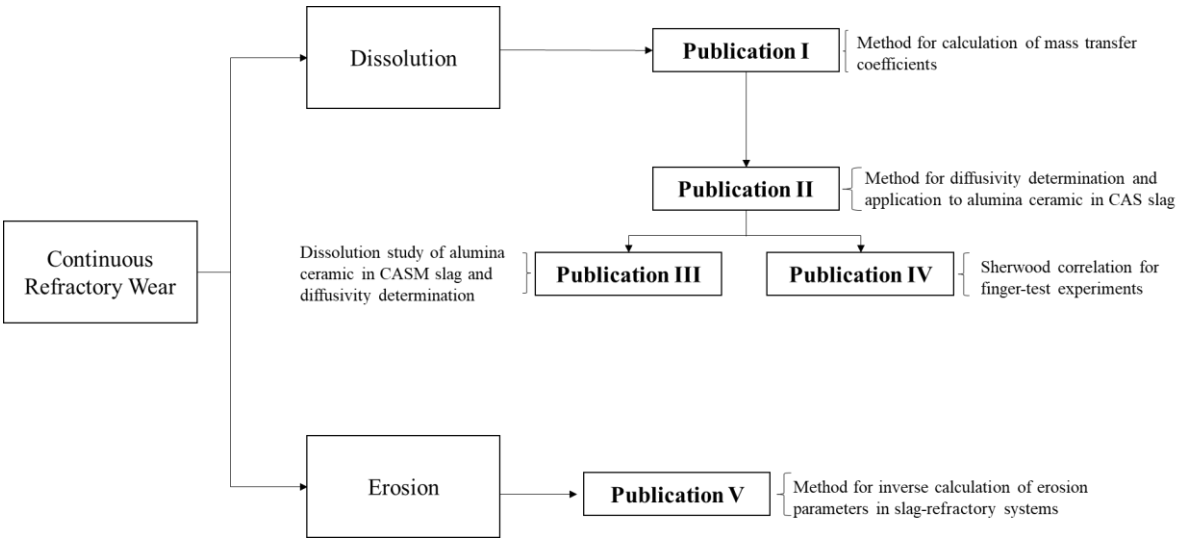

Figure 2. Flowchart of publications employed in this thesis

The next sections include the state of the art, a description of the methodology employed for the dissolution and erosion models, and a summary of the results presented in Publications I-V.

2.1 State of the art

The dissolution of refractory materials has been the focus of many investigations considering the consequences for the steel industry and other industries where pyroprocessing is necessary. From the refractory wear investigations found in the literature many target determination of the wear mechanisms via microscopical examinations [4]–[11], while other focus on quantification by wear parameters [12]–[16].

One notorious investigation is the work of Cooper and Kingery in 1964 on the dissolution of alumina in calcium aluminosilicate slags (CAS) [17]. Their work employs finger test investigations and investigates the dissolution of sapphire in three different situations: the molecular diffusion, where a quiescent fluid is assumed, the natural convection induced by density gradients and the forced convection by rotation of the sample inside the melt. For their system, they claimed and verified that the dissolution of the ceramic sample is dominated by the mass transfer in the liquid. Since this study, other authors have conducted similar investigations, and they also agree on the mass transfer in the liquid being the rate dominating step [1], [3], [12], [18].

In some cases, the rate dominating step might not be given by the diffusion of the species in the liquid. Lee and Zhang published a review article on the melt corrosion of oxide and oxide-carbon refractories [19]. In their work they examine phase formation in different oxide systems and discuss congruent and incongruent dissolution. Incongruent or indirect dissolution involves the precipitation of a solid phase and thus reduces the overall dissolution rate, owing to the necessary species diffusion in the solid.

Several methods for ceramic or refractory testing are available. Some of this include the cup slag test, finger test, test with rotating slag and the induction crucible furnace test. Reynaert et al. present a comparison between the different testing method and the advantages and disadvantages of each of these [20].

In this work, the chosen experimental set-up for both erosion and dissolution investigations is the rotating finger-test. This experiment has the advantage that a flow-field is generated by the rotation of the sample, which imitates the conditions to which the materials are exposed under service [19], [20]. Many authors have reported investigations on dissolution with this finger test experiments [4]–[10], [12]–[15], [17], [21]. Some of these studies quantify the wear by measurements of the lost weight or change in some dimension, such as the radius of the sample at a determined axial position. Moreover, the evaluation methods for dissolution investigations are frequently lacking because they fail to account for the effect of the Stefan velocity on the species boundary layer thickness as discussed in Section 2.2.2.1, and many also neglect the convective component of the dissolution mass flux. Furthermore, the equations employed for determination of the species boundary layer thickness are not always fitting, because no equations had been presented in literature for these experiments. For example, for finger test investigations some authors have employed the equation of Levich for the mass transfer to a rotating disc. While this equation may be employed to compute length change of the sample as done in the works of Cooper and Kingery [17] and Sandhage and Yurek [22], some authors [13], [16], [23] employed this equation for calculation of the mass transfer rate on the cylinder mantle, which is not justified. For the cylinder mantle, others have recurred to the equations for cylindrical surface such as that of Eisenberg [24], however these equations do not account for a clearance to the bottom of the crucible.

The refractory wear by erosion has received less attention in the literature than the dissolution. One of the reasons for this is the lack of an established erosion law as well as the lack of methods

for its depiction. From the investigations in this field, the work of Campbell et al. [25] presents a model for the erosion based on the analogy with soil erosion and implements the Parmenides's equation [26] into a CFD code. However, the erosion parameters are not correlated to experimental studies. The work of Huang et al. [27] introduces an empirical equation for the erosion rate, given by fitted polynomial of the product of wall shear stress and turbulent intensity. Recently, Wang et al. [28] presented a model for the wear in the refining ladle, where the erosion is modelled by power law of the wall shear stress relative to a reference value. In their work, the erosion parameters are obtained from experimental studies and adjusted to industrial measurements. While many different approaches to refractory erosion are found in the literature, most agree on the wall shear stress being the influencing variable for the erosion process [27]–[34].

2.2 Methods

2.2.1 Continuous Wear Testing Device

Both erosion and dissolution investigations are conducted with finger test experiments. The experimental set-up employed, hereafter the Continuous Wear Testing Device (CWTD) is state of the art and can be visualized in Figure 3, where the most significant components of this device are displayed. In these experiments the refractory sample is rotated at constant speed inside a slag bath. This is done for different steps of a defined length and multiple steps can be conducted for one experiment. The experimental schedule is defined a priori, and the schedule is introduced to the device software that operates fully automatically.

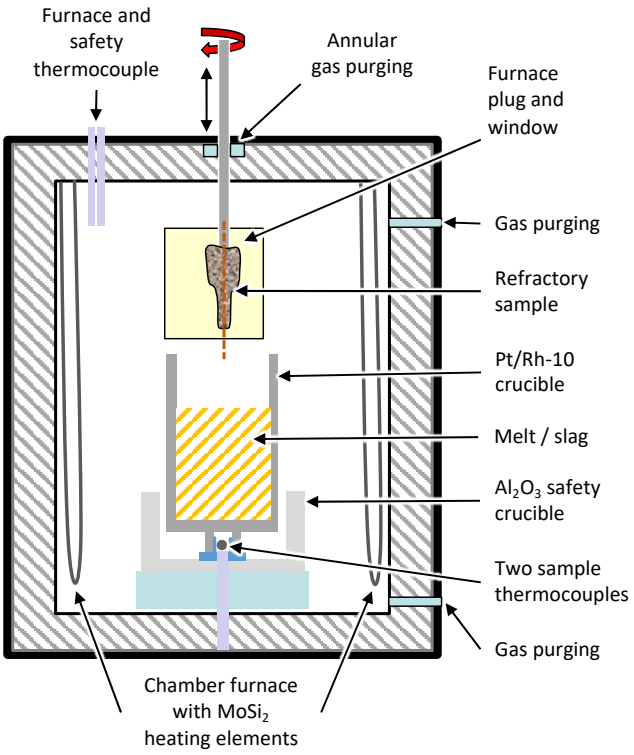

Figure 3. Schematic representation of the interior of the CWTD

A furnace with $MoSi_2$ heating elements is employed for reaching experimental temperature, which is monitored and kept constant by three thermocouples. Two thermocouples measure the sample temperature and are located below the crucible and one furnace and safety thermocouple is located at the top of the furnace. The crucible that contains the slag/melt is fixed in an alumina safety crucible by an interlock. The drilled sample is attached to the rotor shaft and rotor lifting system, which can be seen in Figure 4, extracted from the publication of Kircher et al. [35].

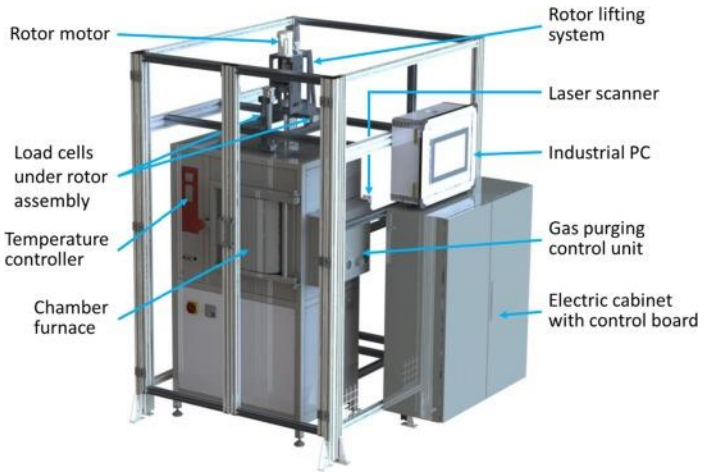

Figure 4. Exterior view of the CWTD. Reprinted from [35] (CC BY 4.0)

A distinct advantage of this device in comparison to classic finger test investigations is the possibility of in-situ measurement at high-temperature. This is achieved with the laser measuring device. The measurement is conducted at the end of each dissolution/erosion steps in addition to a reference measurement of the pristine sample before dipping in the melt. Firstly, the sample is pulled up and the slag is left for 30 minutes to drip from the sample surface, immediately after this, the laser device is placed in position after opening of the furnace plug. The sample is rotated at 2 rpm while the laser scans its surface. The position of all the moving parts are controlled by photoelectric sensors [35]. Figure 5 presents a photography of the interior of the device with an attached sample in upper position and was extracted from the publication of Kircher et al. [35]. Here the furnace window is open, and the laser measurement is taking place. The laser can achieve a resolution of 100 µm along the length and 20 µm in circumferential direction [36].

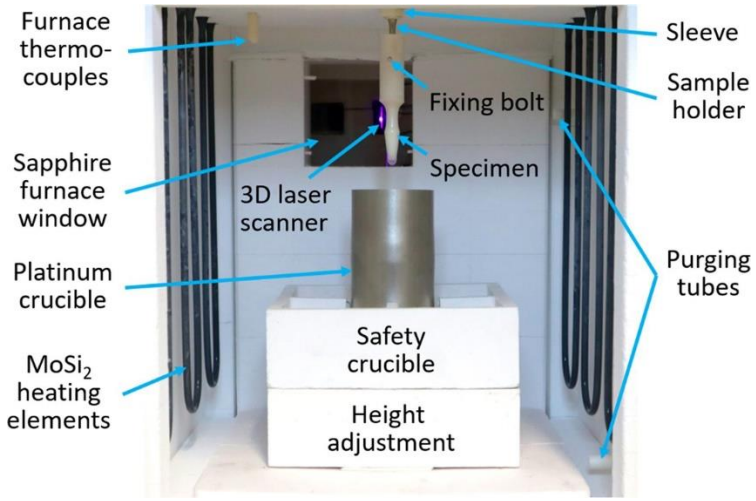

Figure 5. Photography of the interior of CWTD. Reprinted from[35] (CC BY 4.0)

This measurement provides high resolution dimensional information of the worn sample which can be used for assessment of the wear. An example of such measurement is shown in Figure 6. Here, towards the right side of the figure, we observe the worn area in pink and purple colors, whereas the flatter orange surface corresponds to the part of the sample that was not in contact with the melt. It is noticeable that the measurement is very noisy and shows high scatter especially at the worn area. This is not only a result of the roughness of the surface but also slag accumulation inside the pores can deflect the laser beam. Therefore, this data needs processing before it can be used for evaluation.

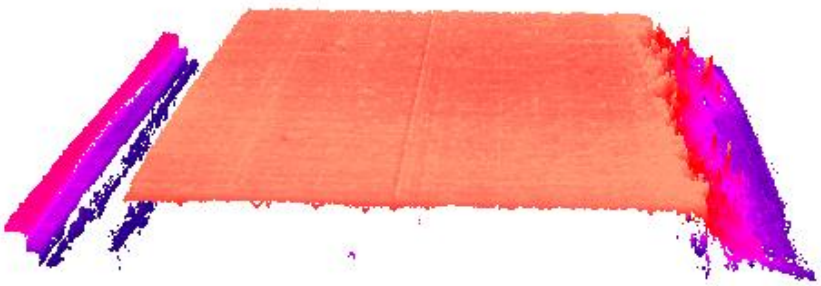

Figure 6. Laser measurement data before processing

The raw data is processed to provide an axisymmetric profile of the worn sample. The processing procedure is discussed in the publication of Kircher et al. [35]. An example of these profiles that corresponds to the raw data shown in Figure 6 is displayed in Figure 7. In this figure, the start of the immersion part is at 74.5 mm, for z larger than this value, the radius of the sample decreased from its original average of 15 mm due to the wear caused by the melt.

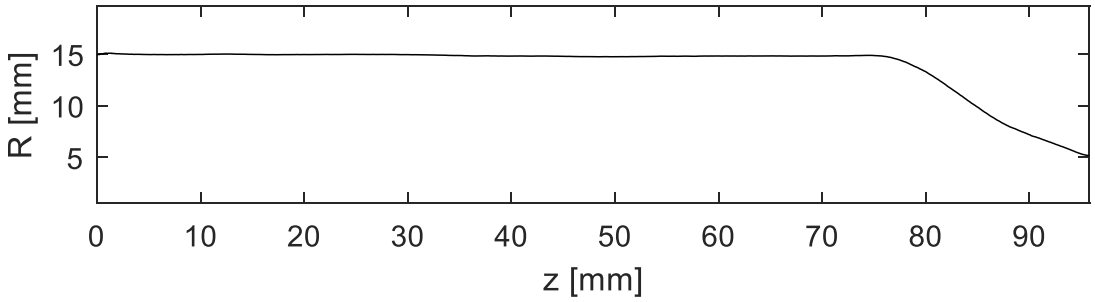

Figure 7. Processed worn profile

For the erosion case, these curves are directly used for the inverse calculation of erosion parameters by inverse calculation with simulated erosion profiles. For dissolution investigations it can be used to determine effective binary diffusivities as discussed in Section 2.2.2.5, where also the experimental profile is fitted to a simulated one. Furthermore, the axisymmetric profiles can be integrated to calculate both the surface area and volume of the sample. This allows calculation of the average mass flux density which can also be used for determination of effective binary diffusivities as explained in 2.2.2.5.

2.2.2 Dissolution model

2.2.2.1 Fundamentals

Investigations on dissolution of refractory materials target quantification of the dissolution mass flux density. With the dissolution dominated by the mass transfer in the liquid, appropriate models for the dissolution process can be constructed from Fick's first law of diffusion:

$$j = -D\nabla c \tag{1}$$

where, D represents the diffusivity and ∇c is the species concentration gradient. Very frequently, for the one-dimensional case, equation (1) is expressed in terms of the Nernst boundary layer thickness (δ_c):

$$j = -D\frac{\Delta c}{\delta_c} \tag{2}$$

here, Δc characterizes a well-defined concentration difference between the concentration at the interface and the solution bulk. Thus, calculation of the mass flux density requires information of the species diffusivity and the species boundary layer thickness. This can be achieved by solving the species transport equation with appropriate boundary conditions:

$$\frac{\partial c}{\partial t} + \nabla \cdot (c\vec{v}) - \nabla^2(Dc) = 0 \tag{3}$$

Already, we can notice the complexity of this problem, since the velocity field $\vec{v}$ is generally not known. Therefore, resolution of Equation (3) also necessitates resolution of the velocity flow field as per the Navier-Stokes equations (5) and continuity equation (4) for mass conservation.

$$\frac{\partial \rho}{\partial t} + \nabla \cdot (\rho\vec{v}) = 0 \tag{4}$$

$$\rho\frac{D\vec{v}}{Dt} = \vec{f} - \nabla p + \nabla \cdot \tau \tag{5}$$

Here $\vec{f}$ represents the sum of external body forces acting on the fluid, p is the pressure field, and $\frac{D\vec{v}}{Dt}$ is the material or substantial derivative:

$$\frac{D\vec{v}}{Dt} = \frac{\partial \vec{v}}{\partial t} + (\vec{v} \cdot \nabla)\, \vec{v} \tag{6}$$

τ is the viscous stress tensor of the deviator stresses which for the Newtonian case may be expressed by:

$$\tau = \mu \left(2\dot{\varepsilon} - \frac{2}{3} \boldsymbol{\delta} \nabla \cdot \vec{v} \right), \tag{7}$$

where $\boldsymbol{\delta}$ is the Kronecker unit tensor and the strain rate tensor $\dot{\varepsilon}$ is:

$$\dot{\varepsilon} = \frac{1}{2} (\nabla \vec{v} + (\nabla \vec{v})^T) \tag{8}$$

Equations (3) to (5) are expressed in convenient vector form and are generally valid; for application a coordinate system needs to be chosen. For instance, in Cartesian coordinates for the case of constant fluid density, the equations reduce to the form given by Equation (9) for the u component of the velocity:

$$\rho \left(\frac{\partial u}{\partial t} + \vec{v} \cdot \nabla\, u \right) = -\frac{\partial p}{\partial x} + \rho g_x + \mu \nabla^2 u \tag{9}$$

where g represents the gravity acceleration as a vector and g_x is the x component of this vector. The equations for v and w are analogous.

The boundary conditions for this problem must also be defined. At the refractory/melt interface ($x = 0$), the concentration matches the solubility limit c_s. For the velocity the no-slip condition applies, by which the tangential velocity at the wall vanishes. The normal velocity can be obtained by a mass balance at this interface, this balance is known as the Eckert-Schneider condition [37, p. 315] and is presented in Equation (10) where the variables are all evaluated at the interface. By considering a binary system, where the dissolving species is characterized by species 1 and all other species are termed residual species 2, the condition that the mass flux of

species 2 must be null at the wall, i.e., the wall is impermeable to the residual species, leads to the normal compensating velocity v_w. In this work we refer to this velocity as the Stefan velocity as an acknowledgment of the pioneering work of this author [38].

$$j_2 = -D\frac{dc_2}{dx}\Big|_{x=0} + v_w c_2 = 0 \tag{10}$$

Here D, represents an effective binary diffusivity. Here the case $D_1 = D_2 = D$ is considered, that means fluid density is independent from concentration. With this further latter assumption, the normal velocity or Stefan velocity, reads:

$$v_w = -\frac{D}{1 - w_s}\frac{dw_1}{dx}\Big|_{x=0} \tag{11}$$

Here w_s represents the solubility limit in mass content and w_1 the mass content of species 1. These derivations might also be found in Publication 1, where the Navier-Stokes equation are presented for the particular case in cylindrical coordinates. This work deals with steady state mass transfer, and therefore time derivatives in the previous equations vanish for sufficiently large times. However, in numerical resolution of the equations, as it will be later described, time-advancement until reach of steady-state is conducted and therefore the equations are presented fully.

Moreover, if we consider the large character of the Peclet number $Pe = \frac{Lu}{D}$ we could argue that the diffusive terms in equation (3) might be neglected when compared to the convective terms. Additionally, if we consider a steady state process, for the two-dimensional case this equation reduces to:

$$\nabla \cdot (c\vec{v}) = 0. \tag{12}$$

If the density is constant, the solution to this equation is satisfied by a constant concentration profile $c = c_0$. Such solution cannot accommodate the boundary conditions described above, where the concentration varies from the saturation limit to the bulk value. Therefore, there must exist a small region of the domain where the diffusive terms are of importance and the second derivative of the concentration takes large values, this region is called the species or diffusion

boundary layer [39]. In contrary to Nernst theory this is not a static film where the velocity is zero, rather the fundamental characteristic is that the convective and diffusive terms are of comparable orders.

For practical applications it might be desired to express the mass flux density (j) through mass transfer coefficients (k_c) with the following definition:

$$j = k_c(c_s - c_0) \tag{13}$$

where the $\Delta c = (c_s - c_0)$ clearly illustrates the effect of chemistry in the matching of refractory/melt and k_c is, besides diffusivity, mainly affected by the flow conditions. Evidently, the wear rate might be reduced by matching the refractory and slag so as to minimize Δc, that is using saturated melts, or the optimal flow conditions might be affected via clever vessel design or adapting the processing conditions.

In a dimensionless form, the diffusive mass flux density j_D might be represented by the Sherwood number with a characteristic length L:

$$Sh = \frac{j_D L}{D\,\Delta c} \tag{14}$$

To the diffusive mass flux, a convective part j_c resulting from the Stefan velocity must be added and the total dissolution flux results:

$$j = j_D + j_c = -D\left.\frac{dc_1}{dx}\right|_{x=0} + v_w c_s = -D\rho\frac{1}{1-w_s}\left.\frac{dw_1}{dx}\right|_{x=0} \tag{15}$$

In modelling of dissolution, the problem comprises dissolution characterization via estimation of j_D, the mass transfer coefficients k_c, species boundary layer thickness δ_c or Sherwood number by known diffusivity, and the inverse calculation of effective binary diffusivity from experiments.

2.2.2.2 Asymptotic boundary layer method

An important characteristic of the slag/refractory systems considered in this work is that they present distinctly large Schmidt numbers ($Sc = \nu/D$) which can range up to 10^7. This has an

important physical meaning; because the Schmidt number gives an indication of the ratio between momentum to species boundary layer thicknesses. Therefore, for these systems the momentum boundary layer, that is, the region immediate to the wall where the velocity gradients are largest, is much thicker than the species boundary layer thickness.

For an adequate numerical resolution of the equations, these regions must be discretized appropriately. For large Schmidt numbers, the species equation requires a much finer resolution than the momentum equations. This can be easily noticed when considering a benchmark problem of fluid dynamics that shares commonalities with our CWTD, this is the flow-field induced in an originally static fluid by a rotating disc, where analytical solutions are available. This set-up can be visualized in Figure 8. While an accurate discretization requires a grid independence test, as a rule of thumb, 10 nodes are required to represent a boundary layer profile in the laminar regime.

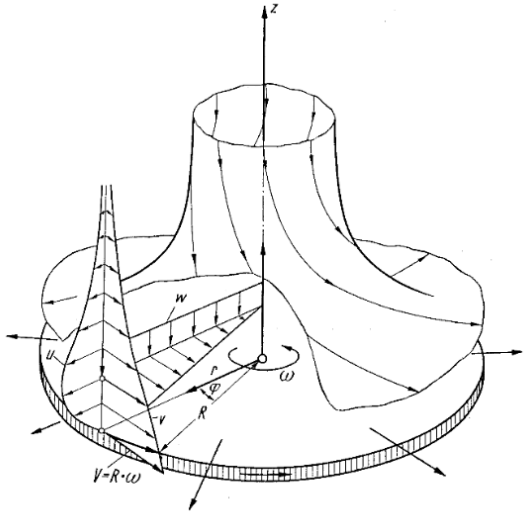

Figure 8. Flow due to a rotating disc in a fluid at rest. Reprinted by permission from Springer Nature: Springer Nature, Exact Solutions of the Navier-Stokes Equations by Herman Schlichting (Deceased) and Klaus Gersten. Copyright 2017

The velocity boundary layer thickness according to Schlichting [40, p. 120] is given by Equation (16):

$$\delta = 5.5\sqrt{\nu/\omega}. \tag{16}$$

The species boundary layer thicnkess might be obtained from the notorious equation of Levich [39]:

$$\delta_c = 1.61\sqrt{\nu/\omega}Sc^{-1/3}. \tag{17}$$

Therefore the ratio of momentum to species boundary layer thickness only depends on a power of the Schmidt number:

$$\frac{\delta}{\delta_c} = 3.4Sc^{1/3} \tag{18}$$

In Table 1, the discretization necessary for resolution of species and momentum equations in this set-up is given. The values are presented for a Schmidt number of 10^7, and a kinematic viscosity $\nu = 2.5 \cdot 10^{-4} m^2/s$, which represents a typical value for the slags used in the experiments presented in this thesis. A scheme of the discretization is shown in Figure 9.

Table 1. Calculation of discretization requirements for the flow due to a rotating disc

$\omega = 200\ rpm$		$\omega = 5000\ rpm$	
$\frac{\delta}{\delta_c} \approx 730$		$\frac{\delta}{\delta_c} \approx 730$	
$\delta \approx 19\ mm$	$y_p = 0.475\ mm$	$\delta \approx 3.8\ mm$	$y_p = 0.095\ mm$
$\delta_c \approx 0.026\ mm$	$y_p = 6.5 \cdot 10^{-4} mm$	$\delta_c \approx 0.0052\ mm$	$y_p = 1.3 \cdot 10^{-4} mm$

From these results, we observe that the first node (y_p) must be located at a much closer distance to the wall for the resolution of the species boundary layer than for the resolution of the velocity boundary layer; moreover this distance decreases with increasing rotational speed, while the ratio of both thickness remains constant and only depends on the Schmidt number. For this

particular example, we observe that the discretization required is quite fine and is determined by the species equation. In many cases, such fine discretization might not be possible, depending on model complexity and simulation time required. Inflation layers may be used to reduced the amount of elements used in discretization.

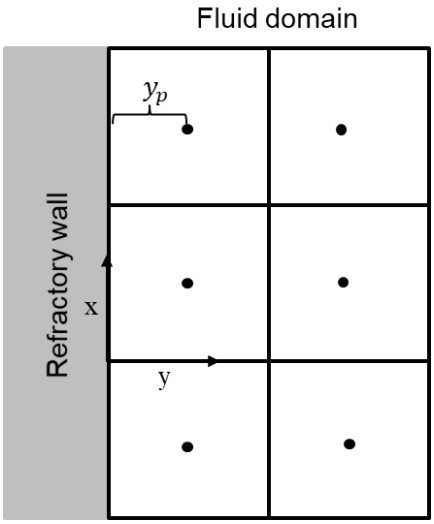

Figure 9. Scheme of domain discretization

To avoid dealing with such fine meshes we make use of an asymptotic boundary layer approach for large Schmidt numbers. This method "was first elucidated by Lighthill [41] through a von Mises transformation of the energy equation" [42], i.e. the method was derived for the case of heat transfer and some modifications to the original method will be done at the end of this section. The method makes use of the fact that the temperature or species boundary layer is much thinner than the momentum boundary layer and approximates the velocity profile within the former by a linear expansion.

$$u = y\beta \tag{19}$$

$$\beta = \left.\frac{\partial u}{\partial y}\right|_{y=0} \tag{20}$$

This becomes asymptotically exact for $Sc \to \infty$. The normal component of the velocity can be obtained from the continuity equation which for an incompressible boundary layer flow is given by Equation (21).

$$\frac{\partial u}{\partial x} + \frac{\partial v}{\partial y} = 0 \tag{21}$$

With Equation (20) the normal velocity results:

$$u = -\frac{1}{2}\beta' y^2 \tag{22}$$

Worth noticing is that both u and v are expanded from the wall coordinates, where the boundary conditions for this problem are zero velocities both in normal as well as tangential direction. These results are used for solving the convective-diffusive boundary layer equation:

$$u\frac{\partial c}{\partial x} + v\frac{\partial c}{\partial y} = D\frac{\partial^2 c}{\partial y^2} \tag{23}$$

here, $\frac{\partial^2 c}{\partial x^2}$ has been neglected since the variations in the normal direction are expected to be much higher than in tangential direction ($\frac{\partial^2 c}{\partial y^2} \gg \frac{\partial^2 c}{\partial x^2}$). The result is a local, steady-state Sherwood profile:

$$Sh_0(x) = \frac{L\,Sc^{1/3}}{9^{1/3}\,\nu^{1/3}\Gamma(4/3)}\sqrt{\beta(x)}\left[\int_0^x \sqrt{\beta(\zeta)}\,d\zeta\right]^{-1/3} \tag{24}$$

where L is a characteristic length. The most important feature of this equation is that is only a function of fluid properties, geometrical parameters, and the flow related variable β. This means that resolution of the flow-field can be conducted independently, and the mass transfer coefficients can be calculated later in a post-processing step avoiding the use of so refined meshes.

Simulations of the CWTD are for an axisymmetric geometry with rotation. Adaptation of the previous results to this situation is straightforward because the boundary layer equations are the same for an axisymmetric body, only the continuity equation is modified [40, p. 322] as shown in Equation (25). Moreover, the azimuthal component of the velocity does not aid mass transfer in the laminar regime [43, p. 397].

$$\frac{\partial(u\mathcal{R})}{\partial x}+\frac{\partial(v\mathcal{R})}{\partial y}=0 \tag{25}$$

Where $\mathcal{R}$ is the radius of the revolution body, and u and v are the tangential and normal velocities in the plane. The coordinate x is measured along the surface and y is the direction normal to the wall. With these revisions, the similarity variable used in solving the problem is changed and the end results provided by Newman [43, p. 396] are adapted and expressed by Equation (26):

$$Sh_0(x)=\frac{L\,Sc^{1/3}}{9^{1/3}\,\nu^{1/3}\Gamma(4/3)}\sqrt{\mathcal{R}\,\beta(x)}\left[\int_0^x \mathcal{R}\sqrt{\mathcal{R}\,\beta(\zeta)}\,d\zeta\right]^{-1/3} \tag{26}$$

As was mentioned before, the boundary conditions used for this problem are zero velocities at the wall. For mass transfer in dissolution, we observed in Section 2.2.2 that tangential velocity vanishes but the normal velocity is given by Equation (11). This situation is analogous to boundary layer control by blowing and it increases the species boundary layer thickness, therefore it decreases the mass transfer rate. “The use of Eq. (26) under the influence of a Stefan flow is justified, as has been demonstrated by Schlichting and Gersten [44] that the similarity of solutions of wedge-flow velocity profiles still holds when the Eckert-Schneider condition (Eq. (10)) is fulfilled, and the constant concentration of the dissolving species is fixed at the wall.”[42]. Even when the method is applicable, some modification is necessary to account for the effect of the Stefan velocity on the boundary layer. Merk is one author that has dealt with this subject and his work provides equations to rectify the error in neglecting the Stefan velocity in the boundary conditions [45]. With this correction, the heat and mass transfer analogy may still be used, when energy dissipation effects are insignificant. In the work of Merk [45], an equation for large Schmidt numbers is presented:

$$\chi_D=\frac{Sh}{Sh_0}=\frac{1}{1+0.566B} \tag{27}$$

Where B is a dimensionless saturation limit defined by:

$$B = \frac{w_s - w_1}{1 - w_s} \tag{28}$$

"Moreover, according to Acrivos [46], a relation similar to Eq. (26) can be derived (29), which also considers the effect of the Stefan velocity only by replacing 1/(4/3) by a quantity b, which is implicitly defined by the following equation:" [42]

$$\frac{1}{b} = \int_0^\infty e^{Bbx - x^3} dx \tag{29}$$

"This modification to Equation (26) can also be expressed by multiplication with χ_D defined by:" [42]

$$\chi_D = \frac{\Gamma(4/3)}{\int_0^\infty e^{Bbx - x^3} dx} \tag{30}$$

An end-formula for calculation of dissolution mass flux based on Equation (15) and the corrections presented above:

$$j = D\rho B \chi_D Sh_0 D\Delta c / L \tag{31}$$

whereas the mass transfer coefficients are given by:

$$k_c = \frac{\chi_D}{1 - w_s} \frac{Sh_0 D}{L} \tag{32}$$

2.2.2.3 Flow-field

Before proceeding to the numerical solution of the governing equations, appropriate models need to be chosen based on hypothesis about the unknown flow-field. The aim of the simulations is to depict the flow-filed generated by the rotation of the refractory sample inside the melt for the finger-test experiments, as described in Section 2.2.1. This set-up presents geometrical symmetry around the axis of rotation, if the flow-field also exhibits this symmetry, the equations can be simplified and 2D simulations can be performed. Moreover, considerations about the flow-regime are necessary, generally speaking we need to decide between transient and

steady-state simulations and laminar or turbulent regimens. These considerations are essential to capture the actual behavior of the flow-field; however, this also necessitates verification and validation.

For characterization of the flow-regimen, we can distinguish between two specific sections of the flow-domain: these are the annular region in between the refractory sample and crucible, and the clearance region from the sample tip to the crucible bottom. These two regions are represented in the figure below:

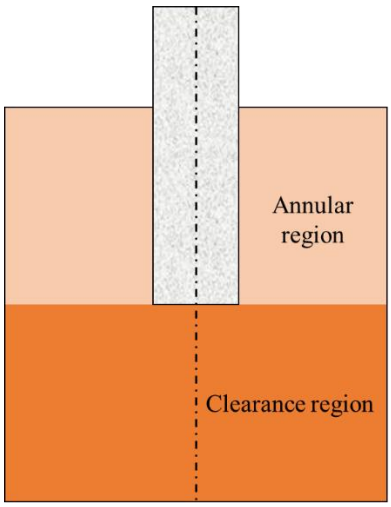

Figure 10. Flow domain regions

This distinction is done because for each of these regions there are similar set-ups from which information about the flow field can be obtained. Starting by the annular region, this is a bench-mark problem in fluid dynamics: the flow field between two rotating concentric cylinders. If we consider infinite length cylinders and axisymmetric flow, both the cases of inviscid flow and the case of viscous flow simplify, and the Circular Couette (CC) flow has an analytical steady state solution for which the azimuthal velocity v_θ is only a function of the radial coor-dinate r:

$$v_\theta(r) = \Omega_1 \frac{\mu - \eta^2}{1 - \eta^2} r + \Omega_1 R_1^2 \left(\frac{1 - \mu}{1 - \eta^2}\right) \frac{1}{r}, \tag{33}$$

where $\mu = \Omega_2/\Omega_1$ is the ratio of the rotational speeds of the outer cylinder of radius R_2 to the inner cylinder of radius R_1, and $\eta = R_1/R_2$. However, this flow field is not maintained for all Reynolds numbers and the system is susceptible to the development of centrifugal instabilities.

A first criterion for the stability of the CC regimen was given by Rayleigh [47] for the case of inviscid flow in terms of the angular velocity $\Omega = v_\theta/r$:

$$\frac{d(r^2\Omega)^2}{dr} > 0, \tag{34}$$

where $|r^2\Omega|$ is the angular momentum per unit mass. This states that a velocity distribution given by equation (33) may be maintained as long as angular momentum increases monotonically outwards [48, p. 273]. When replacing Ω by the analytical solution presented before, this criterion reduces to:

$$\mu > \eta^2, \tag{35}$$

A good illustrative explanation on the physical meaning of this criterion is given by Chandrasekhar in his book [48]. Euler's equations for inviscid flow for the angular component of the velocity reads:

$$\frac{\partial v_\theta}{\partial t} + v_r\frac{\partial v_\theta}{\partial r} + v_r\frac{\partial v_\theta}{\partial z} + \frac{v_r v_\theta}{r} = 0, \tag{36}$$

which for the case in matter is equivalent to:

$$\frac{d(rv_\theta)}{dt} = \frac{d(r^2\Omega)}{dt} = 0, \tag{37}$$

from where we see that the angular momentum $L = r^2\Omega$ remains constant. If we consider two fluid rings of equal mass with radius $r_1 < r_2$, the mass of each given by: $2\pi r_1 dr_1 = 2\pi r_2 dr_2 = dS$. A force $v_\theta^2/r = L^2/r^3$ is acting in radial direction on each of these rings. If we exchange the fluid rings, considering that the angular momentum remains constant with the motion, we can compute the change in kinetic energy[48]:

$$\left[\left(\frac{L_2^2}{r_1^2} + \frac{L_2^2}{r_1^2}\right) - \left(\frac{L_1^2}{r_1^2} + \frac{L_1^2}{r_1^2}\right)\right] dS = (L_2^2 - L_1^2)\left(\frac{1}{r_1^2} - \frac{1}{r_2^2}\right) dS, \tag{38}$$

Here we see that this change is only positive for $L_2^2 > L_1^2$. Therefore, if the angular momentum increases monotonically with r, a source of energy is necessary for the interchange of fluids rings and the system is stable as expressed by Rayleigh's criterion. A similar analysis may be done to understand the physical origin of these instabilities as proposed by Di Prima and Swinney [49, p. 143]. One characteristic of this flow-field is that the centrifugal force is balanced by the radial pressure gradient. If we exchange the outer fluid ring of velocity V_2 with the inner one of velocity V_1, the velocity of the outer ring after the exchange is $v_\theta = r_1 V_1 / r_2$, while the prevailing pressure gradient is $\rho V_2^2 / r_2$. Therefore, if the centrifugal force $\rho V_1^2 r_1^2 / r_2^3$ is larger than the pressure gradient, the ring will continue to migrate outwards, and the instability will settle [49, p. 143]. This happens when: $V_1^2 r_1^2 > V_2^2 r_2^2$ which is equivalent to Rayleigh's criterion.

The case of viscous flow is more complex however, it is reasonable to expect that the viscous stresses should delay the onset of instability. Taylor was one of the first authors to investigate this problem in 1923 both experimentally as well as theoretically by applying linear stability theory [50]. With his analysis he found the locus of transition from the CC flow to a regimen thus known as Taylor-Couette (TC) or Taylor-Vortex flow, which he experimentally verified for the case of small gap width and very long cylinders. In his work, Taylor found that the first transition succeeds to the TC flow, where laminar, time independent, axisymmetric centrifugal structures appear and form counter-rotating toroidal vortices [51]. This transition and the transition to other subsequent regimes is commonly defined in terms of the Taylor number. For the case of stationary outer cylinder, this number is given by equation (39) and represents a ratio of the magnitude of centrifugal to viscous forces.

$$Ta = \frac{2\Omega_1^2 d^4 \eta^2}{(1-\eta^2)\nu^2}. \tag{39}$$

Since the work published by Taylor, many authors have conducted similar analysis and this problem has become a benchmark problem of fluid dynamics [48], [49], [51]–[80]. For example, authors have also investigated the effect of thermally induced density gradients on the stability of the CC and TC flow [53]–[56], [58], [62], [65], [81], were they have considered the effect of both Archimedean and centrifugal buoyancy. The effect of axial flow in the stability and on the heat/mass transfer rates has also been investigated by some authors [82]–[86]. Besides the TC flow, several other flow regimes have been studied both theoretically as well as

experimentally. Some of this include the Wavy Vortex flow, Modulated flow, and turbulent flow regimens. Figure 11 was obtained from the publication of Andereck et al. [67] and shows some of the multiple regimes found in this configuration and the boundaries among these. The abscissa in this figure is given by the outer Reynolds number and the ordinate is given by the inner Reynolds number for independently rotating cylinders.

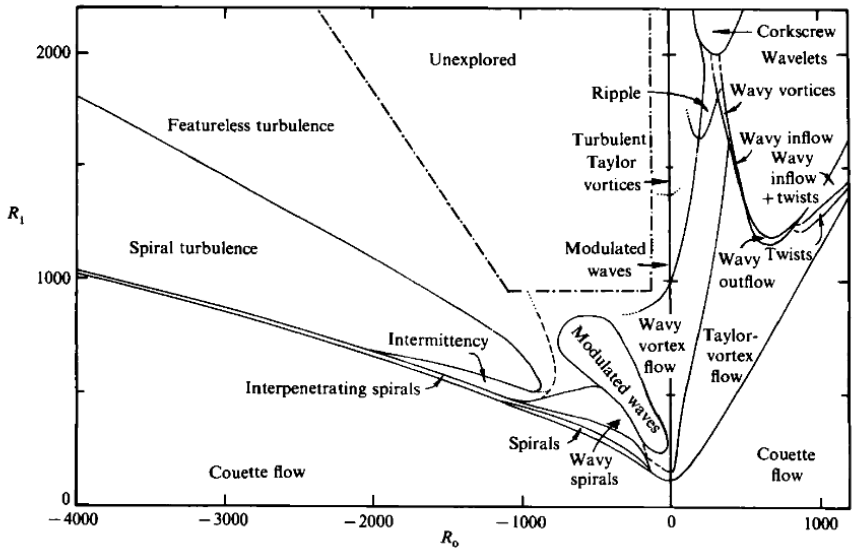

FIGURE 1. Regimes observed in flow between independently rotating concentric cylinders. Dashed lines indicate the transition boundaries that are difficult to establish from visual observation alone since there is no abrupt change in the appearance. Dotted lines indicate the expected, but not yet observed, continuation of several boundaries. More detail is shown in figures 2 and 18 for counter-rotating and co-rotating cylinders, respectively.

Figure 11. Regimes observed in flow between two rotating concentric cylinders. Reprinted by permission from [49, p. 140]

Figure 12, extracted from [49, p. 140] shows photographs of different flow regimens encountered in the annular region between rotating cylinders. In Figure a, the TC flow can be observed, with the developed laminar rings, while Figure d shows already a turbulent flow, where the randomness of the oscillations in the flow is noticeable.

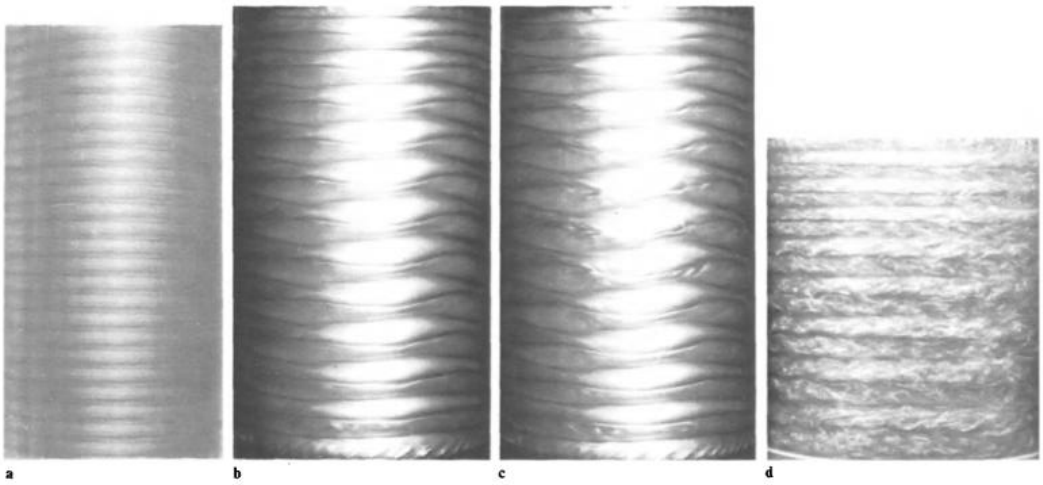

Fig. 6.1a–d. Photographs of the flow between concentric cylinders with the inner cylinder rotating. (The radius ratio is 0.88.) **(a)** $R \simeq R_c$; Taylor vortex flow [6.5]. **(b)** $R/R_c = 10.4$; wavy vortex flow [Ref. 6.6, Fig. 19d]. **(c)** $R/R_c = 12.3$; the "first appearance of randomness" in wavy vortex flow [Ref. 6.6, Fig. 19c]. **(d)** $R/R_c = 23.5$; the azimuthal waves have disappeared and the flow is turbulent, although the axial periodicity remains [Ref. 6.7, Fig. 1d]. The visualization of the flow in these experiments was achieved by suspending small flat flakes in the fluid; the flakes align with the flow, and variations in their orientation are observed as variations in the transmitted or reflected intensity

Figure 12. Photographs of different flow regimens encountered between rotating cylinders. Reprinted by permission from Springer Nature: Springer Nature, Instabilities and transition in flow between concentric rotating cylinders by R. C. Di Prima and Harry L. Swinney. Copyright 1981

Most of these investigations focus on the case of small gap width, that is $d = R_2 - R_1$ is small compared to either R_1 or R_2, however the geometry of the CWTD doesn't fall under this category. For characterization of the critical rotational speeds, DiPrima et al. [66] presented the critical Taylor number for different radii ratio η. From this work, a correlation of the presented data was obtained and reported in our Publication 1: $Ta_c = 1600/\eta^{1.005}$. Also, Dominguez [87] presents similar data, the largest differences between these are for the smallest values of η, however for the values of η used in this work there is little difference between these values. With this information it is possible to calculate the theoretical minimal rotational speed for the transition from a CC to a TC flow-field. This is exemplified in Table 2 for a chosen dissolution experiment shown in Publication I.

Table 2. Characteristic experimental values for flow-regimen characterization

Density *kg/m³*	Viscosity *Pa s*	Sample Radius *mm*	Crucible Radius *mm*	Rotational Speed *rpm*	Taylor Number	Critical Taylor number	Axial wave length *mm*
2589	0.6423	10	32.5	200	382	5230	44.7

From these values, we observe that our system is within the CC regime and the critical rotational speed for the transition for a TC flow is not achieved. The axial wavelength was also obtained from the data presented by DiPrima [66]. This value corresponds to the length of two consecutive counterrotating vortexes upon development of the TC flow, therefore each vortex would have a length of 22.35mm and given that the gap width is 22.5mm the vortices would appear square, as it is typically the case in the TC flow. Hence, we conclude that a hypothesis of laminar, steady-state, and axisymmetric is appropriate for the model when considering the annular region.

It is important to notice that the previous results are based on the case of infinite length cylinders, where the end effects may be neglected. However, for our CWTD experiments the annular region is relatively short, for e.g., for the experiment presented in Table 2, the submerged length of the cylinder is 55mm, which is comparable to the axial wavelength. Many authors have studied the influence of end-effects on flow field between the rotating cylinders [64], [68], [70]–[72], [74], [75], [77], [79], [80], [88], [89]. Even for long cylinders end-effects have been reported to have a major influence in the developed flow-field [78]. The analysis of the influence of end-effects on the flow-field is based on consideration of three representative boundary conditions: the case of fixed plates, rotating plates, and no shear boundary conditions. Three characteristic problems are used to describe the effect of these boundary conditions. The static plate analysis corresponds to the similar configuration of the flow of a revolving fluid over a fixed plate and was studied by Bödewadt [89]. The flow from a rotating plate is analogous to the rotating disc first investigated by von Karman [90] and the no shear boundary condition is similar to the investigations done by Ekman on the effect of Coriolis force on ocean currents [91]. These types of flow fields belong to the family of flow fields know as the BEK family (Bödewadt, Ekman, von Karman) in fluid dynamics. The geostrophic characteristic of the flow-field is not maintained in the boundaries where the boundary conditions are imposed; therefore, a radial component of the velocity emerges and the resulting vortical structures present some similarities to the TC structures, however they are fundamentally different in nature. In the literature, the vortical structures appearing due to the end effects are generally referred to as Ekman vortices. In the CWTD the no-shear boundary condition represents a good approximation for the melt/atmosphere interface, whereas the surface where the clearance region meets the annular region is not well defined.

The clearance regions is similar to the flow-field induced by a rotating disc on a static fluid, which was briefly discussed in Section 2.2.2.2. This problem has been investigated by many authors [37], [43], [90], [92], [93], where the main difference to our set-up is that in these investigations the disc is considered to be of infinite radius. The rotating disc acts a centrifugal pump by expelling fluid outwards in radial direction, continuity demands an axial flow develops which replaces the displaced fluid. Here the flow-field is laminar up to a Reynolds number of $2 \cdot 10^5$ [43, p. 355] which is much higher than the values considered in the investigations conducted for this thesis. Therefore, for this region, the laminar and axisymmetric hypothesis also holds.

To assess the possible influence of natural convection induced by density gradients in the mass transfer rates, as an approximation, we compare the correlation obtained in Publication IV for our set-up considering only forced convection with an equation for natural convection for concentric vertical cylinders [94]. For this comparison, the fluid properties and geometrical parameters are taken from Publication I. The results are presented in Figure 13, where we observe that for Reynolds larger than about 1.5, the forced convection is dominant. The Reynolds number corresponding to the experiment investigated in this publication is 8.4, where the Sherwood number by forced convection is almost three times larger than natural convection. Further, we consider an equation of the form $Sh^n = Sh_F^n + Sh_N^n$ as suggested in [95, p. 594], where Sh_F represents the Sherwood number considering only forced convection and Sh_N considering only natural convection. For an exponent n between 3 and 4, the error incurred by neglecting the free convection is between 0.3% and 1.2%. Therefore, only the forced convection by the rotation of the sample is considered in the simulations.

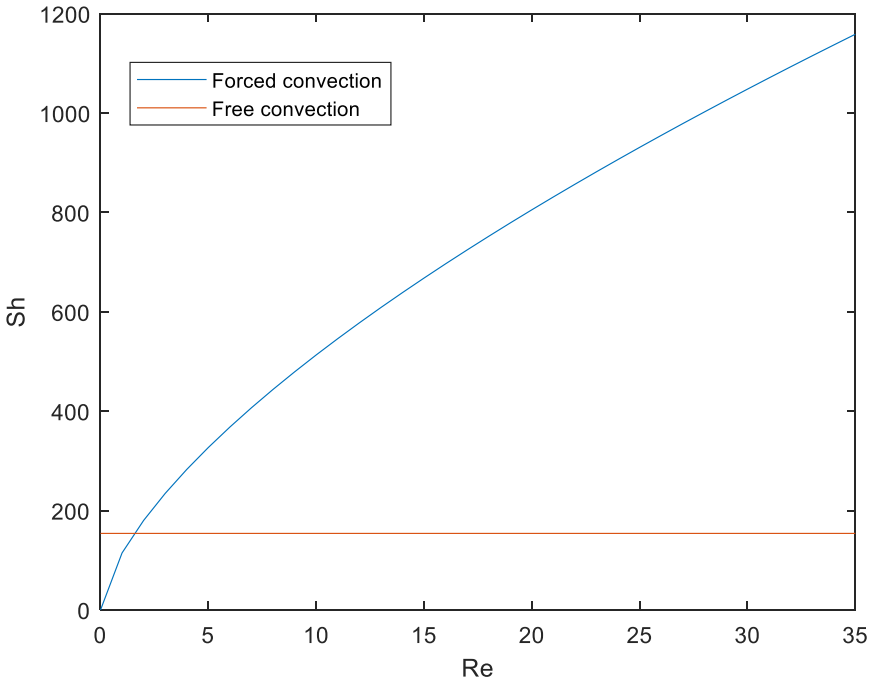

Figure 13. Sherwood number values for forced and free convection

2.2.2.4 CFD model

The CFD model implemented in Ansys Fluent v19.0 is a 2D axisymmetric model of both the melt and atmosphere phases. Details on the numerical schemes, mesh and models can be found in Publication 1 for the case of the idealized cylindrical surfaces and in Publication II for the simulations with corroded surfaces, where the geometries are obtained from laser measurement as described in Section 2.2.1. While the flow-field is considered steady-state, the solution is advanced from a static flow field until the velocity gradients at the wall reach their end value and remain constant. The simulations are conducted with the aim of resolving the flow-field and the mass transfer rates are calculated in the post-processing step with the asymptotic boundary layer method described in Section 2.2.2.2.

2.2.2.5 Diffusivity determination

The dissolution model may be employed for diffusivity determination from CWTD experiments. The application of the dissolution model with the asymptotic boundary layer method provides a Sherwood profile as a function of the unknown diffusivity. Two possible methods are used for obtaining this value. The first one consists of using the experimentally determined mass flux density which is calculated from the laser measurements of the corroded surface as described in Publication III. For this, the geometry is split in two parts: the mantle surface and the bottom disc shaped surface. Then, an area weighted average Sherwood number is computed:

$$\overline{Sh} = \frac{1}{A_1+A_2}(A_1\overline{Sh}_1 + A_2\overline{Sh}_2) \tag{40}$$

Details on calculation of Sh_1 and Sh_2 are found in Publication I and II. These values are functions of the Schmidt number, and the effective binary diffusivity is obtained by matching the simulated results to the experimental mass flux density calculate. Secondly, given that the laser measuring device provides the corrosion profiles, the effective binary diffusivity can also be obtained from curve fitting of a simulated corrosion curve to the experimentally obtained corrosion profile. Details on the method for calculation of the simulated corrosion curve are found in Publication II.

2.2.3 Erosion model

2.2.3.1 Fundamentals

In the erosion of refractory materials, the flow is responsible for the shear stresses that act on the material surface. These forces cause the grains of the material to detach from the matrix and the eroded particles are washed away by the liquid. The grain/matrix bond must first be weakened e.g. by dissolution in order for these forces to be sufficient for erosion. For this reason, measurements of the mechanical properties of the virgin material are not expected to directly represent the resistance against erosion and further, the erosion parameters cannot be considered pure material parameters but rather depend on the material/melt interaction which may also depend on the process conditions. Though the infiltrated slag might appear saturated; the bond created by the fines might still dissolve due to the large curvature of the particles considering the Gibbs-Thomson equation (here for spherical particles):

$$\frac{c_r - c_f}{c_f} = \frac{2\gamma_{sl}V_M}{R\,T\,r} \tag{41}$$

where, c_r is the solubility of a particle of radius r, c_f the solubility for a flat surface, $2\gamma_{sl}$ the surface energy of the solid liquid interface, V_M the molar volume of the dissolving species, R is the universal gas constant, and T the temperature.

In this work, erosion modelling of refractory materials is based on the Partheniade's equation [26] obtained from the field of soil erosion and presented in Equation (42). "The erosion law is a function of the wall shear stress (τ), and the erosion parameters include the critical shear stress

(τ_c), which characterises the flow condition upon which the shear stress is sufficient to begin grain detachment, the rate of detachment k_d [96], and the exponent a.

$$\dot{\varepsilon} = k_d(\tau - \tau_c)^a \tag{42}$$

$\dot{\varepsilon}$ has dimensions of length/time and is considered as a velocity. This is in contrast to most continuous-wear investigations, where the output of the studies is the mass flux density. The units of τ and τ_c are Pa, and the units of k_d depend on the dimensionless power a as follows: $[k_d] = ms^{-1}Pa^{-a}$. Very often, the parameter a is set to unity." [97]The employment of an erosion law coming from the field of soil erosion is rooted on the similarities between soils and refractory materials, both representable by a grain/matrix structure.

2.2.3.2 CFD model

In contrast to the model developed for dissolution, the CFD model is a transient model, where the fluid domain increases with time. The refractory represents a wall of the domain, and this evolves in time owing to the erosion. The simulations involve only the melt phase and are considered laminar and axisymmetric. Details on the numerical schemes and other model characteristics can be found in Publication V.

An important aspect of the model is the implementation of dynamic meshing methods, not only for accounting of the erosion on the refractory wall but also to maintain a sufficient mesh quality that allows the time advancement and procures accurate results. The dynamic meshing methods employed are discussed in detail in Publication V. Additionally, a remeshing method is implemented that, when the mesh quality is insufficient, permits coarsening or refining of the mesh elements.

The erosion is implemented in a User Defined Function written in the C Programming language. A characteristic challenge is the fact that the displacement is implemented at node positions, where flow variables are not available. To overcome this, distance weighted average of the wall shear stress is used. Moreover, the direction of the erosion vector is given by an area weighted average of the cell face normal vectors. This is shown schematically in the figure below:

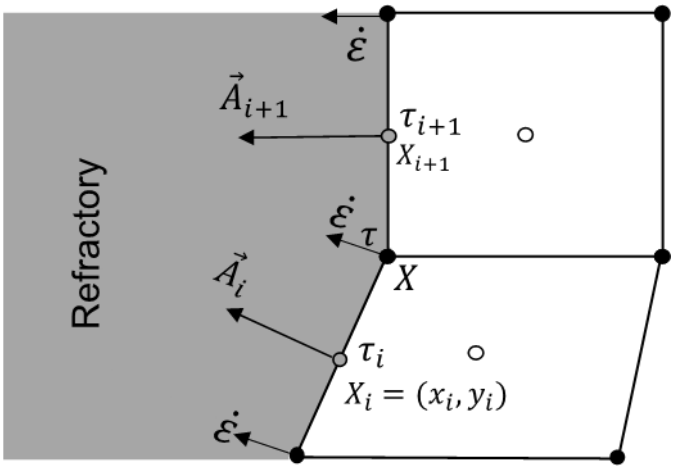

Figure 14. Erosion vector implementation at refractory wall boundary. Adapted from [97] (CC BY 4.0)

2.2.3.3 Inverse Problem

The output of the CFD simulation is the erosion profile. This information is compared with an experimentally obtained erosion profile with the aim of calculation of the erosion parameters in Equation (41). This is achieved by inverse calculation. A least-squares problem is formulated, where the residuals are composed of the difference between the simulated erosion profile and the experimentally measured erosion profile at different axial positions. An optimization software is used for finding the solution that minimizes the sum of the square of residuals. Figure 15 presents a schematic description of this procedure, with the chosen optimization software Dakota [98].

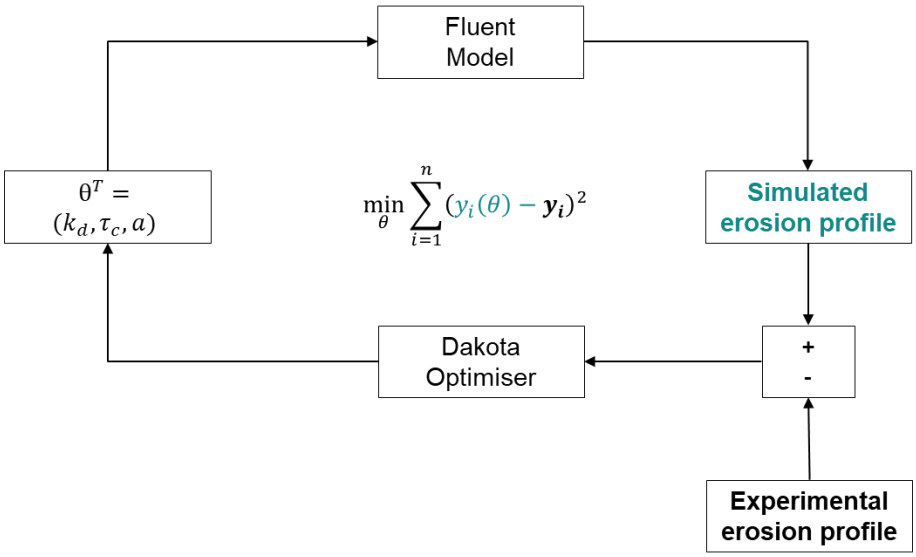

Figure 15. Schematic representation of inverse problem for erosion parameters. Reprinted from [97] (CC BY 4.0)

Publication V presents details on the implementation as well as solvers used. The procedure presented in Figure 15 is fully automated through shell scripting and Fluent journaling. The minimization solver employed was the NL2SOL solver of Dennis et al. [99]. This gradient-based solver is an adaptation of the Gauss-Newton method and offers quadratic convergence. For all cases, multiple random initial points were employed in the search to exclude convergence to local subminima.

2.2.3.4 Test Problem

Firstly, the inverse problem was studied through a test-problem. For this, the experimental erosion profiles were artificially generated with the same model used in the forward problem and random noise was added to the simulated profiles.

The test-problem gives the opportunity to explore the behavior of the implemented method with different solvers and moreover, it offers the possibility of calculation of the parameters under different experimental configurations. Because the standard deviation of the data corresponds to the chosen noise level, a statistical method for assessment of goodness of fit can be employed as discussed in Publication V.

With the test-problem the exact problem was first investigated, that is, the experimental erosion profiles were directly obtained from simulations with no additional noise. Later, artificial noise from a normal distribution with zero mean was used for producing the artificial erosion profiles.

The inverse calculation of the erosion parameter was attempted both based on the three-parameter erosion law as shown in equation (42) and the case of the exponent a fixed to unity was investigated. Additionally, the inverse calculation with multiple experiments was also investigated.

3 Summary of results

3.1 Dissolution

The dissolution model was developed for the finger-test experiments conducted with the CWTD. In Publication 1, the methodology for calculation of Sherwood numbers described in Sections 2.2.2.2 was introduced and applied for a cylindrical sample rotating in a slag bath. The aim was to establish an appropriate model for dissolution of refractory materials, as described in Section 2.2.2.1.

The flow-field simulations obtained with the Fluent model aimed calculation of parameter β of Equation (26). Thus, the grid independence test was conducted based on these values, and the results are shown in detail in Publication I. The independence of the solutions from the chosen time-step was also verified. Validation of the flow-field was based on the discussion presented in Section 2.2.2.3, here the transition from a CC flow to a TC flow was discussed for the case of infinite length cylinders. Simulations at different Reynolds number were conducted and the results are presented in Figure 16, where flow path-lines colored by the velocity magnitude are displayed. For the configuration in study, the transition to a TV flow is at a Reynolds number of 31.8, when the theoretical case of infinite length cylinders is considered.

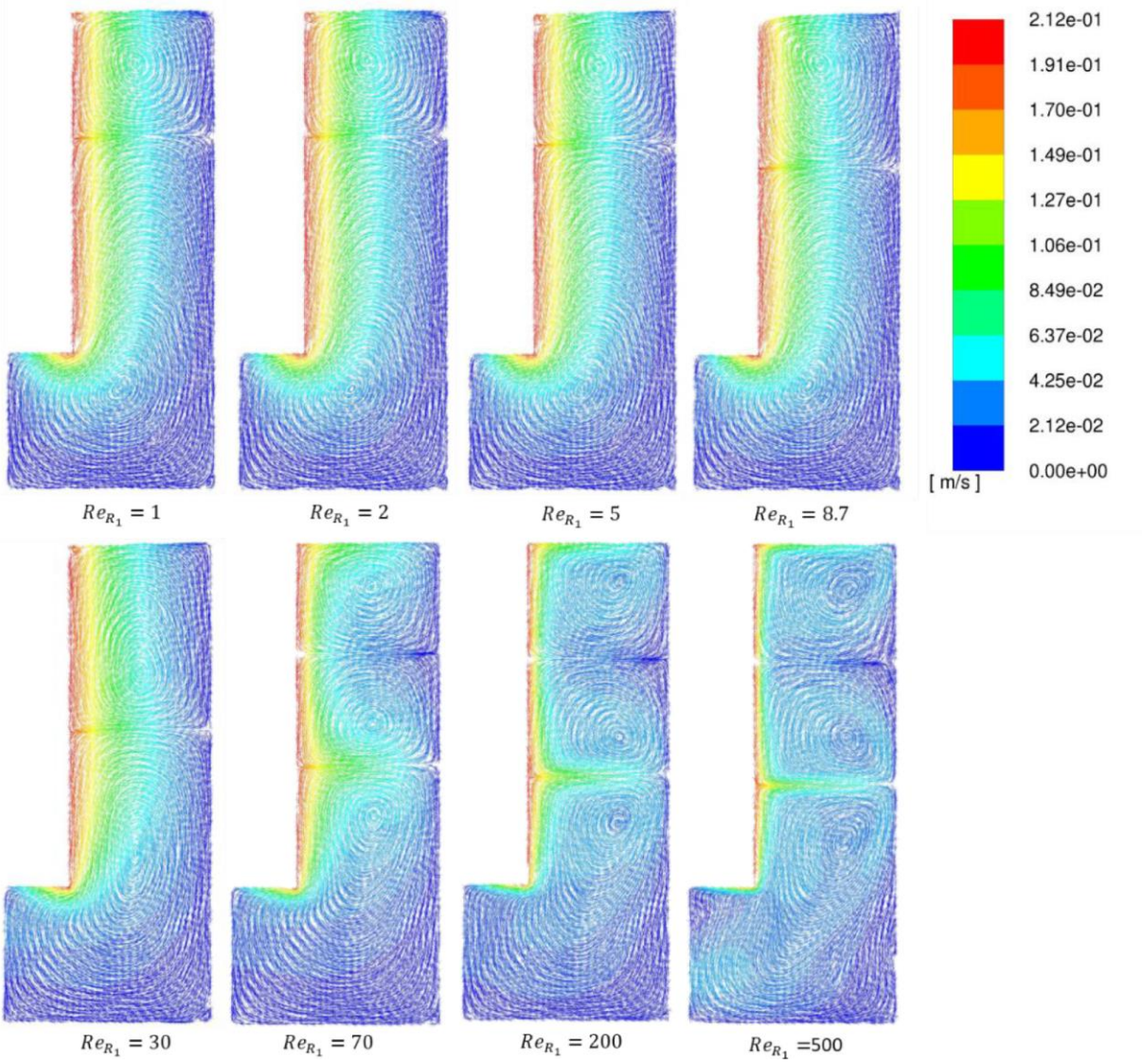

Figure 16. Flow-field for different Reynolds number. Reprinted from [42] (CC BY 4.0)

In Figure 16 it can be observed that below the calculated critical Reynolds number only two vortical structures are observable and the flow-field follows a CC behavior in the annular region, decreasing from the prescribed rotational speed at the inner cylinder to the zero at the crucible or outer cylinder. Above this critical Reynolds number, Taylor vortices appear, and the velocity distribution is no longer given by the CC flow. For all cases, it is noticed that the clearance region serves as a region for development of axial flow, induced by the rotation of the tip of the sample as was also discussed in Section 2.2.2.3.

For verification of the asymptotic boundary layer approach, we consider the cylinder mantle and disc shaped tip separately. Starting by the disc, Figure 17 presents a comparison of the area averaged Sherwood numbers obtained by Simulation with the notorious equations of Levich.

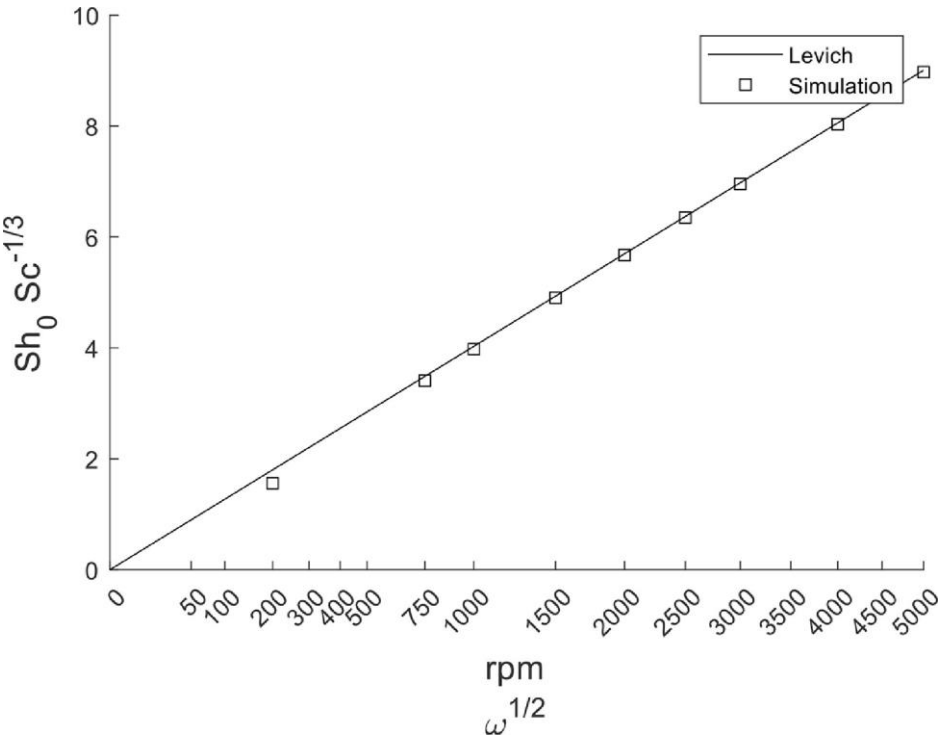

Figure 17. Average Sherwood number for rotating disc. Reprinted from [42]. (CC BY 4.0)

These results provide verification of the asymptotic boundary layer method and flow-field simulations because a good agreement between simulation results and Levich´s equation is observed, especially for the larger rotational speed. At 200 rpm a deviation is observed which is explained by the fact that the velocity boundary layer thickness is comparable to the disc radius, where the equation of Levich is expected to be inaccurate. It is important to notice that these values do not incorporate the effect of the Stefan flow because here only the Sh_0 are shown, however the corresponding corrections are shown in Publication I, where also the mass transfer coefficients are presented.

While the tip of the sample resembles the rotating disc problem, the mantle area can be compared to the case of mass or heat transfer in the rotating cylinder set-up for which some equations are available in literature. These equations are found in Publication 1, and Figure 18 presents the comparison between the values obtained by simulation and these equations. Here the equation presented by Tachibana [100]was modified by exchanging the factor $Sc^{1/4}$ by $Sc^{1/3}$, which is better suited for larger Schmidt numbers.

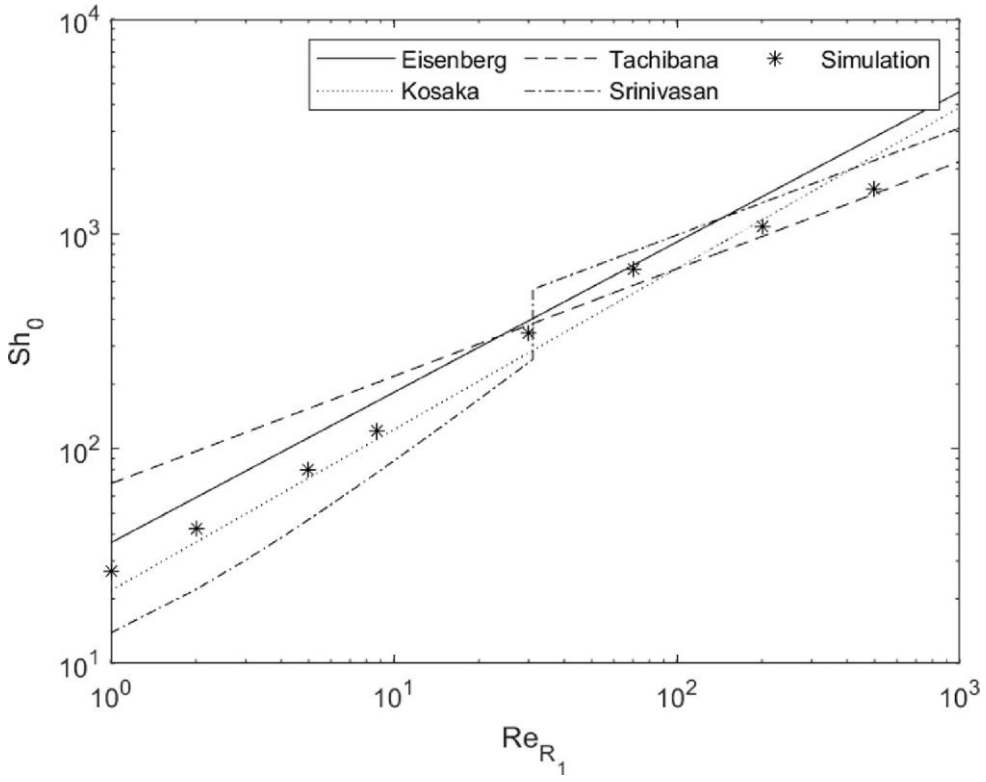

Figure 18. Average Sherwood number for cylinder mantle compared to documented equations. Reprinted from [42] (CC BY 4.0)

It is important to notice that none of the equations shown in Figure 18 considers a clearance region and all are based on cylinders of larger length. We observe that for Reynolds numbers below the critical value of 31.8 the simulation data share a slope with the equation of Kosaka and the equation of Eisenberg, being closest to the former and with an error that decreases with Reynolds number. Above the critical Reynolds number, the slope changes as the flow-field is fundamentally different and the mass transfer rate is significantly increased. The slope of the data is similar to that of the equation of Tachibana which was developed for this flow-regimen. The equation of Srinivasan also shows similar slope in this region.

After the method was verified with Publication I, the second step was application to real dissolution experiments in Publication II. Owing to the high accuracy dimensional information available from laser measurements of the corroded sample after each corrosion step, it is possible to create the geometries for simulation from this data.

Accounting for the actual corroded shape of the sample is expected to increase the accuracy between simulation and experiment due to a more accurate representation of the species boundary layer thickness. The results of this simulations can be employed for calculation of effective

binary diffusivities as discussed in Section 2.2.2.5 and more in detail in Publication II, where experiments of alumina dissolution in CAS slag are conducted. Figure 19 shows the results of curve fitting of the simulated erosion profile to the experiment.

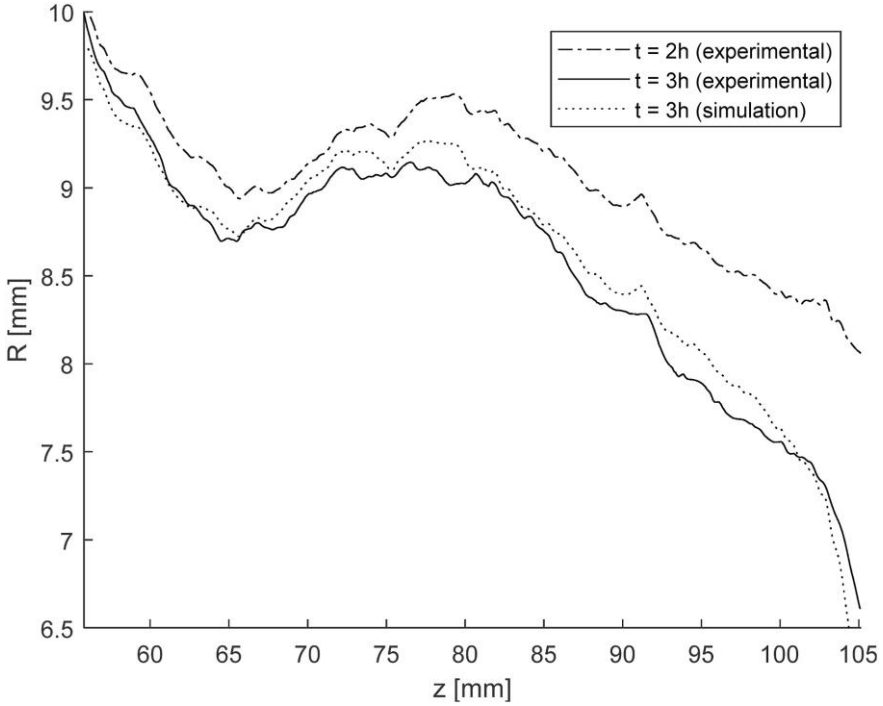

Figure 19. Simulated and experimental corrosion profiles. Reprinted from [101](CC BY 4.0)

A very good qualitative agreement can be observed in this figure for the profiles after three hours of dissolution. The value of diffusivity that was obtained was also compared to values found in the work of Cooper and Kingery [17]. Their diffusivity value was modified to account for the neglected effect of the Stefan velocity and the difference was 29%. Considering that the value of [17] is based on molecular diffusion experiments where the boundary layer is likely not to be well accounted for and given that since their publication in 1964 more accurate values for fluid properties have become available the error is surprisingly small. Furthermore, diffusivity values obtained by Confocal Laser Scanning Microscopy (CLSM) investigations reported by Burhanuddin in his doctoral dissertation [102] are in good agreement with the values obtained by simulation with a differenceof 3%. Furthermore, the value calculate from the average mass flux density differs from the curve fitting value only by 15%.

Publication III studies the case of alumina dissolution in a slag in the CaO-Al_2O_3-SiO_2-MgO (CASM) system and here the same procedure of Publication II was also applied to these experiments to obtain the values of effective binary diffusivities at three different temperatures.

Moreover, the results were also compared to those obtained by application of published Sherwood correlations and the plausibility of the results was verified by Arrhenius plot.

The methodology was applied for different experiments, including those presented in publication II and III, and additional simulations by varying the fluid properties, i.e. density and viscosity were conducted. With these results a new correlation for the average Sherwood number was formulated that includes the geometrical parameters that characterize a CWTD or finger test experiment. The influencing parameters are shown graphically in Figure 20 and the fitting of the correlation to the experimental data can be seen in Figure 21, where the data is scaled to show as a dependency of the Reynolds number only. Here $\bar{R}$ represents the average radius of the immersed sample, and the value of d is computer with this quantity.

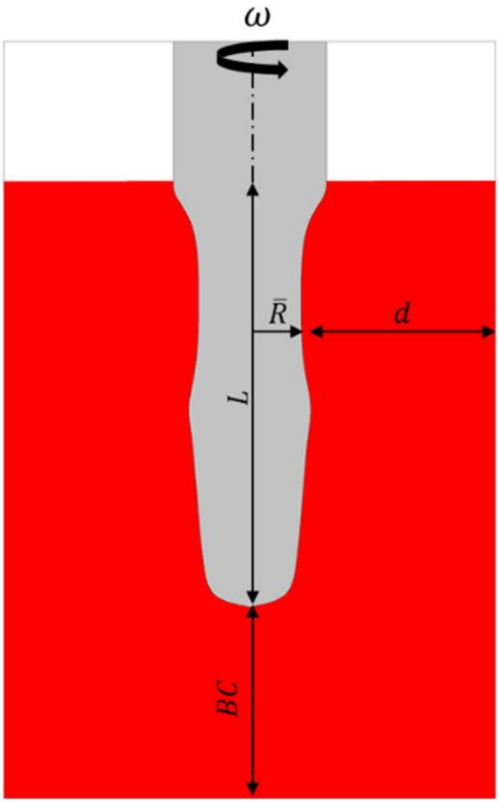

Figure 20. Influencing parameters employed for Sherwood number correlation. Reprinted from [103](CC BY 4.0)

$$Sh_d = 0.10\, Re^{0.65} Sc^{1/3} (d/\bar{R})^{1.49} (BC/L)^{0.32} \tag{43}$$

This equation is the first one derived for to the cylinder mantle in finger-test experiments and accounts for the bottom clearance as well as the gap width and length of the sample.

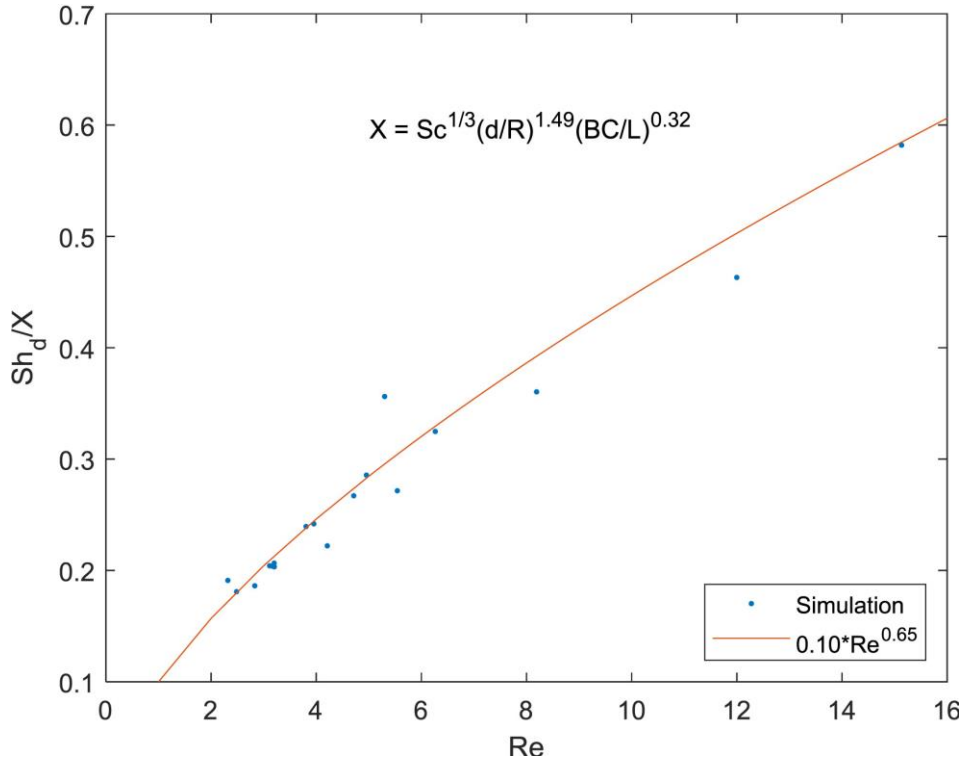

Figure 21. Fitting of correlation to values obtained by simulation. Reprinted from [103](CC BY 4.0)

3.2 Erosion

The results of the erosion investigations are detailed in Publication V. Firstly, the developed model was investigated with a test-problem. Here the erosion profile was obtained by simulation and random noise was added to mimic a real experiment as it is shown in Figure 22.

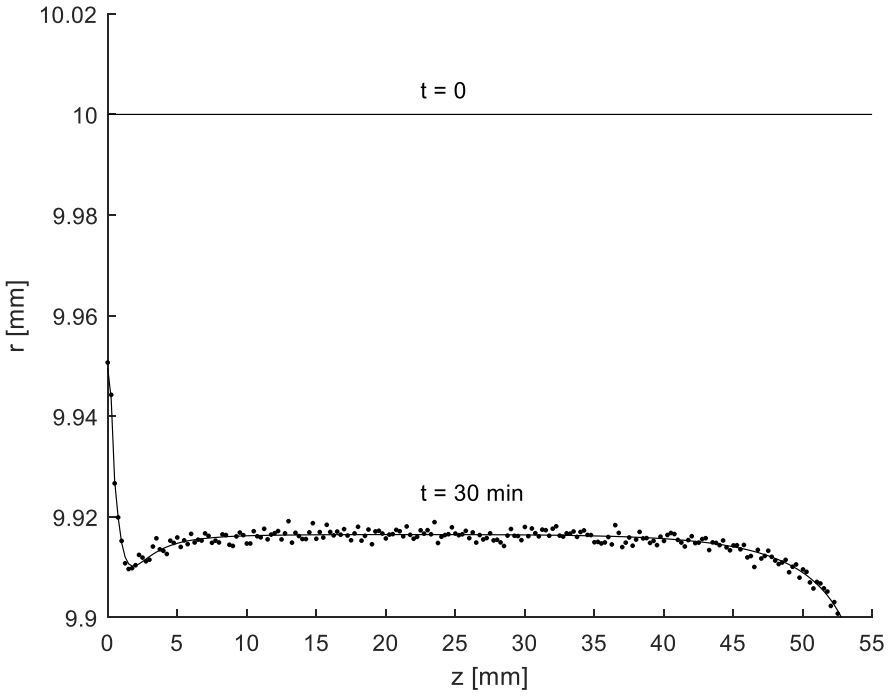

Figure 22. Simulated erosion profile and artificial experimental data. Reprinted from [97]

The results of the test-problem showed that the inverse evaluation was only possible with the exponent a of Equation (42) fixed to unity. When identification with three parameters is attempted, the solutions found are not unique and do not correspond to the design values. Moreover, during inverse calculation local subminima were encountered which highlights the necessity of using multiple random starting points. The NL2SOL solver was proven to be effective. To overcome the ill-conditioning of the three-parameter problem, the solution with multiple experiments was attempted, however this did not change the conclusions.

In Publication V, tables with the solutions for each investigated configuration are presented where also the determinant of the approximated Hessian matrix of the problem is given. It was observed that in case of inverse calculation with three erosion parameters these determinants were close to zero, which is indicative of ill-conditioning [104, p. 230].

With the conclusions obtained by the investigations of the test-problem, inverse calculation of a real erosion experiment was attempted. Here the experiments were also performed with the CWTD and the erosion of an alumina coarse grain refractory in a CASM slag was investigated. The results are shown in Figure 23, where the experimental erosion profile is shown together with the simulated profile with the parameters obtained by the inverse calculation.

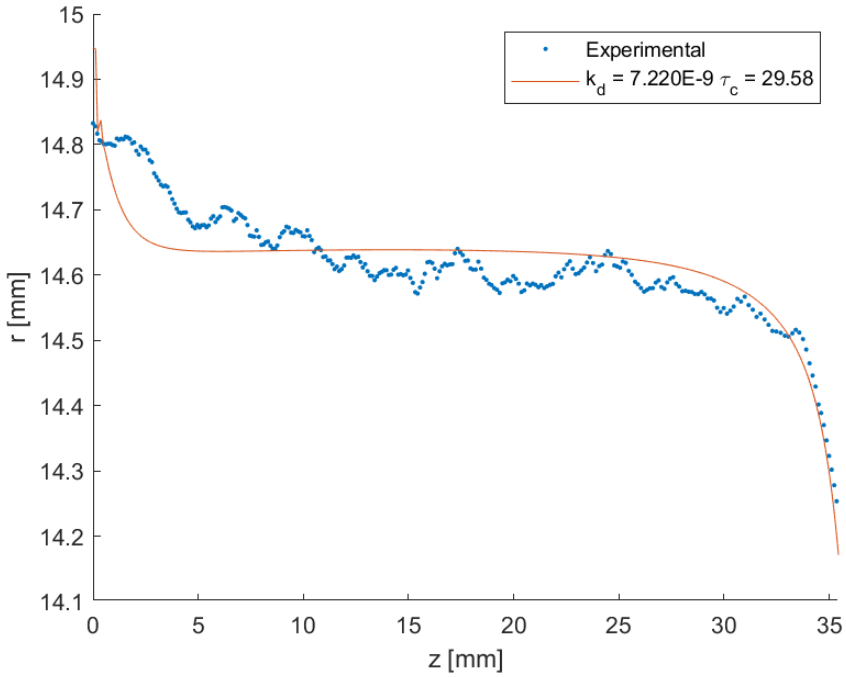

Figure 23. Solution of inverse calculation of erosion parameter of alumina coarse grain refractory. Reprinted from [97]

4 Conclusions

- A model for dissolution of refractory materials in liquid melts was established. The model is based on CFD simulations and an asymptotic boundary layer approach. The generally neglected influence of the Stefan velocity on the species boundary layer thickness and the convective part of the dissolution mass flux were considered.
- The asymptotic boundary layer approach for species transport reduced the computational needs necessary for performing simulations at large Schmidt number and the results obtained with this method were verified against documented equations.
- The dissolution profiles obtained by simulation of the CWTD agree well with those obtained experimentally from laser measurement of the corroded surfaces.
- Effective binary diffusivities were calculated with the developed method and finger test experiments and the obtained values agree with values reported in literature and others obtained independently by CLSM investigations.
- A CFD model for the erosion was established for the finger test experiment based on an erosion law obtained from the field of soil erosion. The model makes use of dynamic meshing methods to account for the geometrical change of the domain boundaries.
- A test-problem revealed the feasibility of the inverse calculation of two erosion parameters, for which the exponent of the erosion law was fixed to unity.
- The inverse problem was successfully applied to a real experiment with an alumina coarse grained ceramic in a CASM slag at high temperature.

5 References

[1] P. Lian, A. Huang, H. Gu, Y. Zou, L. Fu, and Y. Wang, "Towards prediction of local corrosion on alumina refractories driven by Marangoni convection," *Ceram Int*, vol. 44, no. 2, pp. 1675–1680, Feb. 2018, doi: 10.1016/j.ceramint.2017.10.095.

[2] J. Pötschke and C. Brüggmann, "Premature Wear of Refractories due to Marangoni-Convection," *Steel Res Int*, vol. 83, no. 7, pp. 637–644, Jul. 2012, doi: 10.1002/srin.201100294.

[3] L. F. Verdeja, R. Parra, F. Barbés Fernández, and V. Bazán, "Application of the nodal wear model to the static finger test of refractories corrosion," *Steel Grips*, vol. 3, no. 2, pp. 105–110, 2005, [Online]. Available: https://www.researchgate.net/publication/265216342

[4] L. Chen, A. Malfliet, P. T. Jones, B. Blanpain, and M. Guo, "Influence of Al2O3 Level in CaO-SiO2-MgO-Al2O3 Refining Slags on Slag/Magnesia-Doloma Refractory Interactions," *Metallurgical and Materials Transactions B: Process Metallurgy and Materials Processing Science*, vol. 50, no. 4, pp. 1822–1829, 2019, doi: 10.1007/s11663-019-01596-y.

[5] W. K. Banda, J. D. Steenkamp, and E. Matinde, "An investigation into the wear mechanisms of carbon- And silicon carbide-based refractory materials by silicomanganese alloy," *J South Afr Inst Min Metall*, vol. 120, no. 5, pp. 333–344, 2020, doi: 10.17159/2411-9717/959/2020.

[6] L. Chen *et al.*, "Effect of ZnO level in secondary copper smelting slags on slag/magnesia-chromite refractory interactions," *J Eur Ceram Soc*, vol. 36, no. 7, pp. 1821–1828, 2016, doi: 10.1016/j.jeurceramsoc.2016.02.004.

[7] L. Chen *et al.*, "The influence of ZnO in fayalite slag on the degradation of magnesia-chromite refractories during secondary Cu smelting," *J Eur Ceram Soc*, vol. 35, no. 9, pp. 2641–2650, 2015, doi: 10.1016/j.jeurceramsoc.2015.03.013.

[8] H. Um, K. Lee, K. Y. Kim, G. Shin, and Y. Chung, “Effect of carbon content of ferro-manganese alloy on corrosion behaviour of MgO-C refractory,” *Ironmaking and Steelmaking*, vol. 41, no. 1, pp. 31–37, 2014, doi: 10.1179/1743281212Y.0000000098.

[9] M. Guo *et al.*, “Degradation mechanisms of magnesia-carbon refractories by high-alumina stainless steel slags under vacuum,” *Ceram Int*, vol. 33, no. 6, pp. 1007–1018, 2007, doi: 10.1016/j.ceramint.2006.03.009.

[10] M. Guo *et al.*, “Degradation mechanisms of magnesia-chromite refractories by high-alumina stainless steel slags under vacuum conditions,” *J Eur Ceram Soc*, vol. 26, no. 16, pp. 3831–3843, 2006, doi: 10.1016/j.jeurceramsoc.2005.12.025.

[11] M. Guo *et al.*, “Interaction of Al2O3-rich slag with MgO-C refractories during VOD refining-MgO and spinel layer formation at the slag/refractory interface,” *J Eur Ceram Soc*, vol. 29, no. 6, pp. 1053–1060, 2009, doi: 10.1016/j.jeurceramsoc.2008.07.063.

[12] S. Jansson, V. Brabie, and P. Jönsson, “Corrosion mechanism of commercial doloma refractories in contact with CaO-Al2O3-SiO2-MgO slag,” *Ironmaking and Steelmaking*, vol. 35, no. 2, pp. 99–107, 2008, doi: 10.1179/030192307X231595.

[13] A. H. Bui, H. M. Ha, I. S. Chung, and H. G. Lee, “Dissolution kinetics of alumina into mold fluxes for continuous steel casting,” *ISIJ International*, vol. 45, no. 12, pp. 1856–1863, 2005, doi: 10.2355/isijinternational.45.1856.

[14] J. Jeon, Y. Kang, J. H. Park, and Y. Chung, “Corrosion-erosion behavior of MgAl2O4 spinel refractory in contact with high MnO slag,” *Ceram Int*, vol. 43, no. 17, pp. 15074–15079, 2017, doi: 10.1016/j.ceramint.2017.08.034.

[15] H. Um, K. Lee, J. Choi, and Y. Chung, “Corrosion behavior of MgO-C refractory in ferromanganese slags,” *ISIJ International*, vol. 52, no. 1, pp. 62–67, 2012, doi: 10.2355/isijinternational.52.62.

[16] G. Y. Shi, T. A. Zhang, Z. H. Dou, and L. P. Niu, “Dissolution behavior of al2o3 inclusions in cao-al2o3 based slag representing aluminothermic reduction slag,” *Crystals (Basel)*, vol. 10, no. 11, pp. 1–12, 2020, doi: 10.3390/cryst10111061.

[17] A. R. COOPER and W. D. KINGERY, “Dissolution in Ceramic Systems: I, Molecular Diffusion, Natural Convection, and Forced Convection Studies of Sapphire Dissolution in Calcium Aluminum Silicate,” *Journal of the American Ceramic Society*, vol. 47, no. 1, pp. 37–43, Jan. 1964, doi: 10.1111/j.1151-2916.1964.tb14638.x.

[18] S. Jansson, V. Brabie, and P. Jonsson, “Corrosion mechanism and kinetic behaviour of MgO-C refractory material in contact with CaO-Al2O3-SiO2-MgO slag,” *Scandinavian Journal of Metallurgy*, vol. 34, no. 5, pp. 283–292, Oct. 2005, doi: 10.1111/j.1600-0692.2005.00748.x.

[19] W. E. Lee and S. Zhang, “Melt corrosion of oxide and oxide-carbon refractories,” *International Materials Reviews*, vol. 44, no. 3, pp. 77–104, 1999, doi: 10.1179/095066099101528234.

[20] C. Reynaert, E. Sniezek, and J. Szczerba, “CORROSION TESTS FOR REFRACTORY MATERIALS INTENDED FOR THE STEEL INDUSTRY - A REVIEW,” *Ceramics - Silikaty*, vol. 64, no. 3, pp. 278–288, Mar. 2020, doi: 10.13168/cs.2020.0017.

[21] D. Kim, H. T. Kim, S. S. Ryu, and H. J. Kim, “Microstructure changes of aluminum titanate refractory doped SiO2 and ZrO2 in molten steel,” *Journal of Korean Institute of Metals and Materials*, vol. 53, no. 2, pp. 116–122, 2015, doi: 10.3365/KJMM.2015.53.2.116.

[22] K. H. Sandhage and G. J. Yurek, “Direct and Indirect Dissolution of Sapphire in Calcia–Magnesia–Alumina–Silica Melts: Dissolution Kinetics,” *Journal of the American Ceramic Society*, vol. 73, no. 12, pp. 3633–3642, 1990, doi: 10.1111/j.1151-2916.1990.tb04269.x.

[23] I. Kasimagwa, V. Brabie, and P. G. Jönsson, “Slag corrosion of MgO–C refractories during secondary steel refining,” *Ironmaking & Steelmaking*, vol. 41, no. 2, pp. 121–131, Feb. 2014, doi: 10.1179/1743281213Y.0000000110.

[24] M. Eisenberg, C. W. Tobias, and C. R. Wilke, “Ionic Mass Transfer and Concentration Polarization at Rotating Electrodes,” *J Electrochem Soc*, vol. 101, no. 6, p. 306, 1954, doi: 10.1149/1.2781252.

[25] A. P. A. P. Campbell, K. A. K. A. Pericleous, and M. Cross, “Modelling of Freeze Layers and Refractory Wear in Direct Smelting Processes,” in *Proceedings - Ironmaking Conference*, 2002, vol. 29, pp. 479–491.

[26] E. Partheniades, “Erosion and Deposition of Cohesive Soils,” *Journal of the Hydraulics Division*, vol. 91, no. 1, pp. 105–139, Jan. 1965, doi: 10.1061/JYCEAJ.0001165.

[27] A. Huang, H. Gu, M. Zhang, N. Wang, T. Wang, and Y. Zou, “Mathematical Modeling on Erosion Characteristics of Refining Ladle Lining with Application of Purging Plug,” *Metallurgical and Materials Transactions B*, vol. 44, no. 3, pp. 744–749, Jun. 2013, doi: 10.1007/s11663-013-9805-0.

[28] Q. Wang, C. Liu, L. Pan, Z. He, G. Li, and Q. Wang, “Numerical Understanding on Refractory Flow-Induced Erosion and Reaction-Induced Corrosion Patterns in Ladle Refining Process,” *Metallurgical and Materials Transactions B: Process Metallurgy and Materials Processing Science*, vol. 53, no. 3, pp. 1617–1630, Jun. 2022, doi: 10.1007/s11663-022-02471-z.

[29] Q. Wang *et al.*, “Quantitative Characterization of Flow-Induced Erosion of Tundish Refractory Lining via Water Model Experiment and Numerical Simulation,” *Metallurgical and Materials Transactions B: Process Metallurgy and Materials Processing Science*, vol. 52, no. 5, pp. 3265–3275, Oct. 2021, doi: 10.1007/s11663-021-02254-y.

[30] Q. Li, M. Li, S. B. Kuang, and Z. Zou, “Understanding Characteristic of Abrasion of Refractory Lining Caused by Bath Oscillation in BOF Steelmaking,” *JOM*, vol. 68, no. 12, pp. 3126–3133, Dec. 2016, doi: 10.1007/s11837-016-2078-8.

[31] L. Shao and H. Saxén, “Numerical Prediction of Iron Flow and Bottom Erosion in the Blast Furnace Hearth,” *Steel Res Int*, vol. 83, no. 9, pp. 878–885, Sep. 2012, doi: 10.1002/srin.201200041.

[32] F. Karouni, B. P. Wynne, J. Talamantes-Silva, and S. Phillips, “A Parametric Study on the Effects of Process Conditions on Dehydrogenation, Wall Shear and Slag Entrainment in the Vacuum Arc Degasser Using Mathematical Modelling,” *ISIJ International*, vol. 58, no. 9, pp. 1679–1686, Sep. 2018, doi: 10.2355/isijinternational.ISIJINT-2018-254.

[33] H. Ling, L. Zhang, and C. Liu, “Effect of snorkel shape on the fluid flow during RH degassing process: mathematical modelling,” *Ironmaking & Steelmaking*, vol. 45, no. 2, pp. 145–156, Feb. 2018, doi: 10.1080/03019233.2016.1248700.

[34] S. K. Dash, D. N. Jha, S. K. Ajmani, and A. Upadhyaya, “Optimisation of taphole angle to minimise flow induced wall shear stress on the hearth,” *Ironmaking and Steelmaking*, vol. 31, no. 3, pp. 207–215, 2004, doi: 10.1179/030192304225012114.

[35] V. Kircher, Burhanuddin, and H. Harmuth, “Design, operation and evaluation of an improved refractory wear testing technique,” *Measurement*, vol. 178, p. 109429, Jun. 2021, doi: 10.1016/j.measurement.2021.109429.

[36] Burhanuddin, J. Guarco, H. Harmuth, and S. Vollmann, “Application of an improved testing device for the study of alumina dissolution in silicate slag,” *J Eur Ceram Soc*, vol. 42, no. 8, pp. 3652–3659, Jul. 2022, doi: 10.1016/j.jeurceramsoc.2022.02.056.

[37] H. Schlichting and K. Gersten, *Boundary-Layer Theory*. Berlin, Heidelberg: Springer Berlin Heidelberg, 2017. doi: 10.1007/978-3-662-52919-5.

[38] J. Stefan, “Über die Verdampfung und die Auflösung als Vorgänge der Diffusion,” *Sitzungsberichte der kaiserlichen Akademie der Wissenschaften. Mathematisch-naturwissenschaftliche Klasse*, vol. 98 2a, pp. 1418–1442, 1889, [Online]. Available: www.biologiezentrum.at

[39] B. Y. B. Levich, “The theory of concentration polarisation,” 1947, [Online]. Available: https://pubs.rsc.org/is/content/articlelanding/1947/df/df9470100037/unauth#!divAbstract

[40] H. Schlichting and K. Gersten, *Boundary-Layer Theory*, 9th ed. Berlin, Heidelberg: Springer Berlin Heidelberg, 2017. doi: 10.1007/978-3-662-52919-5.

[41] M. J. Lighthill, “Contributions to the theory of heat transfer through a laminar boundary layer,” *Proc R Soc Lond A Math Phys Sci*, vol. 202, no. 1070, pp. 359–377, Aug. 1950, doi: 10.1098/rspa.1950.0106.

[42] J. Guarco, H. Harmuth, and S. Vollmann, “Method for determination of mass transfer coefficients for dissolution of dense ceramics in liquid slags,” *Int J Heat Mass Transf*, vol. 186, p. 122494, May 2022, doi: 10.1016/j.ijheatmasstransfer.2021.122494.

[43] J. Newman and K. E. Thomas-Alyea, *Electrochemical Systems*, 3rd ed. Wiley, 2004.

[44] K. Gersten and H. Herwig, *Grundlagen der Impuls-, Wärme- und Stoffübertragung aus asymptotischer Sicht*. 1992.

[45] H. J. Merk, “Mass transfer in laminar boundary layers calculated by means of a perturbation method,” *Applied Scientific Research*, vol. 8, no. 1, pp. 237–260, 1959, doi: 10.1007/BF00411753.

[46] A. Acrivos, “The asymptotic form of the laminar boundary-layer mass-transfer rate for large interfacial velocities,” *J Fluid Mech*, vol. 12, no. 3, pp. 337–357, 1962, doi: 10.1017/S0022112062000257.

[47] Lord Rayleigh, “On the Dynamics of Revolving Fluids,” *Proceedings of the Royal Society of London. Series A, Containing Papers of a Mathematical and Physical Character*, vol. 93, no. 648, pp. 148–154, 1917, [Online]. Available: http://www.jstor.org/stable/93794

[48] S. Chandrasekhar, *Hydrodynamic and Hydromagnetic Stability*. New York: Dover Publications, Inc., 1961. doi: 10.1017/S0022112062210592.

[49] H. L. Swinney and J. P. Gollub, *Hydrodyanmic instabilities and the transition to turbulence.*, 2nd ed. Springer Berlin Heidelberg, 1981. doi: 10.1016/0031-9201(83)90038-9.

[50] G. I. Taylor, “Stability of a Viscous Liquid Contained between Two Rotating Cylinders,” *Philosophical Transactions of the Royal Society A: Mathematical, Physical and Engineering Sciences*, vol. 223, no. 605–615, pp. 289–343, 1923, doi: 10.1098/rsta.1923.0008.

[51] Y. Takeda, “Quasi-periodic state and transition to turbulence in a rotating Couette system,” *J Fluid Mech*, vol. 389, pp. 81–99, 1999, doi: 10.1017/S0022112099005091.

[52] K. N. Astill, “Studies of the developing flow between concentric cylinders with the inner cylinder rotating,” *J Heat Transfer*, vol. 86, no. 3, pp. 383–391, 1964, doi: 10.1115/1.3688703.

[53] J. Walowit, S. Tsao, and R. C. DiPrima, “Stability of Flow Between Arbitrarily Spaced Concentric Cylindrical Surfaces Including the Effect of a Radial Temperature Gradient,” *J Appl Mech*, vol. 31, no. 4, pp. 585–593, Dec. 1964, doi: 10.1115/1.3629718.

[54] K. S. Ball and B. Farouk, “A flow visualisation study of the effects of buoyancy on Taylor vortices,” *Physics of Fluids A*, vol. 1, no. 9, pp. 1502–1507, 1989, doi: 10.1063/1.857328.

[55] M. Ali and P. D. Weidman, “On the stability of circular Couette flow with radial heating,” *J Fluid Mech*, vol. 220, no. 12, pp. 53–84, Nov. 1990, doi: 10.1017/S0022112090003184.

[56] J. Chen and J. Kuo, “The linear stability of steady circular Couette flow with a small radial temperature gradient,” *Physics of Fluids A: Fluid Dynamics*, vol. 2, no. 9, pp. 1585–1591, Sep. 1990, doi: 10.1063/1.857565.

[57] T. Ma and S. Wang, “Boundary-layer and interior separations in the Taylor-Couette-Poiseuille flow,” *J Math Phys*, vol. 50, no. 3, 2009, doi: 10.1063/1.3093268.

[58] C. Kang, K. S. Yang, and I. Mutabazi, “Thermal effect on large-aspect-ratio Couette-Taylor system: Numerical simulations,” *J Fluid Mech*, vol. 771, pp. 57–78, 2015, doi: 10.1017/jfm.2015.151.

[59] J. H. Ng, R. K. Jaiman, and T. T. Lim, “Interaction dynamics of longitudinal corrugations in Taylor-Couette flows,” *Physics of Fluids*, vol. 30, no. 9, 2018, doi: 10.1063/1.5046710.

[60] H. A. Snyder, “Stability of rotating Couette flow. I. Asymmetric waveforms,” *Physics of Fluids*, vol. 11, no. 4, pp. 728–734, 1968, doi: 10.1063/1.1691991.

[61] H. A. Snyder, “Stability of rotating Couette flow. II. Comparison with numerical results,” *Physics of Fluids*, vol. 11, no. 8, pp. 1599–1605, 1968, doi: 10.1063/1.1692167.

[62] G. de Vahl Davis and R. W. Thomas, “Natural convection between concentric vertical cylinders,” *Physics of Fluids*, vol. 12, no. 12, 1969, doi: 10.1063/1.1692437.

[63] J. E. Burkhalter and E. L. Koschmieder, “Steady supercritical Taylor vortices after sudden starts,” *Physics of Fluids*, vol. 17, no. 11, pp. 1929–1935, 1974, doi: 10.1063/1.1694646.

[64] J. E. Burkhalter and E. L. Koschmieder, “Steady supercritical Taylor vortex flow,” *J Fluid Mech*, vol. 58, no. 3, pp. 547–560, 1973, doi: 10.1017/S0022112073002326.

[65] I. G. Choi and S. A. Korpela, “Stability of the conduction regime of natural convection in a tall vertical annulus,” *J Fluid Mech*, vol. 99, no. 4, pp. 725–738, 1980, doi: 10.1017/S0022112080000869.

[66] R. C. DiPrima, P. M. Eagles, and B. S. Ng, “The effect of radius ratio on the stability of Couette flow and Taylor vortex flow,” *Physics of Fluids*, vol. 27, no. 10, p. 2403, 1984, doi: 10.1063/1.864544.

[67] C. D. Andereck, S. S. Liu, and H. L. Swinney, “Flow regimes in a circular Couette system with independently rotating cylinders,” *J Fluid Mech*, vol. 164, no. 1986, pp. 155–183, Mar. 1986, doi: 10.1017/S0022112086002513.

[68] T. B. Benjamin, “Bifurcation Phenomena in Steady Flows of a Viscous Fluid - 1, 2.,” *Proc R Soc London Ser A*, vol. 359, no. 1696, pp. 1–43, 1978.

[69] M. Gorman and H. L. Swinney, “Spatial and temporal characteristics of modulated waves in the circular Couette system,” *J Fluid Mech*, vol. 117, pp. 123–142, 1982, doi: 10.1017/S0022112082001554.

[70] T. B. Benjamin and T. Mullin, “Anomalous Modes in the Taylor Experiment.,” *Proc R Soc Lond A Math Phys Sci*, vol. 377, no. 1770, pp. 221–249, 1981, doi: 10.1098/rspa.1981.0122.

[71] T. Watanabe and Y. Toya, “Vertical Taylor-Couette flow with free surface at small aspect ratio,” *Acta Mech*, vol. 223, no. 2, pp. 347–353, 2012, doi: 10.1007/s00707-011-0569-9.

[72] T. Watanabe, H. Furukawa, and Y. Toya, “Transition of free-surface flow modes in taylor-couette system,” *J Vis (Tokyo)*, vol. 10, no. 3, pp. 309–316, 2007, doi: 10.1007/BF03181698.

[73] T. Watanabe, H. Furukawa, M. Aoki, and I. Nakamura, “Visualization of Sudden-start Flow between Two Concentric Rotating Cylinders with Finite Length,” *J Vis (Tokyo)*, vol. 4, no. 3, pp. 223–230, 2001, doi: 10.1007/BF03182582.

[74] M. Lücke, M. Mihelcic, and K. Wingerath, “Front propagation and pattern formation of Taylor vortices growing into unstable circular Couette flow,” *Phys Rev A (Coll Park)*, vol. 31, no. 1, pp. 396–409, 1985, doi: 10.1103/PhysRevA.31.396.

[75] I. Nakamura and Y. Toya, “Existence of extra vortex and twin vortex of anomalous mode in Taylor vortex flow with a small aspect ratio,” *Acta Mech*, vol. 117, no. 1–4, pp. 33–46, Mar. 1996, doi: 10.1007/BF01181035.

[76] Y. Toya, I. Nakamura, S. Yamashita, and Y. Ueki, “An experiment on a taylor vortex flow in a gap with a small aspect ratio bifurcation of flows in an asymmetric system,” *Acta Mech*, vol. 102, no. 1–4, pp. 137–148, Mar. 1994, doi: 10.1007/BF01178523.

[77] V. Sobolík, B. Izrar, F. Lusseyran, and S. Skali, “Interaction between the Ekman layer and the Couette-Taylor instability,” *Int J Heat Mass Transf*, vol. 43, no. 24, pp. 4381–4393, 2000, doi: 10.1016/S0017-9310(00)00067-3.

[78] O. Czarny, E. Serre, P. Bontoux, and R. M. Lueptow, “Ekman vortices and the centrifugal instability in counter-rotating cylindrical Couette flow,” *Theor Comput Fluid Dyn*, vol. 18, no. 2–4, pp. 151–168, 2004, doi: 10.1007/s00162-004-0140-6.

[79] O. Czarny, E. Serre, P. Bontoux, and R. M. Lueptow, “Interaction between Ekman pumping and the centrifugal instability in Taylor-Couette flow,” *Physics of Fluids*, vol. 15, no. 2, pp. 467–477, 2003, doi: 10.1063/1.1534108.

[80] M. J. Burin *et al.*, “Reduction of Ekman circulation within Taylor-Couette flow,” *Exp Fluids*, vol. 40, no. 6, pp. 962–966, 2006, doi: 10.1007/s00348-006-0132-y.

[81] J. M. Lopez, F. Marques, and M. Avila, “The Boussinesq approximation in rapidly rotating flows,” *J Fluid Mech*, vol. 737, pp. 56–77, 2013, doi: 10.1017/jfm.2013.558.

[82] A. Recktenwald, M. Lücke, and H. W. Müller, “Taylor vortex formation in axial throughflow: Linear and weakly nonlinear analysis,” *Phys Rev E*, vol. 48, no. 6, pp. 4444–4454, Dec. 1993, doi: 10.1103/PhysRevE.48.4444.

[83] H. Belkadi, Y. Laghouati, V. Sobolik, H. Oualli, and A. Bouabdallah, “Axial Flow Effect on the Stability of Circular Couette Flow,” *Journal of Applied Fluid Mechanics*, vol. 15, no. 1, pp. 271–281, 2022, doi: 10.47176/jafm.15.01.33113.

[84] K. Kataoka, H. Doi, and T. Komai, “Heat/mass transfer in taylor vortex flow with constant axial flow rates,” *Int J Heat Mass Transf*, vol. 20, no. 1, pp. 57–63, 1977, doi: 10.1016/0017-9310(77)90084-9.

[85] R. C. DiPrima and A. Pridor, “Stability of viscous flow between rotating concentric cylinders with an axial flow.,” vol. 366, pp. 555–573, 1979.

[86] F. Tachibana and S. Fukui, “Convective Heat Transfer of the Rotational and Axial Flow between Concentric Cylinders,” *Bulletin of JSME*, vol. 7, no. 26, 1964.

[87] M. A. Dominguez-Lerma, G. Ahlers, and D. S. Cannell, “Marginal stability curve and linear growth rate for rotating Couette-Taylor flow and Rayleigh-Bénard convection,” *Physics of Fluids*, vol. 27, no. 4, pp. 856–860, 1984, doi: 10.1063/1.864714.

[88] D. G. Sceaeffer, “Qualitative analysis of a model for boundary effects in the Taylor problem,” *Mathematical Proceedings of the Cambridge Philosophical Society*, vol. 87, no. 2, pp. 307–337, 1980, doi: 10.1017/S0305004100056759.

[89] U. T. Bödewadt, “Die Drehströmung über festem Grunde,” *ZAMM - Journal of Applied Mathematics and Mechanics / Zeitschrift für Angewandte Mathematik und Mechanik*, vol. 20, no. 5, pp. 241–253, 1940, doi: 10.1002/zamm.19400200502.

[90] T. von Karman, “On laminar and turbulent friction,” *Zeitschrift für angewandte Mathematik un Mechanik*, vol. 1, no. 4, 1921, doi: https://resolver.caltech.edu/CaltechAUTHORS:20140804-114256964.

[91] V. W. Ekman, “On the Influence of the Earth’s Rotation on Ocean-Currents,” *Ark. Mat. Astr. Fys.*, vol. 2, no. 11. pp. 1–52, 1905. [Online]. Available: http://www.aos.princeton.edu/WWWPUBLIC/gkv/history/general.html

[92] W. G. Cochran, “The flow due to a rotating disc,” *Mathematical Proceedings of the Cambridge Philosophical Society*, vol. 30, no. 3, pp. 365–375, 1934, doi: 10.1017/S0305004100012561.

[93] V. G. Levich, *Physicochemical hydrodynamics*. Prentice-Hall, Inc., 1962. doi: 10.1021/ed040pA827.2.

[94] G. D. Raithby and K. G. T. Hollands, “A General Method of Obtaining Approximate Solutions to Laminar and Turbulent Free Convection Problems,” 1975, pp. 265–315. doi: 10.1016/S0065-2717(08)70076-5.

[95] F. P. Incropera, D. P. DeWitt, T. L. Bergman, and A. S. Lavine, *Fundamentals of Heat and Mass Transfer*, 6th ed. Wiley, 2007.

[96] A.-S. T. Al-Madhhachi, G. J. Hanson, G. A. Fox, A. K. Tyagi, and R. Bulut, “Measuring Soil Erodibility Using a Laboratory ‘Mini’ JET,” *Trans ASABE*, vol. 56, no. 3, pp. 901–910, Jul. 2013, doi: 10.13031/trans.56.9742.

[97] J. Guarco, S. Vollmann, H. Harmuth, and Burhanuddin, “Method for inverse calculation of erosion parameters in slag-refractory systems,” *Materials Today Communications (Under-Review)*, 2022.

[98] T. M. W. Brian M. Adams, Mohamed S. Ebeida, Michael S. Eldred, John D. Jakeman, Laura P. Swiler, J. Adam Stephens, Dena M. Vigil, *Dakota, A Multilevel Parallel Object-Oriented Framework for Design Optimization, Parameter Estimation, Uncertainty Quantification, and Sensitivity Analysis: Version 6.2 User’s Manual*. 2015.

[99] J. E. Dennis, D. M. Gay, and R. E. Walsh, “An Adaptive Nonlinear Least-Squares Algorithm,” *ACM Transactions on Mathematical Software*, vol. 7, no. 3, pp. 348–368, Sep. 1981, doi: 10.1145/355958.355965.

[100] F. Tachibana, S. Fukui, and H. Mitsumura, “Heat Transfer in an Annulus with an Inner Rotating Cylinder,” *Transactions of the Japan Society of Mechanical Engineers*, vol. 25, no. 156, pp. 788–792, 1959, doi: 10.1299/kikai1938.25.788.

[101] J. Guarco, Burhanuddin, S. Vollmann, and H. Harmuth, “Method for determination of effective binary diffusivities in dissolution of dense ceramic materials,” *Ceram Int*, vol. 48, no. 6, pp. 7456–7463, Mar. 2022, doi: 10.1016/j.ceramint.2021.11.264.

[102] Burhanuddin, “Experimental studies of alumina and magnesia dissolution in silicate and aluminate melts,” Doctoral Dissertation, Montanuniversität, 2022.

[103] J. Guarco, Burhanuddin, S. Vollmann, and H. Harmuth, “Sherwood correlation for finger-test experiments,” *Results in Engineering*, vol. 15, p. 100610, Sep. 2022, doi: 10.1016/j.rineng.2022.100610.

[104] R. C. Aster, B. Borchers, and C. H. Thurber, *Parameter estimation and inverse problems*. Elsevier Inc., 2013. doi: 10.1016/C2009-0-61134-X.

6 List of publications

Journal article I

J. Guarco, H. Harmuth, and S. Vollmann, “Method for determination of mass transfer coefficients for dissolution of dense ceramics in liquid slags,” *International Journal of Heat and Mass Transfer*, vol. 186, p. 122494, May 2022, doi: 10.1016/j.ijheatmasstransfer.2021.122494.

Journal article II

J. Guarco, Burhanuddin, S. Vollmann, and H. Harmuth, “Method for determination of effective binary diffusivities in dissolution of dense ceramic materials,” *Ceramics International*, vol. 48, no. 6, pp. 7456–7463, Mar. 2022, doi: 10.1016/j.ceramint.2021.11.264.

Journal article III

Burhanuddin, J. Guarco, H. Harmuth, and S. Vollmann, “Application of an improved testing device for the study of alumina dissolution in silicate slag,” *Journal of the European Ceramic Society*, vol. 42, no. 8, pp. 3652–3659, Jul. 2022, doi: 10.1016/j.jeurceramsoc.2022.02.056.

Journal article IV

J. Guarco, Burhanuddin, S. Vollmann, and H. Harmuth, “Sherwood correlation for finger-test experiments,” *Results in Engineering*, vol. 15, p. 100610, Sep. 2022, doi: 10.1016/j.rineng.2022.100610.

Journal article V

J. Guarco, S. Vollmann, H. Harmuth, and Burhanuddin, “Method for inverse calculation of erosion parameters in slag-refractory systems,” *Materials Today Communications (Under-Review)*, 2022.

Contribution of the author to the publications

Publication	Conceptualization and planning	Simulations	Analysis and interpretation	Manuscript preparation
I	90%	100%	90%	75%
II	90%	100%	90%	80%
III	0%	100%	30%	0%
IV	100%	100%	80%	80%
V	100%	100%	90%	90%

Author Burhanuddin conducted the experiments supporting publications II, III, and V.

7 Appended publications

7.1 Publication I

Method for determination of mass transfer coefficients for dissolution of dense ceramics in liquid slags

Jerónimo Guarco, Harald Harmuth, Sandra Vollmann

International Journal of Heat and Mass Transfer 186 (2022) 122494

Contents lists available at ScienceDirect

International Journal of Heat and Mass Transfer

journal homepage: www.elsevier.com/locate/hmt

Method for determination of mass transfer coefficients for dissolution of dense ceramics in liquid slags

Jerónimo Guarco*, Harald Harmuth, Sandra Vollmann

Chair of Ceramics, Montanuniversität Leoben, Peter-Tunner Straße 5, 8700 Leoben, Austria

ARTICLE INFO

Article history:
Received 7 June 2021
Revised 5 October 2021
Accepted 26 December 2021
Available online 4 January 2022

Keywords:
CFD
ACFD
Mass transfer
Dissolution
Large Schmidt systems

ABSTRACT

This paper presents a numerical method to determine the mass transfer coefficients in the dissolution of dense ceramics in liquid slags. Simulations are based on a typical rotating finger test as the experimental set-up, where a cylindrical sample is immersed in a slag bath and rotated with a constant angular speed. CFD simulations of the flow field are conducted using the volume of fluid method to incorporate both the slag and air phases. Owing to the very large Schmidt number of the arrangement and to avoid using extremely fine meshes, an asymptotic boundary layer approach is employed. This approach allows for the calculation of local, steady-state mass transfer coefficients along the sample in a postprocessing step without resorting to solving the species transport equation within the CFD calculations. The method is verified by comparing the results to those obtained via well-established equations. Resultant mass transfer coefficients are discussed with respect to values obtained from mass transfer equations in literature. The presented approach serves as an effective calculation method for the mass transfer coefficient and offers the opportunity to obtain the inverse calculation of diffusivities in systems where the Schmidt number reaches large values.

1. Introduction

This work presents a method to determine mass transfer coefficients for the dissolution of dense ceramics in slag systems during the rotating finger test. The dissolution of dense ceramics has been studied experimentally by many authors, who aimed to calculate the binary diffusivities of the ceramic materials in different slag systems [1–3]. To ensure the correct calculation of diffusivities, accurate computation of the mass transfer coefficients is necessary. To this end, authors employ different equations derived from theory and experimental observations of arrangements that are similar to their experimental set-ups. Among such approaches, it is common to turn to equations describing heat transfer based on a heat/mass transfer analogy. However, such an analogy is not always valid owing to two features that can hinder its applicability. Firstly, the dissolution of the material causes the interface between the liquid and solid to move, a phenomenon that does not occur during pure heat transfer. Secondly, the movement of this interface can have an effect on the thickness of the hydrodynamic boundary layer which directly affects the mass transfer coefficients. Regardless of whether the investigations are based on heat or mass transfer, the derived equations are a function of the Prandtl or Schmidt number with a power-law dependency. The magnitude of the numbers for which this dependency is obtained is frequently much lower than the high Schmidt numbers observed in the dissolution of ceramics in slags.

There are currently no equations that are directly applicable to the typical rotating finger test investigated in this work. Experimental investigations of such a test have been conducted by Kosaka and Minowa; [4] however, the Schmidt numbers they observed are much lower than those considered here. Moreover, an approximation of the rotating finger test by an annular region of infinite length could be conceived considering the large number of investigations into this configuration owing to the appearance of the centrifugal instabilities. For example, Tachibana et al. [5] present an equation to determine heat transfer coefficients for a flow regimen known as the Taylor-Couette regime. Eisenberg et al. [6] studied a similar set-up with an annular region. However, the finger test is characterized by a clearance to the bottom of the crucible which means that these equations are not directly applicable to our study.

In this work, we develop a methodology that considers all the aforementioned effects and that is also applicable to the high Schmidt numbers frequently found in typical ceramic/slag systems. Moreover, we utilize the characteristic high Schmidt numbers to

* Corresponding author.
E-mail address: jeronimo.guarco@unileoben.ac.at (J. Guarco).

https://doi.org/10.1016/j.ijheatmasstransfer.2021.122494

List of symbols

j_D..	diffusive flux ($kg{\cdot}m^2{\cdot}s^{-1}$)
j_t..	*gross mass flux* ($kg{\cdot}m^2{\cdot}s^{-1}$)
μ.	*dynamic viscosity*
ρ..	*density*
σ..	*surface tension*
λ..	*thermal conductivity*
ν.. $\frac{\mu}{\rho}$	*kinematic viscosity*
c_p..	*heat capacity*
D..	*effective binary diffusivity* ($m^2{\cdot}s^{-1}$)
c	*concentration* ($kg{\cdot}m^{-3}$)
w..	*mass fraction*
x..	*direction along surface*
y..	*direction normal to surface*
u..	*velocity tangential to surface*
v..	*velocity normal to surface*
r..	*radial direction*
z..	*axial direction*
v_r..	*radial velocity*
v_z..	*axial velocity*
v_θ..	*swirl velocity*
Ω..	*rotational speed* (rad s^{-1})
$\vec{v}$..	*velocity vector*
v_w..	*Stefan velocity*
β..	$\frac{\partial u}{\partial y}$
δ..	*velocity boundary layer thickness*
δ_c..	*species boundary layer thickness*
τ..	*wall shear stress (Pa)*
R_1..	*radius of the sample*
R_2..	*radius of the crucible*
d.	$R_2 - R_1$ *gap width*
η.	R_1/R_2 *radii ratio*
$\mathcal{R}$..	*radius of surface of revolution*
L..	*characteristic length*
Δc	$c_s - c_\infty$
B	$(w_s - w_\infty)/(1 - w_s)$
k_c..	*mass transfer coefficient*
h..	*heat transfer coefficient*
Re.. $\frac{\Omega R_1 L}{\nu}$	*Reynolds number*
Ta.. $\frac{2\Omega^2 d^4 \eta^2}{(1-\eta^2)\nu^2}$	*Taylor number*
Sc.. $\frac{\nu}{D}$	*Schmidt number*
We.. $\frac{\rho d(\Omega R_1)^2}{\sigma}$	*Weber number*
Ca.. $\frac{\mu \Omega R_1}{\sigma}$	*Capillary number*
Sh.. $\frac{k_c L}{D}$	*Sherwood number*
Nu.. hL/λ	*Nusselt number*
Pr.. $\nu\rho c_p/\lambda$	*Prandtl number*
Γ..	*gamma function*
α.	*volume fraction of slag*
V_ν..	*partial volumetric volume of solute*
χ_D..	correction for influence of Stefan velocity to mass flux

List of subscripts

s..	*interface solute/solvent*
∞..	*at end of the diffusive boundary layer*
1..	dissolving *species*
2..	residual *species*
c..	*convective*
d..	*diffusive*
a..	*air phase*
b..	*slag phase*

simplify the underlying equations using an asymptotic boundary layer method.

The following sections describe the methodology employed in the calculation of mass transfer coefficients and explain the aforementioned phenomena in detail. Subsequently, the asymptotical boundary layer approach is introduced followed by a complete description of the model used for the calculation of the flow field. Lastly, the results are presented and compared to those obtained with the equations discussed above.

2. Methodology of mass transfer calculation

In many application cases, dissolution is controlled by the diffusion of the dissolving species [1,2,4,7]. Under this hypothesis, the dissolution mass flux is given by Fick's First Law of Diffusion, which can be stated as follows for the one-dimensional case:

$$j_D = -D\frac{dc_1}{dy} \tag{1}$$

According to Eq. (1), the diffusive flux depends on the species gradient and the effective binary diffusivity; however, this diffusive flux, when evaluated on the solute/slag interface, does not represent the gross dissolving mass flux. The relative motion between solute and interface constitutes a classical Stefan problem and must also be accounted for, as indicated by Cooper [8,9]. Based on this previous research and approximating the partial volume of a solute as the ratio of the solute to slag densities, the gross flux can be expressed as follows:

$$j_t = j_D\frac{1}{1-w_1} \tag{2}$$

Our next step is the calculation of the diffusive flux. The theory of hydrodynamics of the boundary-layer provides us with a method for this calculation by solving the steady-state convection-diffusion equation for the source-free case:

$$u\frac{\partial c_1}{\partial x} + v\frac{\partial c_1}{\partial y} = D\frac{\partial^2 c_1}{\partial y^2} \tag{3}$$

This equation is solved using the continuity equation, momentum conservation equations, and necessary boundary conditions. Typically, both the tangential and normal velocities are considered to vanish at the wall. Under such circumstances, a perfect analogy between mass and heat transfer holds if the effect of dissipation is neglected. In doing so, the wall is considered to be impermeable to both the diffusing species and all other components (henceforth termed as residual species). This is not the case considered here, which involves the dissolution of the solute from a surface that is impermeable to the other species. This case results in the Eckert-Schneider condition (Eq. (4)), which follows from the equality of the diffusive flux of the dissolving species at the interface ($j_{1,d,s}$) (given by Fick's law) and the convective flow of the residual species ($j_{2,c,s}$). Consequently, a finite velocity in the direction normal to the wall (v_w) must exist, i.e., the analogy between mass and heat transfer does not hold anymore.

$$j_{2,c,s} = \rho(1-w_1)v_w = j_{1,d,s} \tag{4}$$

$$v_w = \frac{j_{1,d,s}}{\rho(1-w_1)} = -\frac{D}{(1-w_1)}\left(\frac{dw_1}{dy}\right)_s \tag{5}$$

Here, the concept of effective binary diffusivity is applied to distinguish between the dissolving species 1 and the residual species 2 using an equal diffusivity D for both. The latter assumption necessitates a constant fluid density, viz. $d\rho/dc = 0$. The velocity v_w is sometimes referred to as Stefan velocity, because he was the first author to experimentally observe such velocities [10].

While the effect of the Stefan velocity on the gross mass flux according to Eq. (2) can be easily considered, its impact on the fluid flow is often neglected; however whether this is justified needs to be proven for each particular case [11].

For dimensionless concentration $c_1{}^* = c_1/\Delta c$ and coordinate $y^* = y/L$, the mass flux at the interface can be represented in terms of the Sherwood number:

$$Sh = \frac{j_D L}{D\Delta c} = -\left(\frac{\partial c_1{}^*}{\partial y^*}\right)_s \tag{6}$$

The Stefan velocity contributes with a mass flux $v_w c_1$, accounted for in Eq. (2), but its effect on the flow field might be better understood in terms of the diffusive boundary layer thickness (δ_c), sometimes referred to as Nernst boundary layer thickness, using the following definition:

$$j_D = -D\frac{\Delta c}{\delta_c} \tag{7}$$

It follows from Eq. (1) that this thickness is a function of the concentration gradient at the interface according to Eq. (8):

$$\delta_c = \frac{\Delta c}{\left|\frac{dc_i}{dy}\right|} \tag{8}$$

The ratio of the thickness of the velocity to species boundary layers is concordantly dependent on the dimensionless Schmidt number, and the Stefan velocity increases both thicknesses for the case of dissolution (it acts inversely for the crystallization case); consequently, the effect of the Stefan velocity results in a reduction in the mass transfer coefficients of dissolution, or equivalently, a decrease in the absolute value of the derivative at the right-hand-side of Eq. (6). Sherwood relations neglecting the effect of Stefan flow or corresponding Nusselt equations are well known for many cases, and the respective Sherwood number is denominated by Sh_0 here.

Calculating Sh amounts to solving Eq. (3) including v_w as a boundary condition, and it is analogous to a boundary layer control by blowing; it has been studied by Merk [12]. Merk provides formulas for χ_D, the ratio of Sh to Sh_0 as a function of B; consequently, we only need to concentrate ourselves on the calculation of Sh_0 to express the total flux as follows:

$$j_t = \chi_D \frac{DSh_0}{L} B\rho \tag{9}$$

which can be reformulated to $j_t = k_c \Delta c$, where the mass transfer coefficient (k_c) is given by

$$k_c = \frac{\chi_D}{1 - w_s}\frac{DSh_0}{L} \tag{10}$$

It is important to notice that even though v_w can have an effect on the mass transfer rate, it does not influence the velocity field outside of the boundary layer [13] but extends it compared to the case with $v_w = 0$. In this work, calculations of Sh_0 are conducted by coupling CFD simulations with an asymptotic boundary layer approach, in what it is known as asymptotical computational fluid dynamics (ACFD).

3. Experimental set-up

In this work simulations of a typical experimental set-up used in ceramic and refractory testing, namely the rotating finger test, are performed. This set-up is employed purely as a basis for the simulations. In this experiment, a cylindrical sample of refractory material is rotated while submerged into a slag bath at a constant rotational speed of 200 rpm under isothermal conditions. The sample of pure dense sapphire fine ceramics has an initial radius of 10 mm and a total length of 110 mm. Approximately 55 mm are dipped in the slag bath contained in a crucible of 32.5 mm of radius with a clearance to the bottom of the crucible of 20 mm. The CAS slag (viz. a silicate slag in the system CaO-Al_2O_3-SiO_2) is maintained at 1550 °C, and the initial concentration and its properties are summarized in Table 1. Density and surface tension values were calculated at service temperature using the correlations proposed by Xin [14,15] based on the bulk concentration. The alumina solubility is 48.79% in weight.

Table 1
Slag/refractory properties.

	CaO	Al_2O_3	SiO_2	D (m^2s^{-1})	μ (Pa s)	ρ (kg/m^3)	σ (mNm^{-1})
w	0.3807	0.2100	0.4093	$4.2\cdot10^{11}$	0.6423	2,589	476.9

Table 2
Dimensionless numbers.

Re	*Ta*	*Sc*	*We*	*Ca*
19	382	$5.9\cdot10^6$	5.4	0.28

From these values, the most relevant dimensionless numbers for the problem were calculated and are presented in Table 2. The peripheral velocity at the inner cylinder was chosen as the characteristic velocity, which is the upper bound of the velocities, and it is therefore the most conservative choice. For the Schmidt number, the diffusivity value is selected from the diffusivities presented in the work of Cooper and Kingery [1]. The characteristic length is the gap width in all cases.

4. Hydrodynamics of large Schmidt numbers

Given the high values of Schmidt number of the system (above 10^6, see also Table 2), resolution of the species boundary layer would require a very fine mesh in the region of the solute/slag interface. To overcome this issue, an asymptotic boundary layer approach is employed; however, the species transport equation is not solved within the CFD calculation.

A connection between the skin friction (τ) and heat transfer rate was elucidated by Lighthill [16] through a von Mises transformation of the energy equation:

$$Nu(x) = \frac{L\ Pr^{1/3}}{9^{1/3}\Gamma(4/3)}\left(\frac{\rho}{\mu^2}\right)^{1/3}\sqrt{\tau(x)}\left(\int_0^x \sqrt{\tau(\zeta)}d\zeta\right)^{-1/3} \tag{11}$$

This approximation considers a linear velocity profile in the boundary layer given by $u = (\tau/\mu)\cdot y$, which becomes asymptotically exact for large Pr (Sc) [17].

This work was extended by Acrivos in two publications [18,19], in which he derived a more general solution for the heat (species) transfer rate by considering wedge-flow velocity profiles ($u = ay^m$) in the boundary layer. He arrived at a theoretical solution for arbitrary exponent m, which reduces to the to Lighthill's method for $m = 1$. The methodology is grounded on the principle that when the Pr (Sc) number is large the thermal (concentration) boundary layer is much thinner than the velocity boundary layer. Acrivos also studied the asymptotic case of very small Pr (Sc) number as well as the effect of variable fluid properties.

It is noteworthy that the method proposed by Lighthill is not well suited near points of flow separation, where τ becomes zero and a linear velocity profile no longer approximates this situation. A detailed analysis of the effect of this nonlinearity on the heat transfer rate is presented by Spalding [17], who proposed a correction to Lighthill's method.

The case treated within this work is a case of axisymmetric flow, for which Eq. (11) requires some adaptation. This was conducted already by Newman [20] and employed for the calculation of the limiting electrical current of an electrode (for which

$c_{1,s} = 0$). The equation is adapted here by converting the transport of electrical charge induced by the diffusing species to the pure mass transport, which results in Eq. (12):

$$Sh_0(x) = \frac{L\ Sc^{1/3}}{9^{1/3}\ \nu^{1/3}\Gamma(4/3)}\sqrt{\mathcal{R}\ \beta(x)}\left[\int_0^x \mathcal{R}\ \sqrt{\mathcal{R}\ \beta(\zeta)}d\zeta\right]^{-1/3} \quad (12)$$

where $\mathcal{R}$ is the radius of the surface of revolution and $\beta = \frac{\partial u}{\partial y}$. For the cylindrical geometry in this work, when applying Eq. (12) to the cylinder mantle, $\mathcal{R}$ is constant and equal to the cylinder radius and x is the z coordinate. In this case, the equation reduces to Eq. (11). On the disk surface, $\mathcal{R}$ is variable and equal to the radial coordinate x. The azimuthal component of the velocity flow field does not contribute to mass transfer in the laminar regime [20]; consequently, the focus is on the determination of axial and—for the end face—radial stresses at the sample surface.

Existing publications have reported the use of this methodology for the determination of species mass flux [21,22] and have successfully contrasted their findings to experimental results. Particularly, Baier et al. [22] used this method for a Taylor-Couette (TC) system. In this previous study, no special consideration was given to the point of separation; nevertheless, their results agreed with experimental results. Therefore, we also neglect the nonlinearity close to separation points.

The use of Eq. (12) under the influence of a Stefan flow is justified, as has been demonstrated by Schlichting and Gersten [13] that the similarity of solutions of wedge-flow velocity profiles still holds when the Eckert-Schneider condition (Eq. (4)) is fulfilled, and the constant concentration of the dissolving species is fixed at the wall. Moreover, according to Acrivos [23], a relation similar to Eq. (12) can be derived (13), which also considers the effect of the Stefan velocity only by replacing $1/\Gamma(4/3)$ by a quantity b, which is implicitly defined by the following equation:

$$\frac{1}{b} = \int_0^\infty e^{Bbx-x^3}dx \quad (13)$$

This modification to Eq. (12) can also be expressed by multiplication with χ_D defined by

$$\chi_D = \frac{\Gamma(4/3)}{\int_0^\infty e^{Bbx-x^3}dx} \quad (14)$$

which produces very similar results to the correlations proposed by Merk [12] with a relative error of 1.5% for the value of B resulting from the experimental set-up as investigated here.

5. Flow field

The flow domain can be separated into two distinct regions, i.e., the annular region between the cylinder mantle and the crucible and the area below the tip of the sample. In the latter, the disk-shaped surface acts as a centrifugal pump that pulls fluid outwards. Fluid continuity requires that an axial flow develops, which replenishes this displaced fluid.

The flow field induced by a rotating cylindrical surface has been extensively studied by many authors, and it is a characteristic topic in hydrodynamics [13,20,24–26]. Most studies have investigated an ideal case of a disk of infinite diameter in a semi-infinite domain for which the flow is a characteristic boundary layer flow, where the thickness of the boundary layer can be calculated using the equation found in [13]:

$$\delta = 5.5\sqrt{\frac{\nu}{\Omega}} \quad (15)$$

For the system considered here, this thickness is comparable to the bottom clearance, and it is even larger than the radius of the disk. Consequently, the ideal case approximation is not valid. Nonetheless, this benchmark problem is used for comparison and analysis of the characteristics of the flow field, which according to Newman and Thomas [20], remains in the laminar regime for Reynolds numbers up to $2{\cdot}10^5$.

The annular region, with the inner cylinder rotating at a constant rotational speed, is a region where a Circular Couette (CC) flow forms. It is a very well-known fact that a pure CC flow cannot be maintained for any rotational speed. Upon a critical speed, centrifugal instabilities settle in form of vortical structures. Many authors have addressed the topic of instabilities in the CC system. Taylor [27] was one of the first authors to investigate this by means of a mathematical approach. His-work, based on linear perturbation analysis, predicts the rotational speed necessary for these instabilities to set-in by considering an idealized case of narrow gap and infinite length cylinders. Numerous publications proceeded the work of Taylor and since then, the influence of different parameters on the stability of the CC flow has been investigated [28–44].

A variety of flow regimes can take place within a TC system depending on geometrical aspects and the rotational speed. A good classification and description of each regime can be found in Gollub [45]. Numerical investigations on the transitions between this regimens is conducted for e.g. in the work of Takeda [46]. For the system dealt within this work, the flow is in the laminar regime and the instabilities do not exceed the Taylor Vortex Flow (TVF) regime, where stacked, time-independent, axisymmetric vortices form. This validates our hypothesis of 2D, laminar, axisymmetric flow used in developing the CFD model.

Because of the wide gap of the arrangement, the analysis conducted by Taylor is not applicable here. DiPrima et al. [42] calculated the critical rotational speed for different radii ratios. From their results, we obtain for the chosen experimental set-up a critical rotational speed for our system of 740 rpm with an axial wavelength of 44.7 mm. This axial wavelength represents the length of two consecutive vortices, and given that our gap width is 22 mm, the vortices should appear square, as is typical in TC systems. When comparing the wavelength with the dipped length, we observe that the infinite length is far from a good approximation; moreover, the critical rotational speed for the experimental set-up is well above 200 rpm, even though vortical structures are observed in the simulations of the experimental set-up, which must then be attributed to end-effects. For comparison, simulations at higher Reynolds number were conducted within the TC regime as well, and, here, Taylor vortices were observed.

It has been observed that end-effects have a significant influence on the stability even in cases where the cylinders are very large [47]. Various authors have studied the influence of end-effects on the TC system [39,48–57]. When the cylinders are of finite length, the end-conditions imposed result in a region where the flow field is no longer geostrophic, i.e., the centrifugal force is not balanced by the pressure gradient, which results in development of radial velocity.

Generally, three different boundary conditions are considered for the end-effects: static end plates, rotating plates, and free surfaces. The characteristics of these flows can be explained by a family of boundary layer flows known as the BEK family (Bödewadt, Ekman, von Kármán). Bödewadt [58] studied the flow field of a rotating fluid close to static wall, which represents the case of a static plate, while von Kármán [24] studied the rotating disk described previously. Finally, Ekman developed a theory on the effect of wind on ocean currents considering the effect of the Coriolis force [59]. In the literature, the vortices induced by end-effects are generally referred to as Ekman vortices and are said to be caused by Ekman pumping.

Given that both the annular and clearance regions, when compared to close analytical situations, are well within the laminar region, no turbulence is considered in the CFD model.

6. Model description

The CFD model is implemented in the software Ansys Fluent, v. 19.0. The laminar, 2D, axisymmetric model is a multiphase model of the slag and air phases. The boundary conditions are summarized in Fig. 1 and include a pressure outlet at the top of the domain, where the air is located, a no-slip condition on the crucible wall, constant angular speed on the refractory wall and an axis of symmetry along the axis of the rotating sample. The species transport equation is not solved within the CFD model; this is treated in a postprocessing step as described in Section 4. Additionally, the model is isothermal; thus, only the continuity equation Eq. (16) and Navier-Stokes equations (Eqs. (17) to (19)) are solved within the CFD model:

$$\frac{\partial}{\partial z}(\rho v_z)+\frac{\partial}{\partial r}(\rho v_r)+\frac{\rho v_r}{r}=0 \tag{16}$$

$$\frac{\partial}{\partial t}(\rho v_z)+\frac{1}{r}\frac{\partial}{\partial z}(r\rho v_z v_z)+\frac{1}{r}\frac{\partial}{\partial r}(r\rho v_z v_r) = -\frac{\partial p}{\partial z}+\frac{1}{r}\frac{\partial}{\partial z}\left[r\mu\left(2\frac{\partial v_z}{\partial z}-\frac{2}{3}\nabla\cdot\vec{v}\right)\right]+\frac{1}{r}\frac{\partial}{\partial r}\left[r\mu\left(\frac{\partial v_z}{\partial r}+\frac{\partial v_r}{\partial z}\right)\right] \tag{17}$$

$$\frac{\partial}{\partial t}(\rho v_r)+\frac{1}{r}\frac{\partial}{\partial z}(r\rho v_r v_z)+\frac{1}{r}\frac{\partial}{\partial r}(r\rho v_r v_r) = -\frac{\partial p}{\partial r}+\frac{1}{r}\frac{\partial}{\partial z}\left[r\mu\left(\frac{\partial v_r}{\partial z}+\frac{\partial v_z}{\partial r}\right)\right]+\frac{1}{r}\frac{\partial}{\partial r}\left[r\mu\left(2\frac{\partial v_r}{\partial r}-\frac{2}{3}\nabla\cdot\vec{v}\right)\right] -2\mu\frac{v_r}{r^2}+\frac{2}{3}\frac{\mu}{r}(\nabla\cdot\vec{v})+\rho\frac{v_\theta^2}{r} \tag{18}$$

$$\frac{\partial}{\partial t}(\rho v_\theta)+\frac{1}{r}\frac{\partial}{\partial z}(r\rho v_z v_\theta)+\frac{1}{r}\frac{\partial}{\partial r}(r\rho v_r v_\theta) = \frac{1}{r}\frac{\partial}{\partial z}\left[r\mu\left(\frac{\partial v_\theta}{\partial z}\right)\right]+\frac{1}{r^2}\frac{\partial}{\partial r}\left[r^3\mu\frac{\partial}{\partial r}\left(\frac{v_\theta}{r}\right)\right]-\rho\frac{v_r v_\theta}{r} \tag{19}$$

where $\nabla\cdot\vec{v}$ is given by Eq. (20):

$$\nabla\cdot\vec{v}=\frac{\partial v_z}{\partial z}+\frac{\partial v_r}{\partial r}+\frac{v_r}{r} \tag{20}$$

The volume of fluid (VOF) method was chosen to incorporate both slag and air phases. This is an interface-capturing-method for which the transport equation of a scalar function representing the volume fraction of a phase (α), is solved Eq. (23). A single set of equations is solved for the flow field, where the density and viscosity are dependent on α as shown in Eqs. (21) and (22). A sharp jump in these properties occurs at the interface between phases, which is only a few cells wide:

$$\mu=\mu_a\alpha+(1-\alpha)\mu_a \tag{21}$$

$$\rho=\rho_b\alpha+(1-\alpha)\rho_b \tag{22}$$

$$\frac{\partial\alpha}{\partial t}+\nabla\cdot(\alpha\vec{v})=0 \tag{23}$$

For the advection of the interface between phases, the Geometric-Reconstruct scheme is employed, which is the most accurate method available [60]. This scheme is explicit in time, and the time-step used for solving Eq. (23) is automatically chosen by the solver based on a maximum Courant number of 0.25, which is independent of the time-step used for solving other transport equations.

Surface tension is considered in the simulations given the low values of Capillarity and Weber number of the system as presented in Table 2. Its effect is studied using the continuous surface force (CSF) model formulated by Brackbill [61]. The surface tension force is considered constant along the interface using the value presented in Table 1. Marangoni convection is neglected as it has been reported to have no effect when the rotational speed is large enough [62], which has been corroborated by Kircher for a similar set-up [63]. Buoyancy effects induced by density gradients are also neglected.

Coupling between pressure and velocity is accomplished with the PISO scheme and second order schemes are used for the momentum and swirl equations. The pressure is interpolated from the cell centroid to cell faces using with the PRESTO! scheme. A grid-independence-test was conducted for three different element sizes based on the value of the derivative of axial velocity at the slag/refractory interface. The results are presented in Section 7. Two different time-steps of 0.001 s and 0.0001 s were employed in the simulations, and no differences in the results were observed.

The VOF was patched to the dipped length and the solution was advanced from an initial static state. A steady state is considered to be achieved when no more time variations in $\beta(x)$ are observed. Time discretization is done with an implicit first-order scheme, because higher-order schemes are not available with an explicit treatment of the VOF equation.

Simulations are conducted for the cylindrical geometry and the mesh is composed entirely of quadrilateral elements of equal size, as shown in Fig. 1.

The total number of discretization elements varies from the coarsest to the finest grid between approximately 47,000 to 190,000 elements.

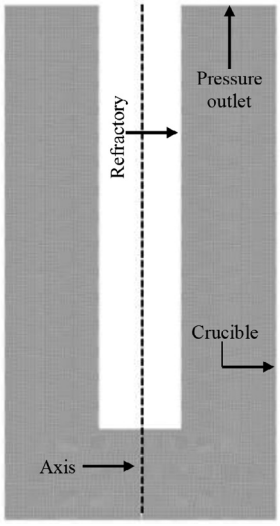

Fig. 1. Discretization of the domain.

7. Results and discussion

The following shows the results of the simulations of the experimental set-up presented in Section 3, where the Reynolds number are was 19 and 8.4 based on the gap width and inner radius, respectively (see also Table 2). The flow field is depicted in Fig. 2 with path-lines colored by the phase volume fraction; the employed boundary conditions are also illustrated. We observe an axial flow along the cylinder mantle induced by the rotation of the end face, along which a radial flow occurs. This agrees with the theoretical discussion presented in Section 5. Moreover, in this region, the flow-field matches qualitatively the results presented by Levich [25] for a rotating disk. One main difference is that, in the infinite disk case, the flow domain is limited by the disk itself; however, here, the developed axial flow ascends the cylin-

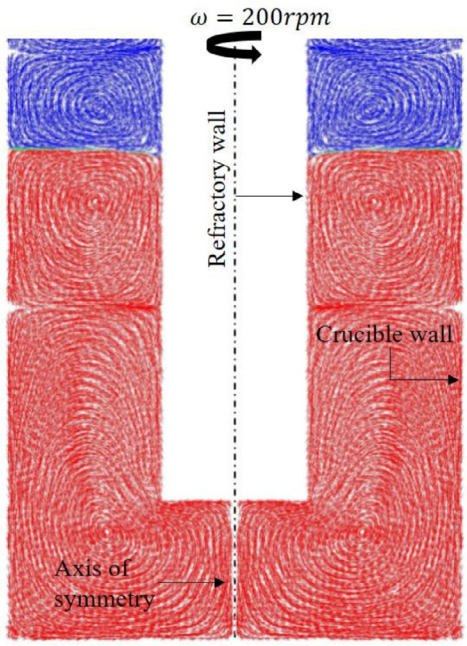

Fig. 2. Flow field path-lines. Slag phase in red, air phase in blue.

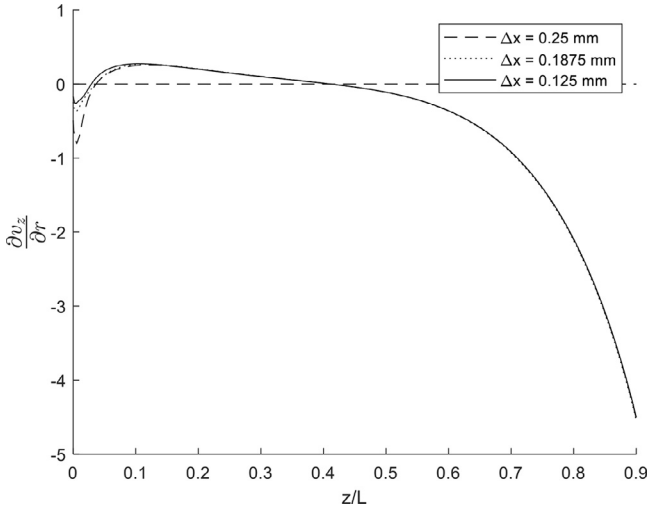

Fig. 3. Derivative of axial velocity with respect to radial coordinate over cylinder mantle (L = submerged length).

der mantle. Within the slag bath and close to the interface atmosphere/slag, we observe a vortical structure that is attributed to Ekman transport. Its quadratic shape is very close to the predicted wavelength of a TC instability and the rotation is in the opposite direction as in the lower region of the sample, which results in an inflection point where the vortical structures meet. This can also be perceived from Fig. 3; at this position, β becomes zero. In this figure, the independence of the axial and radial derivatives of velocity from grid fineness can also be observed. This independence is also proven for the derivative of the radial velocity over the refractory tip shown in Fig. 4.

The profiles of Sh_0 relative to the Schmidt number to the power of one third, calculated as described in the previous section, are shown in a dimensionless form in Fig. 5 for the disk surface and in Fig. 6 for the cylinder mantle. The independence of the grid fineness is also depicted for the aforementioned calculations. A good qualitative match is observed in this figure, with an error in the

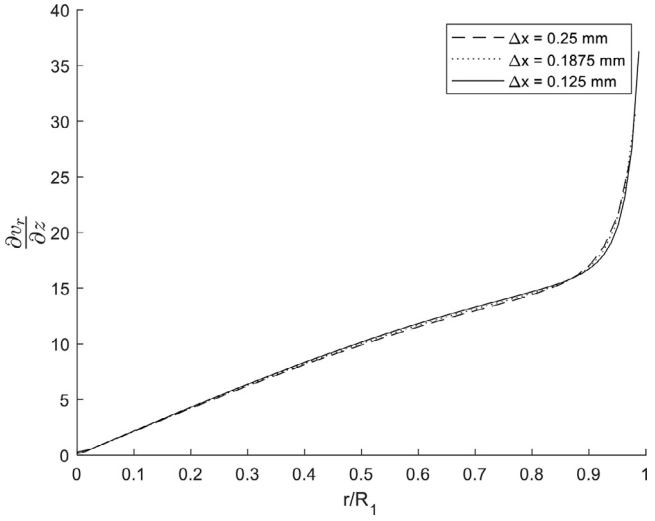

Fig. 4. Derivative of radial velocity with respect to axial coordinate over cylinder tip.

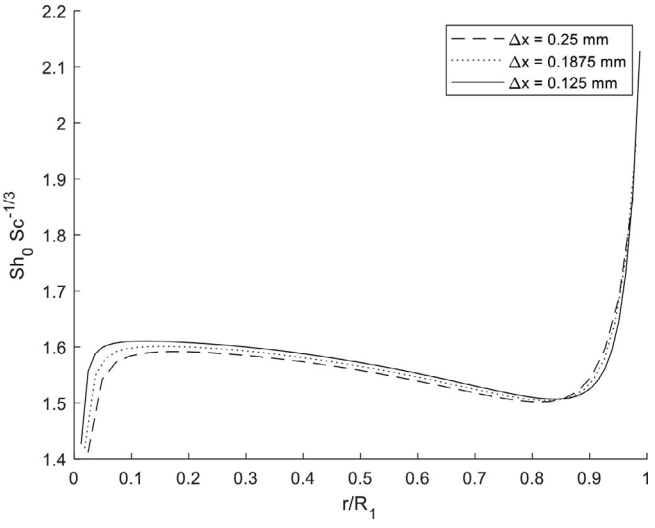

Fig. 5. Sherwood profile relative to $Sc^{-1/3}$ for the disk surface.

average value of 2%; therefore, the results are considered to be independent of the grid fineness.

The values presented in Figs. 5 and 6 are those necessary for calculating the mass transfer coefficients using Eq. (10), which are displayed in Fig. 7 for the cylinder mantle. In these figures, the relationship between the flow field and Sherwood profiles is noticeable. For the cylinder mantle, we observe a marked increase in Sh_0 towards the end of the cylinder, which is attributed to the higher axial stresses present in this region. These stresses become smaller further away from this region and consequently Sh_0 decreases. The profile presents a minimum at the location where the two vortical structures meet and another one near the slag/atmosphere interface, where β changes sign.

Simulations for a range of Reynolds numbers based on the inner radius between 1 and 500 were also conducted to gain better insight into this set-up and facilitate verification with documented Sherwood equations in Section 7.1. The rotational speed was maintained in all cases at 200 rpm. To obtain different Reynolds number the simulations were conducted by varying the value of dynamic viscosity, resulting in an alteration of the value of the predicted theoretical critical rotational speed; however, the critical Reynolds number calculated for the geometry remains unchanged

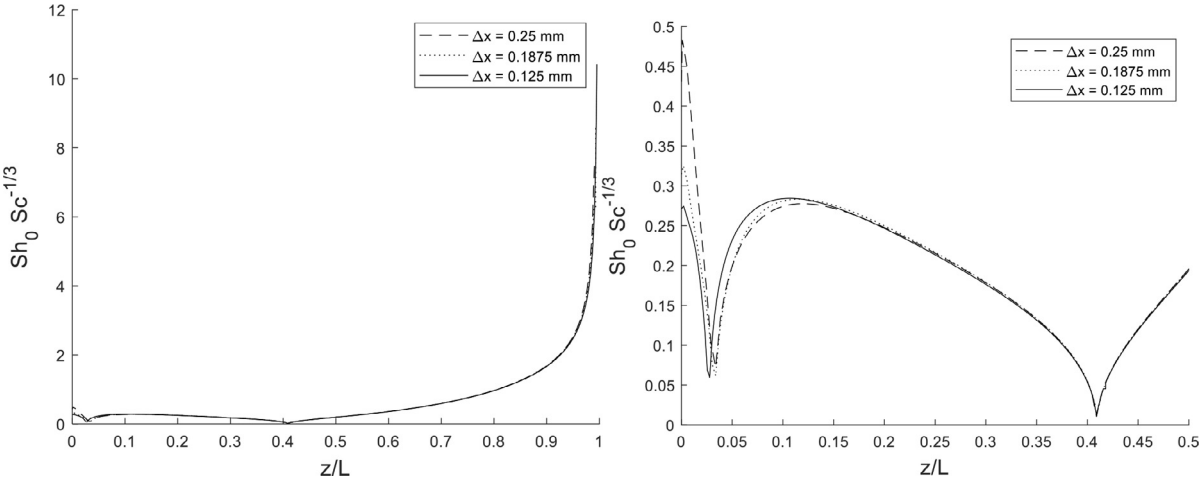

Fig. 6. Sherwood profile relative to $Sc^{-1/3}$ on the cylinder mantle (left) and magnification of the part z/L<0.5 (right), where L is submerged length.

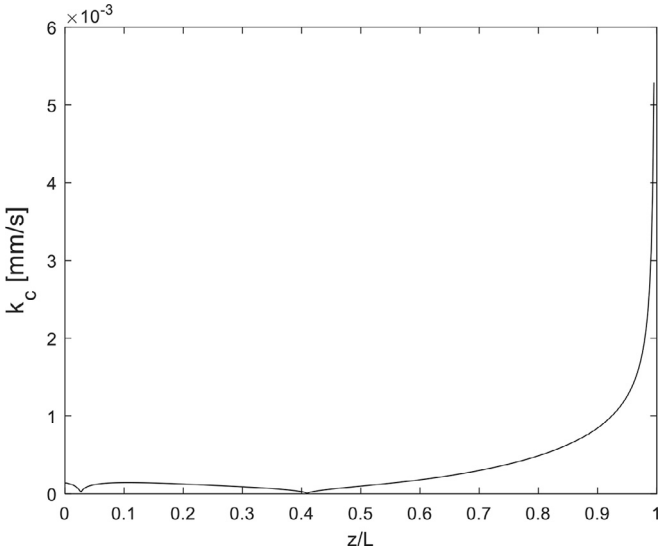

Fig. 7. Mass transfer coefficients profile on the cylinder mantle.

at $Re_{R_1} = 31.8$. This value was calculated by a simple correlation of the data presented in the publication of DiPrima et al. [42], presented below:

$$Re_{R_{1,c}} = \sqrt{\frac{800.5(1+\eta)}{\eta^{1.005}(1-\eta)}}\frac{R_1}{d} \tag{24}$$

The flow field for these calculated values is depicted in Fig. 8 with path-lines colored by contours of velocity magnitude. For small Reynolds numbers, below the critical rotational speed, the velocity magnitude in the annular region is dominated by the azimuthal component, which is described by the analytical CC solution. In this case, the velocity decreases from the imposed rotating velocity at the inner cylinder to zero at the static outer cylinder. It is also noticeable that this CC variation in the velocity only occurs in the annular region and deviates towards the end of the sample, as expected. For $Re_{R_1} = 30$, which is very close to the critical rotational speed, the magnitudes of the axial and radial velocities are already large enough to have an obvious influence on the total velocity magnitude. Beyond this value, the appearance of a second vortex can be observed, which is then attributed to centrifugal instabilities. The velocity magnitude for this range of Reynolds numbers is no longer given by a pure CC flow and the axial and radial velocity of the vortices is comparable to the azimuthal velocity. The critical Reynolds number, although derived for the case of infinite length cylinders, provides a reasonable estimate of the bifurcation point; this is because, below this value, we only observe Ekman vortices, which increase in size and strength with Reynolds number. The proximity of the observed critical point to the theoretical prediction provides validation to our computed flow-field and the hypothesis employed in the construction of the model.

The Sherwood profile relative to the Schmidt number to the power of one third for $Re_{R_1} = 200$ is shown in Fig. 9 for the mantle. In this Figure we observe two minima due to the appearance of a second vortex. Unlike for low Reynold numbers, for which the appearing vortex was attributed to end-effects, these Taylor vortices are a result of centrifugal instabilities and have larger radial and axial velocities. Therefore, the observed Sh_0 in these regions is noticeably larger and comparable to the Sh_0 value observed towards the end of the cylinder. In average, Sh_0 follows the expected increment with the Reynolds number, and a change in the slope of the logarithmic plot of Sh_0 versus Re is observed at the transition from the CC regime to the TC, which is presented in Fig. 11 of Section 7.1.

7.1. Comparison to documented mass transfer equations

By distinguishing between the bottom clearance and the annular region, the total average mass flux density could be approximated by independently employing correlations for the disk surface and a cylindrical surface. We now compare the approach used in this work with equations that have been reported in the literature. For the disk surface, the theoretical Eq. (25) proposed by Levich was found to be optimal [25].

$$Sh = 0.62 \cdot Re^{1/2}Sc^{1/3} \tag{25}$$

This equation was also used for verification of the mass transfer calculations. This verification was performed at higher rotational speeds, because in this case, the boundary layer thickness decreases according to Eq. (15), and we approach the ideal situation corresponding to this equation. The results are shown in Fig. 10, where an excellent agreement with Levich's equation is observed for rotational speeds higher than 750 rpm, whereas for the rotational speed used in this work, an error of 16% is incurred.

The determination of heat/mass transfer in a CC system has been investigated by some authors [5,22,64–69]; however not all authors present correlations with parameters of interest. From these works, the correlations presented by Tachibana et al. [5] and Srinivasan et al. [69] were selected, and the values are compared in Fig. 11 for the Schmidt number given in Table 2 and Reynolds

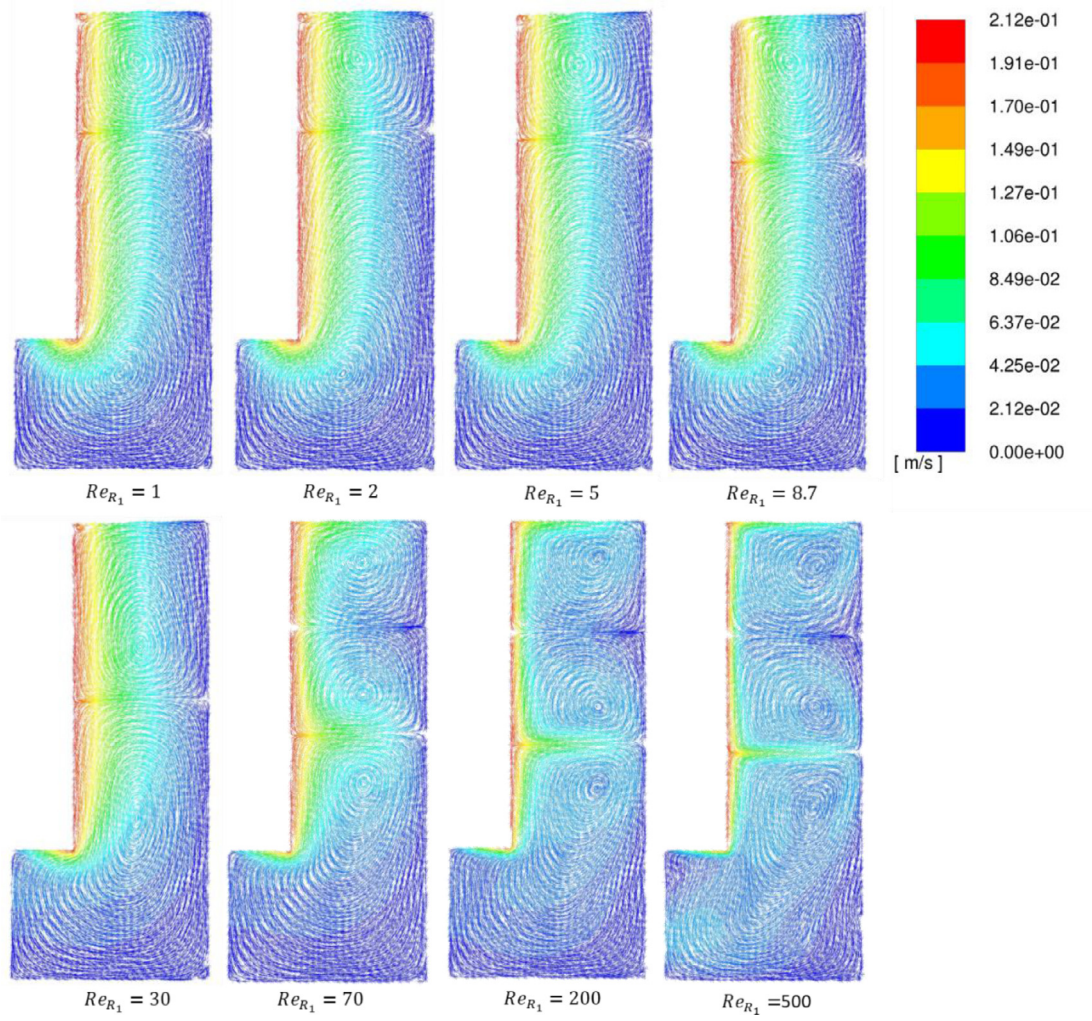

Fig. 8. Path-lines colored by velocity magnitude at different Reynold numbers.

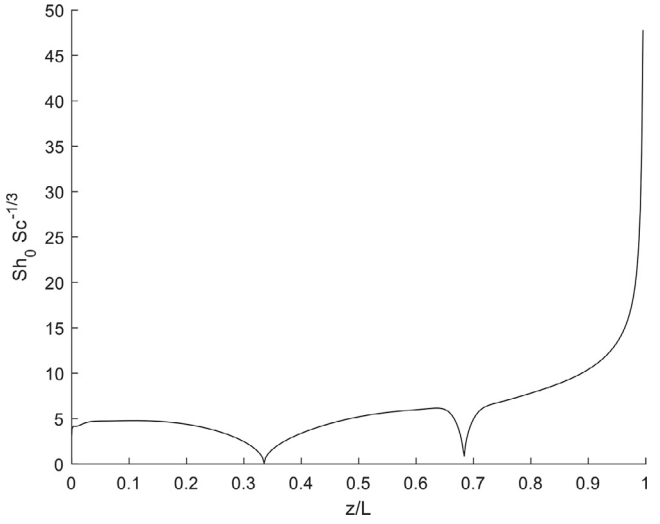

Fig. 9. Sherwood profile relative to $Sc^{-1/3}$ on the cylinder mantle for $Re_{R_1} = 200$.

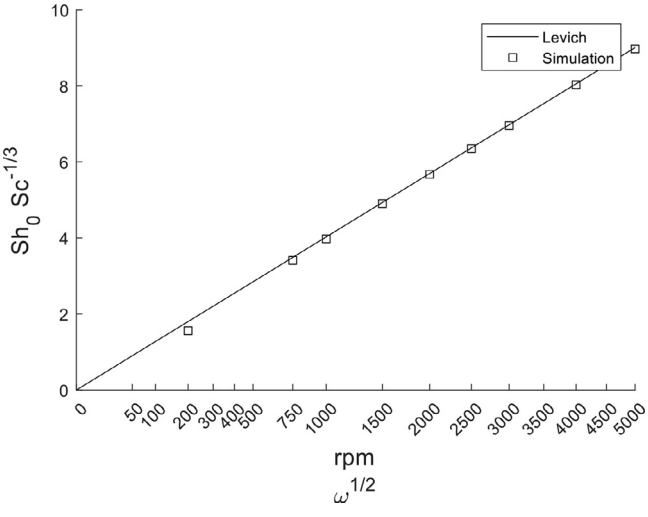

Fig. 10. Comparison of asymptotic calculations to Levich's equation.

number in the range of 1–500. Experimental equations based on a rotating cylinder by Kosaka and Minowa [70] and Eisenberg et al. [6] are also displayed in this figure. All these equations are presented in Table 3 referenced to by the name of the first author and the subscripts indicate the characteristic length used in calculating Sherwood and Reynolds number (viz. the gap width was used as characteristic dimension of the Sherwood numbers for the cylinder mantle); furthermore, the validity ranges displayed in Table 3 are

Table 3
Equations for the calculation of mass transfer coefficients.

	Equation	Application/Validity range
Levich [25]	$Sh_{R_1} = 0.62 \cdot Re_{R_1}^{1/2} Sc^{1/3}$	disk/ Re<100,000 100 <Sc ([20])
Eisenberg [6]	$Sh_d = 0.0642 Re_{R_1}^{0.7} Sc^{0.356} \frac{d}{R_1}$	Mantle/ 500<Re<50,000 835<Sc<11,490
Kosaka [4]	$Sh_d = 0.0547 Re_{R_1}^{0.75} Sc^{1/3} \frac{d}{R_1}$	Mantle/ 50<Re<5,000 106<Sc<173
Tachibana [5]	$Sh_d = 0.21 Re_{R_1}^{1/2} Sc^{1/4} (\frac{d}{R_1})^{3/4}$	Mantle/ Re<$10^4 (\frac{R_1}{d})^{0.5}$
Srinivasan [69]	$Ta < Ta_c$ $Sh_d = \frac{3d}{R_1 \log(R_2/R_1)} + 0.0048 Re_{R_1} Sc^{1/3} \frac{d}{R_1} (\frac{R_1}{R_2})^{-1.25}$	Mantle/ 0.5<Re<1,000 1<Sc<50,000 0.3 < R_1/R_2 < 0.7
	$Ta > Ta_c$ $Sh_d = \frac{3d}{R_1 \log(R_2/R_1)} + 0.3253 Re_{R_1}^{0.5} Sc^{1/3} (\frac{d}{R_1})^{0.5} (\frac{R_1}{R_2})^{-0.1}$	

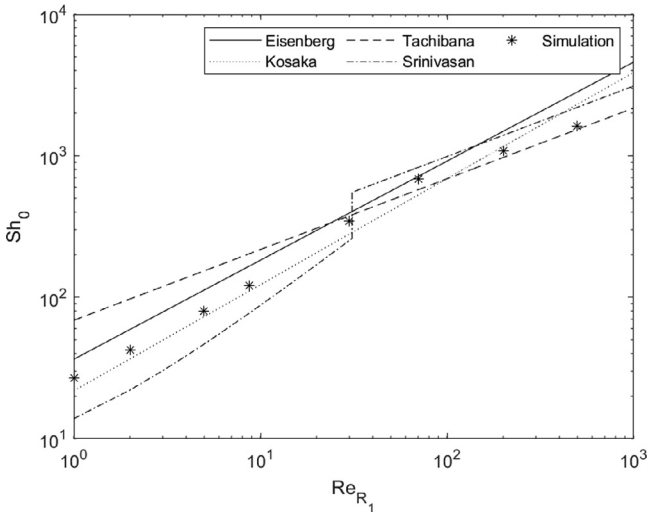

Fig. 11. Comparison of Sh values for cylinder mantle (for Tachibana the exponent of *Sc* was replaced by 1/3, see text).

either reported by the authors themselves or based on the experimental data presented in the respective publications and/or theoretical justifications.

It can be observed from Fig. 11 that the equation of Kosaka and Eisenberg has a similar slope to the simulation results. For Reynolds numbers below 30, our results match very well with the equation of Kosaka and Minowa, with the largest calculated relative error being 18% at $Re = 1$ and decreasing with this number. For the experimental set-up value, Kosaka and Minowa equation underpredicts the value of Sherwood number by 9%. Over the critical Reynolds number ($Re_{R_1} = 31.8$ for our system, see text below), the deviation of the calculated values from Eisenberg's equation becomes larger. For Reynolds numbers greater than the critical Reynolds number, the equation of Srinivasan has a similar slope to the trend followed by the simulated value. This is not true for smaller Reynolds, presumably due to the differences in cylinder length and boundary conditions, which play a marked role in this regime. The formula of Tachibana, presented in Table 3 has a dependency on Schmidt number of $Sc^{1/4}$, however, given that this correlation was obtained for fluids of much smaller Prandtl number as the equivalent Schmidt values considered in this publication, the comparison shown in Fig. 11 was done by replacing this factor with $Sc^{1/3}$, which is the expected dependency for large Schmidt numbers [11]. In this case, the slope of the equation is also similar to the equation of Srinivasan and matches the simulated values very well; however, when the original $Sc^{1/4}$ dependency is used, the values predicted by Tachibana equation are much smaller than the simulated values. Both Srinivasan and Tachibana's equations are based on pure TC flow where the length of the cylinder has no effect on the mass transfer rate; this is not true for our set-up composed of a very short cylinder where a bottom clearance is present as well. For these reasons, we expect some deviation between the simulated values and the documented equations; however, for the modified Tachibana equation with exponent 1/3 of *Sc* number, over the critical rotational speed, the maximum error was surprisingly only 16% and decreased with increasing Reynolds number. The modified equation only provides a good qualitative fit for Reynolds above the critical condition, as expected, because it was developed for flow in this regime. A detailed parameter study is not in the scope of this publication but the reasonable agreement between the documented equations and the simulated values in the respective ranges validates the use of the approach for such set-ups.

The correction due to the influence of Stefan velocity on the flow field calculated with Merk's method is, for the experimental case considered here, $\chi_D = 0.765$, indicating that a large error is committed by neglecting the effect of the Stefan velocity on the Sherwood calculations.

8. Conclusions

An asymptotic boundary layer approach was employed to calculate mass transfer coefficients from CFD simulations of a rotating finger test. This approach reduces the amount of computation resources needed and provides accurate results. Independence of both grid fineness and time-step was obtained in all calculations. The methodology was verified by comparing Levich's equation at higher rotational speeds. The obtained values were compared with the results of documented equations for the calculation of mass transfer coefficients. While reasonable agreement was obtained with some of the empirical equations for selected Reynolds numbers, most of the empirical equations have not been designed for the experimental set-up investigated here and for such high Schmidt numbers. This underlines the necessity of the approach shown here. The methodology presented provides an accurate tool

for predicting mass transfer coefficients in dissolution problems when the binary diffusivity is known or alternatively it presents an opportunity to inversely determine diffusivities. This methodology is a very important tool for systems where the Schmidt number (or alternatively Prandtl number) reaches very large values, and computational resources pose a problem. Such systems are frequent in slag/refractory systems, such as the one discussed in this work, and electrolytic solutions. The expected greater accuracy of the method originates from the fact that a more rigorous consideration regarding the phenomena involved in the dissolution was considered, and all the appearing effects were incorporated to the methodology. Furthermore, because the boundary layer approach becomes asymptotically exact for large Schmidt numbers, and already some successful studies employing this method are found in literature for smaller numbers, we expect that for typical ceramic/slag systems this should also be the case. Nevertheless, validation of the model through experiments is in the future works of the authors. In addition to the evaluation of tests as described herein, the methodology also offers a mathematical procedure to optimize reactor design or process parameters with respect to mass transfer, e.g. to minimize the wear of a refractory lining.

Declaration of Competing Interest

The authors declare that they have no known competing financial interests or personal relationships that could have appeared to influence the work reported in this paper.

Acknowledgments

The authors gratefully acknowledge the financial support under the scope of the COMET program within the K2 Center “Integrated Computational Material, Process and Product Engineering (IC-MPPE)” (Project No. 859480). This program is supported by the Austrian Federal Ministries for Climate Action, Environment, Energy, Mobility, Innovation and Technology (BMK) and for Digital and Economic Affairs (BMDW), represented by the Austrian research funding association (FFG), and the federal states of Styria, Upper Austria, and Tyrol.

References

[1] A.R. C.ooper, W.D. K.ingery, Dissolution in ceramic systems: I, molecular diffusion, natural convection, and forced convection studies of sapphire dissolution in calcium aluminum silicate, J. Am. Ceram. Soc. 47 (1) (Jan. 1964) 37–43.
[2] S. Jansson, V. Brabie, P. Jonsson, Corrosion mechanism and kinetic behaviour of MgO-C refractory material in contact with CaO-Al2O3-SiO2-MgO slag, Scand. J. Metall. 34 (5) (Oct. 2005) 283–292.
[3] I. Kasimagwa, V. Brabie, P.G. J.önsson, Slag corrosion of MgO–C refractories during secondary steel refining, Ironmak. Steelmak. 41 (2) (Feb. 2014) 121–131.
[4] M. Kosaka, S. Minowa, On the rate of dissolution of carbon into molten Fe-C alloy, Trans. Iron Steel Inst. Japan 8 (6) (1968) 392–400.
[5] F. Tachibana, S. Fukui, H. Mitsumura, Heat transfer in an annulus with an inner rotating cylinder, Trans. Japan Soc. Mech. Eng. 25 (156) (1959) 788–792.
[6] M. Eisenberg, C.W. T.obias, C.R. W.ilke, Ionic mass transfer and concentration polarization at rotating electrodes, J. Electrochem. Soc. 101 (6) (1954) 306.
[7] L.F. V.erdeja, R. Parra, F. Barbés Fernández, V. Bazán, Application of the nodal wear model to the static finger test of refractories corrosion, Steel Grips 3 (2) (2005) 105–110.
[8] A.R. C.ooper, The effect of the moving boundary on molecular diffusion controlled dissolution or growth kinetics, Trans. Faraday Soc. 58 (1962) 2468–2472.
[9] A.R. C.ooper, Modification of noyes-nernst equation, J. Chem. Phys. 38 (1) (1963) 284–285.
[10] J. Stefan, Versuche über die Verdampfung, Sitzungsberichte /Akad. der Wissenschaften Wien, Math. Klasse 68 (Abt. 2) (1873) 385–423.
[11] K. Gersten, H. Herwig, Grundlagen der Impuls-, Wärme- und Stoffübertragung aus asymptotischer Sicht. 1992.
[12] H.J. M.erk, Mass transfer in laminar boundary layers calculated by means of a perturbation method, Appl. Sci. Res. 8 (1) (1959) 237–260.
[13] H. Schlichting, K. Gersten, Boundary-Layer Theory, 9th Ed., Springer Berlin Heidelberg, Berlin, Heidelberg, 2017.
[14] J. Xin, L. Gan, L. Jiao, C. Lai, Accurate density calculation for molten slags in SiO2-Al2O3-CaO-MgO systems, ISIJ Int 57 (8) (2017) 1340–1349.
[15] J. Xin, N. Wang, M. Chen, L. Gan, Surface tension calculation of molten slag in SiO2–Al2O3–CaO–MgO systems based on a statistical modelling approach, ISIJ Int 59 (5) (2019) 759–767.
[16] M... Lighthill, Contributions to the theory of heat transfer through a laminar boundary layer, Proc. R. Soc. London. Ser. A. Math. Phys. Sci. 202 (1070) (Aug. 1950) 359–377.
[17] D.B. S.palding, Heat transfer from surfaces of non-uniform temperature, J. Fluid Mech. 4 (1) (1958) 22–32.
[18] A. Acrivos, Solution of the laminar boundary layer energy equation at high Prandtl numbers, Phys. Fluids 3 (4) (1960) 657–658.
[19] A. Acrivos, On the solution of the convection equation in laminar boundary layer flows, Chem. Eng. Sci. 17 (July 1961) (1962) 457–465.
[20] J. Newman, K.E. Thomas-Alyea, Electrochemical Systems (2004).
[21] M. Chen, R. Chalupa, A.C. W.est, V. Modi, High Schmidt mass transfer in a laminar impinging slot jet flow, Int. J. Heat Mass Transf. 43 (21) (2000) 3907–3915.
[22] G. Baier, T.M. G.rateful, M.D. G.raham, E.N. L.ightfoot, Prediction of mass transfer rates in spatially periodic flows, Chem. Eng. Sci. 54 (3) (1999) 343–355.
[23] A. Acrivos, The asymptotic form of the laminar boundary-layer mass-transfer rate for large interfacial velocities, J. Fluid Mech. 12 (3) (1962) 337–357.
[24] T.V. K.ármán, Über laminare und turbulente Reibung, ZAMM - J. Appl. Math. Mech. /Zeitschrift für Angew. Math. und Mech. 1 (4) (1921) 233–252.
[25] V.G. L.evich, Physicochemical Hydrodynamics, Prentice-Hall, Inc., 1962.
[26] W.G. C.ochran, The flow due to a rotating disc, Math. Proc. Cambridge Philos. Soc. 30 (3) (1934) 365–375.
[27] G.I. T.aylor, Stability of a Viscous Liquid Contained between Two Rotating Cylinders, Philos. Trans. R. Soc. A Math. Phys. Eng. Sci. 223 (605–615) (1923) 289–343.
[28] K.N. A.still, Studies of the developing flow between concentric cylinders with the inner cylinder rotating, J. Heat Transfer 86 (3) (1964) 383–391.
[29] J. Walowit, S. Tsao, R.C. D.iPrima, Stability of Flow Between Arbitrarily Spaced Concentric Cylindrical Surfaces Including the Effect of a Radial Temperature Gradient, J. Appl. Mech. 31 (4) (Dec. 1964) 585–593.
[30] K.S. B.all, B. Farouk, A flow visualisation study of the effects of buoyancy on Taylor vortices, Phys. Fluids A 1 (9) (1989) 1502–1507.
[31] M. Ali, P.D. W.eidman, On the stability of circular Couette flow with radial heating, J. Fluid Mech. 220 (12) (Nov. 1990) 53–84.
[32] J. Chen, J. Kuo, The linear stability of steady circular Couette flow with a small radial temperature gradient, Phys. Fluids A Fluid Dyn. 2 (9) (Sep. 1990) 1585–1591.
[33] T. Ma, S. Wang, Boundary-layer and interior separations in the Taylor-Couette-Poiseuille flow, J. Math. Phys. 50 (3) (2009).
[34] C. Kang, K.S. Y.ang, I. Mutabazi, Thermal effect on large-aspect-ratio Couette–Taylor system: numerical simulations, J. Fluid Mech. 771 (2015) 57–78.
[35] J.H. N.g, R.K. J.aiman, T.T. L.im, Interaction dynamics of longitudinal corrugations in Taylor-Couette flows, Phys. Fluids 30 (9) (2018).
[36] S. Chandrasekhar, Hydrodynamic and HydromagneticStability, Dover Publications, Inc., New York, 1961.
[37] H.A. S.nyder, Stability of rotating Couette flow. I. Asymmetric waveforms, Phys. Fluids 11 (4) (1968) 728–734.
[38] G. De Vahl Davis, R.W. T.homas, Natural convection between concentric vertical cylinders, Phys. Fluids 12 (12) (1969).
[39] J.E. B.urkhalter, E.L. K.oschmieder, Steady supercritical Taylor vortex flow, J. Fluid Mech. 58 (3) (1973) 547–560.
[40] J.E. B.urkhalter, E.L. K.oschmieder, Steady supercritical Taylor vortices after sudden starts, Phys. Fluids 17 (11) (1974) 1929–1935.
[41] I.G. C.hoi, S.A. K.orpela, Stability of the conduction regime of natural convection in a tall vertical annulus, J. Fluid Mech. 99 (4) (1980) 725–738.
[42] R.C. D.iPrima, P.M. E.agles, B.S. N.g, The effect of radius ratio on the stability of Couette flow and Taylor vortex flow, Phys. Fluids 27 (10) (1984) 2403.
[43] C.D. A.ndereck, S.S. L.iu, H.L. S.winney, Flow regimes in a circular Couette system, J. Fluid Mech. 164 (1986) (1986) 155–183.
[44] K.S. B.all, B. Farouk, Bifurfaction phenomena in Taylor-Couette flow with bouyancy effect, J. Fluid Mech. 197 (1988) 479–501.
[45] H.L. S.winney, J.P. G.ollub, Hydrodyanmic Instabilities and the Transition to Turbulence, 2nd ed., Springer Berlin Heidelberg, 1981.
[46] Y. Takeda, Quasi-periodic state and transition to turbulence in a rotating Couette system, J. Fluid Mech. 389 (1999) 81–99.
[47] O. Czarny, E. Serre, P. Bontoux, R.M. L.ueptow, Ekman vortices and the centrifugal instability in counter-rotating cylindrical Couette flow, Theor. Comput. Fluid Dyn. 18 (2–4) (2004) 151–168.
[48] T.B. B.enjamin, Bifurcation Phenomena in Steady Flows of a Viscous Fluid - 1, 2, Proc R Soc London Ser A 359 (1696) (1978) 1–43.
[49] T. Watanabe, Y. Toya, Vertical Taylor-Couette flow with free surface at small aspect ratio, Acta Mech 223 (2) (2012) 347–353.
[50] D.G. S.ceaeffer, Qualitative analysis of a model for boundary effects in the Taylor problem, Math. Proc. Cambridge Philos. Soc. 87 (2) (1980) 307–337.
[51] T.B. B.enjamin, T. Mullin, Anomalous modes in the taylor experiment, Proc. R. Soc. London, Ser. A Math. Phys. Sci. 377 (1770) (1981) 221–249.
[52] M. Lücke, M. Mihelcic, K. Wingerath, Front propagation and pattern formation of Taylor vortices growing into unstable circular Couette flow, Phys. Rev. A 31 (1) (1985) 396–409.
[53] I. Nakamura, Y. Toya, Existence of extra vortex and twin vortex of anomalous mode in Taylor vortex flow with a small aspect ratio, Acta Mech 117 (1–4) (Mar. 1996) 33–46.

[54] V. Sobolík, B. Izrar, F. Lusseyran, S. Skali, Interaction between the Ekman layer and the Couette-Taylor instability, Int. J. Heat Mass Transf. 43 (24) (2000) 4381–4393.
[55] O. Czarny, E. Serre, P. Bontoux, R.M. L.ueptow, Interaction between Ekman pumping and the centrifugal instability in Taylor-Couette flow, Phys. Fluids 15 (2) (2003) 467–477.
[56] M.J. B.urin, et al., Reduction of Ekman circulation within Taylor-Couette flow, Exp. Fluids 40 (6) (2006) 962–966.
[57] T. Watanabe, H. Furukawa, Y. Toya, Transition of free-surface flow modes in taylor-couette system, J. Vis. 10 (3) (2007) 309–316.
[58] U.T. B.ödewadt, Die Drehströmung über festem Grunde, ZAMM - J. Appl. Math. Mech. /Zeitschrift für Angew. Math. und Mech. 20 (5) (1940) 241–253.
[59] V.W. E.kman, On the influence of the earth's rotation on ocean-currents, Ark. Mat. Astr. Fys. 2 (11) (1905) 1–52.
[60] I. ANSYS, Ansys Fluent 12.0 Theory Guide. Lebanon, 2009.
[61] J.U. B.rackbill, D.B. K.othe, C. Zemach, A continuum method for modeling surface tension, J. Comput. Phys. 100 (2) (Jun. 1992) 335–354.
[62] K. Fagerlund, S. Sun, S. Jahanshahi, Effect of Marangoni-induced flow on the rate of refractory dissolution in molten slags, Scand. J. Metall. 31 (6) (Dec. 2002) 359–366.
[63] V. Kircher, Burhanuddin, H. Harmuth, Design, operation and evaluation of an improved refractory wear testing technique, Measurement 178 (Jun. 2021) 109429.
[64] K. Kataoka, H. Doi, T. Komai, Heat/mass transfer in taylor vortex flow with constant axial flow rates, Int. J. Heat Mass Transf. 20 (1) (1977) 57–63.
[65] C.C. W.an, J.E.R. Coney, An experimental study of diabatic spiral vortex flow, Int. J. Heat Fluid Flow 3 (1) (1982) 31–38.
[66] R. Kedia, M.L. H.unt, T. Colonius, Numerical simulations of heat transfer in taylor-couette flow, J. Heat Transfer 120 (1) (1998) 65–71.
[67] G. Baier, M.D. G.raham, E.N. L.ightfoot, Mass transport in a novel two-fluid Taylor vortex extractor, AIChE J 46 (12) (2000) 2395–2407.
[68] L. Gbahoue, Increase in mass transfer by the onset of Taylor-Couette-wise vortices, J. Enhanc. Heat Transf. 11 (1) (2004) 1–12.
[69] R. Srinivasan, S. Jayanti, A. Kannan, Effect of Taylor Vortices on mass transfer from a rotating cylinder, AIChE J 51 (11) (2005) 2885–2898.
[70] M. Kosaka, S. Minowa, Mass-transfer from solid metal cylinder into liquid metal, Tetsu-to-Hagane 52 (12) (1966) 1748–1762.

7.2 Publication II

Method for determination of effective binary diffusivities in dissolution of dense ceramic materials

Jerónimo Guarco, Burhanuddin, Sandra Vollmann, Harald Harmuth

Ceramics International 48 (2022) 7456–7463

Contents lists available at ScienceDirect

Ceramics International

journal homepage: www.elsevier.com/locate/ceramint

Method for determination of effective binary diffusivities in dissolution of dense ceramic materials

Jerónimo Guarco *, Burhanuddin, Sandra Vollmann, Harald Harmuth

Montanuniversität Leoben, Peter-Tunner Straße 5, 8700, Leoben, Austria

ARTICLE INFO

Keywords:
Corrosion (C)
Diffusion (C)
Wear resistance (C)
Al2O3 (E)
Dense ceramics

ABSTRACT

A method is proposed to determine the effective binary diffusivities in a dissolution of dense ceramics in liquid slags. This is achieved by combining computational fluid dynamics with a boundary layer approach to overcome the resolution problem that is associated with high Schmidt numbers. The rotating finger test experiment was performed with a dense alumina fine grain ceramic in a calcium aluminosilicate (CAS) slag. During the experiment, the sample dissolved, and the sample's shape deviated substantially from the initial cylindrical shape. The simulations were conducted in a middle step whereat the sample was already corroded, and the geometry was obtained from the laser measurements of the corroded surface. The diffusivities were evaluated via the average mass flux density and by fitting the experimental and simulation curves. Good agreement between the simulated and experimental corrosion profiles existed for the diffusivities evaluated by using the two methods.

1. Introduction

The wear of ceramic and refractory materials must be investigated because of the extreme temperatures and processing conditions that these materials are generally exposed to. A deeper understanding and quantification of the wear mechanisms will facilitate the development of highly wear resistant materials, which can be used for process optimization to minimize production costs. This work targets the quantification of the continuous wear of ceramic materials, which mainly encompasses two mechanisms: corrosion by dissolution and erosion. The focus herein is on the dissolution of dense ceramics, precisely that of alumina refractories. Here, the eroding effect of the liquid motion is minimized due to the dense structure of the material and small grain size.

Finger test experiments are very common for investigations of wear resistance of ceramic and refractory materials. Some studies conducted with these experiments can be found in Refs. [1–13]. These experiments can be conducted statically as well as dynamically by rotating the finger sample in the corroding medium, which resembles more closely the industrial applications of these materials [14,15]. While some investigations mainly focus on determining the wear mechanisms by microstructural investigations [1,2,7,8,10,12,13,16], others intend to quantify the wear through parameters [4–6,11,17]. For alumina dissolution, many authors acknowledged that the dissolution process is controlled by species diffusion through boundary layer [3,5,17,18]; thus quantification of wear generally involves calculations of mass transfer coefficients and effective binary diffusivities.

Sherwood correlations found in literature are frequently used to calculate mass transfer coefficients. One of the popular equations is the well-stablished equation of Levich [19] for disc shaped surfaces of infinite radius submerged in a semi-infinite medium. This equation provides an accurate approximation of mass flux density for real finite geometries when the velocity boundary layer thickness is much smaller than the disc radius [20]. Furthermore, the mass flux density is uniform over the disc surface, i.e. this equation can be applied to estimate the change in length of a cylindrical sample, as was conducted in the study of Cooper and Kingery [3] and Sandhage and Yurek [21]. However, some authors also used this equation to compute the total mass flux density from dissolution of a cylindrical sample [5,17,22] what seems not to be justified. This equation cannot predict the mass flux density of the cylinder mantle. Other authors have remedied this by using equations applicable to cylindrical shapes. For example, Um et al. [11] employed Eisenberg's equation [23] for this estimation. However, most equations found in literature did not include a clearance to the bottom of

Abbreviations: CFD, computational fluid dynamics; CAS, calcium aluminosilicate; VOF, volume of fluid; CSF, continuous surface force; AIC, Akaike information criterion; BIC, Bayes information criterion.

* Corresponding author.
E-mail address: jeronimo.guarco@unileoben.ac.at (J. Guarco).

https://doi.org/10.1016/j.ceramint.2021.11.264
Received 16 September 2021; Received in revised form 29 October 2021; Accepted 24 November 2021
Available online 26 November 2021

the crucible as it is the case with most finger test experiments. Although all equations are generally found for well-defined geometries such as ideal cylinders, the ceramic sample geometry can change substantially during the experiments. Therefore, it does not resemble an ideal cylindrical surface anymore. Furthermore, very frequently, these equations were obtained for much smaller Schmidt numbers than those typically valid for slags present in these set-ups.

Very often, a heat/mass transfer analogy is employed, and Nusselt correlations are translated into Sherwood equations for estimating mass flux density. In doing so, two effects are neglected. Firstly, there is a relative motion of the interface between solute and solution in dissolution processes, which is not the case for heat transfer (moving boundary problem). This effect adds a mass flux term and can be incorporated as introduced by Cooper [24]. Moreover, the boundary conditions of a heat transfer problem include zero relative velocity between the surface and fluid, not only parallel (no-slip condition) but also perpendicular to the surface, while for dissolution, a finite velocity normal to the surface known as Stefan's velocity must be considered in the boundary conditions, which also hinders this analogy. This Stefan velocity impacts the flow field and therefore also the mass transfer, what is not considered in the references quoted above. To give an example, merely applying the Levich equation for calculating the mass transfer at a rotating disc surface, does not yet include this effect, therefore results in a too small effective boundary layer thickness what overestimates the mass transfer. Further, neglecting the mass flow directly following from the Stefan velocity and equal to the product of Stefan velocity and concentration of dissolving species in the solution at the interface, underestimates the mass transfer.

The fundamentals of the methodology employed here was described in a previous study by the authors [25] for cylinder surfaces. This methodology accounts for the advection that occurs in an orthogonal direction to the solute/solvent interface and the effect of the Stefan's velocity on the boundary layer thickness. In addition, the computations are valid for large Schmidt numbers in the arrangement. Unlike the previous study, herein, the methodology is not applied to an ideal cylindrical surface but to real corroded surfaces. Conducting a simulation by considering the real shape of the dissolving specimen is expected to be a big step toward more accurate estimation of the diffusivity. To the best of the authors' knowledge, such a simulation has not been previously attempted.

The approach employed here allows the calculation of local, steady-state mass transfer coefficients. The obtained mass transfer coefficient profile is employed for computing the wear rate, which is used to predict the end worn out profile. Validation is provided with experimental results. Furthermore, the model is employed to calculate the diffusivities using two different methods. The initial and final surfaces of the sample are measured with a laser scanning device, which provides measurements over the entire cylindrical sample for several angular coordinates. To obtain a unique, axisymmetric curve, the profiles are averaged. A detailed description of the measuring method and processing of the profiles has been reported by Kircher et al. [26].

The objective of this study is to establish a more appropriate procedure for estimating effective binary diffusivities as the ones presented so far in literature. We will apply this procedure to a specific case of alumina dissolution. The evaluation procedure is improved, and the experimental setup is state-of-the-art as well. We also expect our estimations for slag properties to be more accurate than previous ones thanks to the larger availability of models and software present till date.

The following sections give a description of the experimental methods, the model used for the resolution of the flow field, and the methodology employed for computing the mass transfer coefficients. The simulation and experimental results are compared and discussed, and finally, the diffusivities are determined by applying two different methods.

2. Materials and methods

2.1. Experiment

The rotating finger test experiment was conducted for a pure dense alumina fine ceramic in a calcium aluminosilicate (CAS) slag; the slag properties are listed in Table 1. The slag was contained in a platinum crucible that is located in a furnace chamber, in which the temperature was controlled by thermocouples and it was constantly maintained at 1550 °C. The sample was immersed in the slag and rotated at a constant rotational speed of 200 rpm for 60 min. After this, the sample was lifted from the slag bath and was left to drip for 30 min. After this, laser measurements were conducted. A total of eight steps were performed. More information about the experimental set-up has been described in the study by Kircher et al. [26].

From the curves that were obtained by the laser measurement results, the corroded volume (ΔV) is computed and used to calculate the slag composition, immersed length ($\overline{L}$), average sample radius ($\overline{R}$) and average mass flux density ($\bar{j}_{exp}$). Table 1 presents the mean values of these quantities for single corrosion periods, which is calculated as the arithmetic mean between two consecutive measurements including the minimum radius measured ($\overline{R}_{tip}$). Step 0 represents the experiment start, and therefore in this case, there is no time averaging of the values presented. Furthermore, the slag composition in terms of mass fraction (w), density (ρ), viscosity (μ), and surface tension (σ) was determined at the beginning of each step. The density and surface tension were calculated with the correlations that were proposed by Xin [27,28], and the viscosity was calculated with the thermochemical software program FactSage v.7.2. These values were used to calculate the relevant dimensionless numbers: Reynolds $Re = \omega\overline{R}^2/\nu$, Weber: $We = \rho d(\omega\overline{R})^2/\sigma$, Capillarity: $Ca = \mu\omega\overline{R}/\sigma$, Taylor: $Ta = \frac{2\omega^2 d^4\eta^2}{\nu^2(1-\eta^2)}$, and Schmidt: $Sc = \nu/D$, which are displayed in Table 2. Here, d is the gap width between the crucible and the average sample radius, ω is the rotational speed, and ν is the kinematic viscosity. To compute the Schmidt number, we require the effective binary diffusivity, which is the quantity that we intend to calculate and is unknown. However, as a first approximation and with the intention of assessing the magnitude of these numbers, we referred to the report by Cooper and Kingery [3], in which the dissolution experiments with the same slag composition and temperature were conducted for three different configurations. These configurations are the molecular diffusion, free convection, and forced convection experiments. As a starting point, we have chosen the diffusivity that was evaluated from the molecular diffusion experiments, which has a value of $D = 3.0{\cdot}10^{-11}\ m^2/s$.

The properties of the slag do not change significantly with each step, and the relative changes between the start and end of the experiment are only 0.27% and 1.7% for the density and surface tension, respectively. Moreover, the calculated Schmidt numbers are very large; therefore, the asymptotic boundary layer approach is considered to be appropriate.

2.2. Simulation

The flow field was resolved with computational fluid dynamics (CFD) simulations using the software Ansys Fluent v.19 [29]. The volume of fluid (VOF) multiphase approach was employed for the resolution of the slag and atmosphere phases. Because the We and Ca numbers presented in Table 2 are not large enough to neglect the effects of the surface tension, these are incorporated with the continuous surface force (CSF) model. The model was laminar, 2D, and axisymmetric. This hypothesis was supported by the range of Reynolds numbers presented in Table 2. More importantly, the flow regimen was characterized by the Taylor number, which gives the ratio of the centrifugal to the viscous forces. In annular set-ups with rotating cylinders, centrifugal instabilities are known to develop after a critical Taylor number is

Table 1
Slag/refractory properties.

	w_{CaO}	$w_{Al_2O_3}$	w_{SiO_2}	$\bar{j}_{exp}$ (kg/(m^{2}s))	μ (Pa s)	ρ (kg/m^3)	σ (mN/m)	$\bar{R}$ (mm)	$\bar{R}_{tip}$ (mm)	$\bar{L}$ (mm)
0	0.3807	0.2100	0.4093	–	0.6423	2589	476.9	10.14	10.14	54.29
1	0.3774	0.2168	0.4058	7.988E-4	0.6652	2590	477.9	9.86	9.49	53.01
2	0.3720	0.2281	0.3999	6.049E-4	0.7045	2591	479.6	9.30	8.20	51.21
3	0.3680	0.2363	0.3957	5.470E-4	0.7354	2592	480.8	8.82	7.10	49.99
4	0.3646	0.2433	0.3920	5.559E-4	0.7624	2593	481.8	8.37	6.16	49.21
5	0.3616	0.2496	0.3888	5.193E-4	0.7877	2594	482.8	7.96	5.40	48.28
6	0.3588	0.2554	0.3858	5.970E-4	0.8118	2595	483.7	7.56	4.74	46.77
7	0.3563	0.2607	0.3831	5.520E-4	0.8335	2596	484.5	7.24	4.31	45.23
8	0.3544	0.2647	0.3810	4.069E-4	0.8514	2596	485.1	7.01	4.21	43.50

Table 2
Dimensionless numbers.

	Re	Sc	We	Ca	Ta
0	8.7	8.3E6	5.5	0.3	384
1	7.9	8.6E6	5.2	0.3	354
2	6.7	9.1E6	4.8	0.3	307
3	5.7	9.5E6	4.4	0.3	272
4	5.0	9.8E6	4.0	0.3	244
5	4.4	1.0E7	3.7	0.3	220
6	3.8	1.0E7	3.4	0.3	198
7	3.4	1.1E7	3.1	0.3	181
8	3.1	1.1E7	2.9	0.3	168

exceeded. The first appearing regimen is known as the Taylor-Couette regime, which was described by Taylor [30], who mathematically studied the locus of the transitions. For our experimental set-up, we calculated these critical values on the basis of the results reported by DiPrima et al. [31]. The lowest critical Taylor number corresponds to the first step and it is $Ta_{crit} = 5161$. Because all values that are presented in Table 2 are well below this value, we can conclude that no such instabilities should form.

The boundary conditions are summarized in Fig. 2; they include an axis of symmetry along the axis of the ceramic sample, a pressure outlet at the top, a no-slip condition on the crucible walls, and a constant rotational speed on the refractory surface. The density is considered to be constant with the value of the initial slag that is presented in Table 1 and with all other properties listed in this table. A detailed description of the model and the underlying equations can be found in Ref. [25].

The simulations were conducted for a worn sample after 3 h of corrosion, in which the geometry significantly deviates from a perfect cylindrical surface. To generate the geometry that is used in the CFD model, we used the processed measured laser profile in the third step, i.e., 3 h of corrosion. The scanned surface has a very high resolution; however, to produce the sample geometry for the CFD model, we used a smooth approximation of this profile with splines by connecting 12 points. A further step involves using a smoothing tool to avoid unrealistic topologies. The exact geometry of the sample tip is unknown because it is impossible to perform laser measurements on this surface due to the retention of a thick slag droplet that scatters the laser beam. To construct the complete geometry for the simulations, this part was drawn with an arbitrary curvature. There is, therefore, some small uncertainty in the actual immersed length and the shape of this part. The

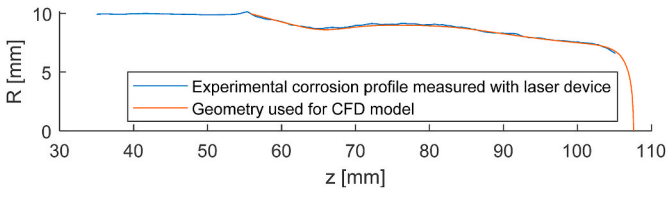

Fig. 1. Comparison of the corrosion curve obtained through laser measurement and the approximation used for the model after 3 h of corrosion.

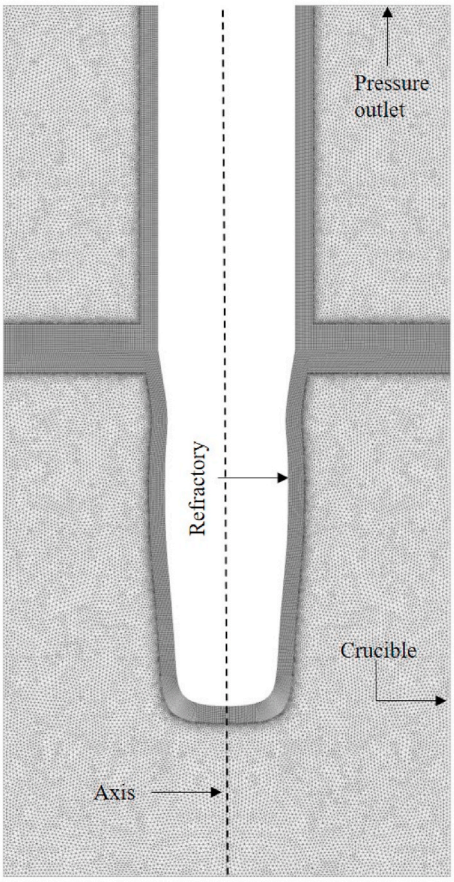

Fig. 2. Meshing of the simulation domain.

approximated shape of the tip only serves the simulation of the flow field. The mass flux from this surface part was calculated by applying Levich's [19] equation for a disc surface, in which the disc radius is considered as the minimum radius measured by the laser device. This value is also presented in Table 1. In Fig. 1, a comparison between the geometry that is obtained on the basis of the laser measurement results and the approximation that is used for the model is displayed.

The mesh of the worn sample consists of quadrilateral and triangular elements. The immediate vicinity of the solute/solution interface is meshed with quadrilateral elements, as well as is the area of the slag/atmosphere interface, for a better resolution of surface tension effects.

The CFD simulations were employed exclusively for the resolution of the flow field. The transport equations for the species were not solved within the model. However, it was treated by a post-processing step through an approach based on the boundary layer theory, as described in our previous study [25]. All relevant effects were incorporated, and the mass transfer coefficients (k_c) were calculated using the following

formula:

$$k_c = \frac{\chi_D}{1 - w_s} \frac{DSh_0}{L} \tag{1}$$

where w_s is the alumina saturation mass fraction, Sh_0 is the Sherwood number without considering the influence of the interface advection on the boundary layer thickness, and χ_D is a correction factor for this effect. Unlike our previous study, herein, the integral that is needed to calculate Sh_0 is unavoidably a line integral because the curve is no longer easily represented by Cartesian coordinates, which results in Equation (2). Here, x is the local coordinate along the line that represents the worn profile, β is a directional derivative of the velocity that is tangential to the surface in the direction normal to it, and $\mathscr{R}$ the radius of the revolution surface at position x. The last two variables vary along the curve, unlike the case of the mantle of an ideal cylindrical surface where only β is a function of the coordinates. This line integral is evaluated numerically with the trapezoidal rule. Variable β is calculated with Equation (3) and the wall shear stresses are defined by Equation (4). According to the software documentation [32], the axial wall shear stress (τ_z) considers the derivative of the axial velocity in the direction normal to the surface. In addition, the radial wall shear stress (τ_r) considers that of the radial velocity in the normal direction.

$$Sh_0(x) = \frac{L\, Sc^{1/3}}{9^{1/3}\, \nu^{1/3} \Gamma(4/3)} \sqrt{\mathscr{R}\, \beta(x)} \left[\int_s \mathscr{R} \sqrt{\mathscr{R}\beta(\zeta)} ds \right]^{-1/3} \tag{2}$$

$$\beta = \frac{\partial v_t}{\partial \hat{n}} = \frac{\partial (\vec{v} \cdot \hat{t})}{\partial \hat{n}} = \frac{\partial \vec{v}}{\partial \hat{n}} \cdot \hat{t} = \frac{1}{\mu} (\tau_z \hat{e}_z + \tau_r \hat{e}_r) \tag{3}$$

$$\tau_{w,i} = \mu \frac{\partial v_i}{\partial \hat{n}} \tag{4}$$

In Equations (2)–(4): L is the characteristic length ; v_t is the velocity component that is tangential to the surface; $\hat{n}$ is a unit vector that is normal to the surface; $\hat{t}$ is a unit vector that is in the tangential direction ; $\vec{v}$ is the velocity vector; and $\hat{e}_z$ and $\hat{e}_r$ are the axial and radial unit vectors, respectively.

For the verification of grid independence, two different mesh sizes were employed having $\Delta x = 0.125$ mm and $\Delta x = 0.0625$ mm. The total number of elements considered for the coarse and fine grids is 58,100 and 232,400, respectively.

3. Results and discussion

3.1. Experimental results

A total of eight steps were conducted; the corresponding corrosion curves are displayed in Fig. 3, which includes measuring the pristine sample.

In Fig. 3, by starting from the nearly ideal cylindrical shape, the wear of the sample is not uniform, and this becomes more noticeable in the later steps. Two features can be easily recognized. The first feature is that the bottom region is prone to higher wear rates. The second feature is that the region of the slag/atmosphere interface has lower wear rates. These results agree with the findings of our previous study [25]; however, these were only applicable to ideal cylindrical samples. The alteration of the geometry can influence the flow field and, ergo, has a direct effect on the mass transfer coefficients profile. From the consecutive profiles, it is possible to compute an experimental wear rate, which is displayed in Fig. 4, for the first three steps for clearer visualization.

The wear rates for the three steps were qualitatively similar, and as expected, they decreased with time. We can observe higher wear rates that are close to the end of the sample and smaller rates that are close to the slag/atmosphere interface; the wear rate is at a maximum between these two regions.

3.2. Simulation results

The simulation of the flow field shows that for the corroded sample, the flow field is slightly different than that shown in our previous study based on ideal cylindrical samples [25]. In Fig. 5, the path lines coloured by the phase volume fraction are displayed. In our previous study [25], we could observe an Ekman vortex in the vicinity of the slag/atmosphere interface which is not present here anymore.

To determine Sh_0, variable β is shown in Fig. 6 for the mantle surface, where the independence of the grid size is also noticed.

The use of Equation (2) with the above β profile and the known outline of the mantle surface resulted in the $Sh_0/Sc^{1/3}$ profile that is depicted in Fig. 7 for the cylinder mantle. The characteristic length that is used for Sh_0 is the gap width d. In this figure, the independence of the grid fineness is also observed. Although the cylinder tip is not based on the real measurements of this surface, the mass transfer coefficient profile is shown in Fig. 8 for the approximated geometry with average tip radius $\overline{R}_{tip}$ being the characteristic length that is employed.

These results show the same behaviour as the experimental wear rates that are shown in Fig. 4. Higher wear rates are observed towards the end of the sample, and the maximum wear rate exists between this region and the region of the slag/atmosphere interface whereat the corrosion rate is low. This provides a qualitative degree of the validation to the model, its hypothesis, and approximations. Furthermore, it allows us to employ the methodology to determine the diffusivities with more confidence.

Lastly, we review the main differences with our previous investigations for perfect cylindrical surfaces [25] with the results obtained here. The application of the asymptotic boundary layer method for the perfect cylindrical surface is more straightforward given that the geometry is easily described in cartesian coordinates, and for this method, only axial stresses are necessary for the cylinder mantle and

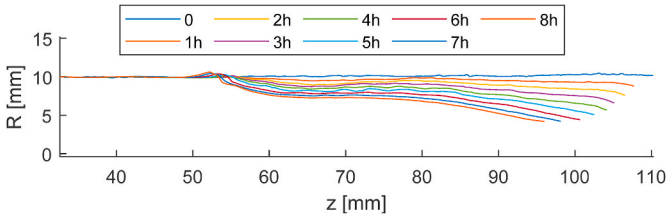

Fig. 3. Measured corrosion profiles.

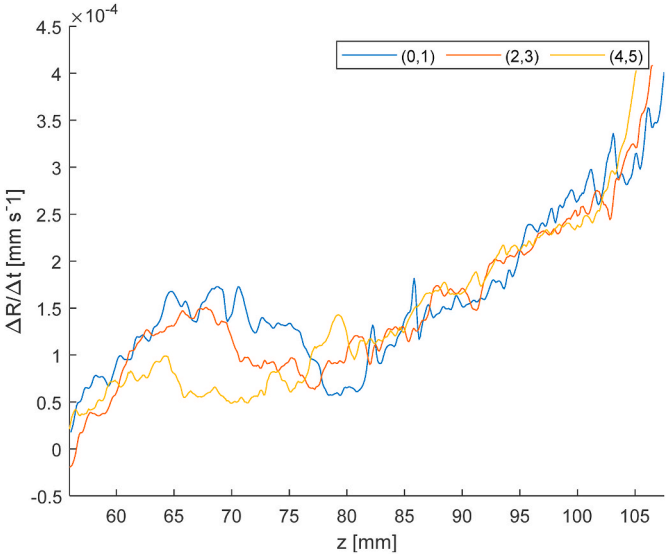

Fig. 4. Experimental wear rates for the first three dissolution steps.

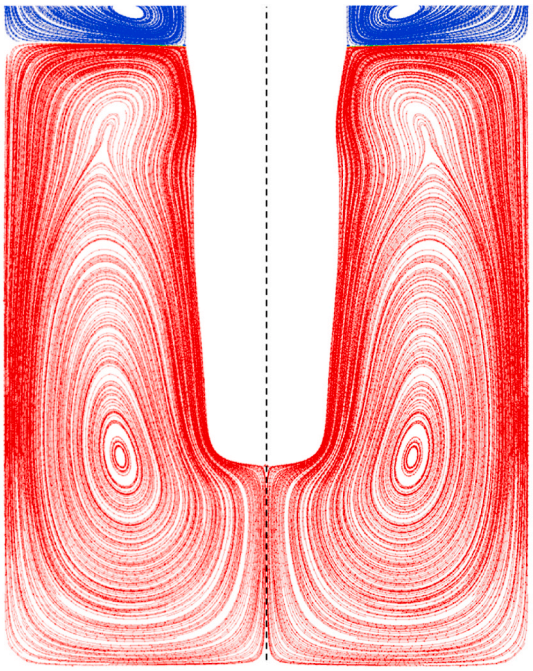

Fig. 5. Flow field path lines that are coloured red for the slag and blue for the atmosphere after 3 h of corrosion. (For interpretation of the references to colour in this figure legend, the reader is referred to the Web version of this article.)

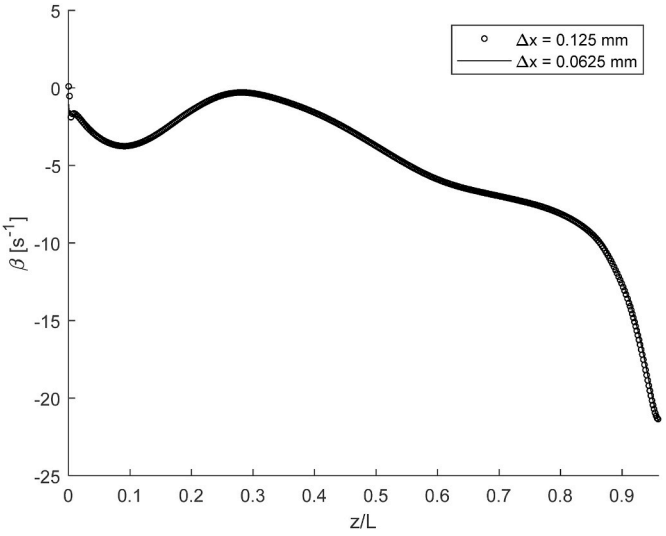

Fig. 6. β over the mantle after 3 h of corrosion (L = submerged length).

radial stresses for the tip of the sample. However, for the corroded surface, the line integral has to account for the continuous change in geometry as well as the variations in axial and radial shear stresses for both mantle and tip. For cylinder surfaces, we observed an Ekman vortex in the vicinity of the slag/atmosphere interface, which resulted in an inflection point on β and therefore in a minimum in the Sherwood profiles where the vortical structures meet. This structure is no longer present in the investigations performed in this work; and the axial flow induced by the rotation of the sample tip ascends further into the annular region, however, we still observe a minimum and maximum of the Sherwood profile over the sample mantle, even when β remains negative over the whole region, therefore these features are strongly dependent on the geometrical aspect of the corroded sample. Naturally, some commonalities are maintained between these configurations; in

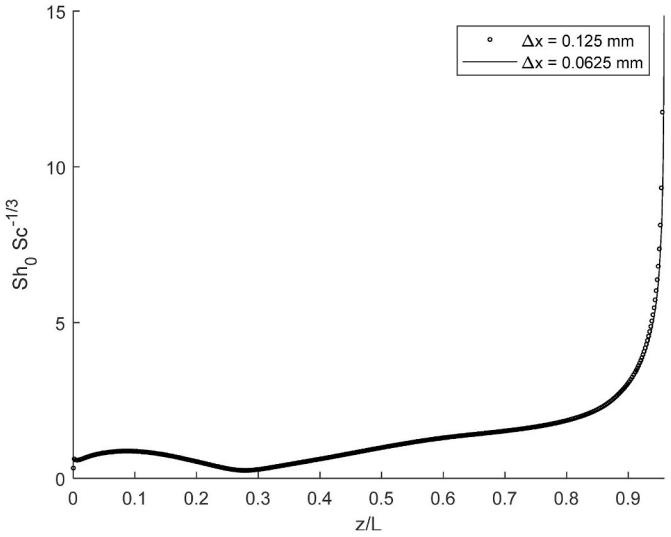

Fig. 7. Local $Sh_0/Sc^{1/3}$ on the specimen mantle of the corroded sample (L = submerged length).

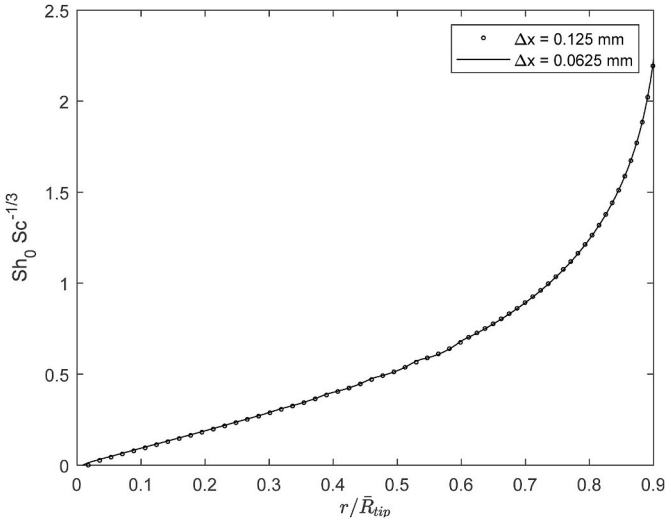

Fig. 8. Local $Sh_0/Sc^{1/3}$ on the cylinder tip.

both cases, the largest wear rates are observed towards the tip of the sample and the lowest at the slag/atmosphere interface.

3.3. Diffusivity calculations

The binary diffusivity was calculated by two different approaches.

3.3.1. Diffusivity calculation based on mass flux density

The first approach consists of employing the experimental average mass flux density ($\bar{j}_{exp}$) to determine the diffusivity value that results in the same theoretical/simulation mass flux density ($\bar{j}_{model}$). In this study, the average experimental mass flux density is computed from the product of the corroded volume (ΔV) during one step, i.e., 1 h of the dissolution time (Δt) with the refractory density (ρ^r) that is divided by Δt and the dissolution area (A), which is measured with the laser device.

$$\bar{j}_{exp} = \frac{\rho^r \Delta V}{A \Delta t} \tag{5}$$

Moreover, the average mass flux density is computed from the area weighted average between the mantle (1) and the tip (2). The former is

calculated as shown above with the average of the data that is displayed in Fig. 7 and the latter is calculated by using Levich's equation. This results in the following expression.

$$\bar{j}_{model} = k_c \Delta c = \frac{1}{A_1 + A_2}(A_1 \bar{k}_1 + A_2 \bar{k}_2)\Delta c \tag{6}$$

$\bar{k}_c$ is calculated from Equation (1), in which the unknown diffusivity allows the determination of $Sh_0 Sc^{-1/3}$. By correlating Equations (5) and (6) and after performing an algebraic manipulation, the following expression is obtained.

$$D^{2/3} = \frac{\bar{j}_{exp}\, d}{\chi_D B \rho^s G \nu^{1/3}} \tag{7}$$

where B is the mass transfer parameter $B = (w_s - w_\infty)/(1 - w_s)$; ρ^s and ν are the slag density and viscosity, respectively; and $G = \overline{Sh}_0\, Sc^{-1/3}$, as shown in Figs. 7 and 8. The value of G is obtained by an area weighted average of the tip and mantle contributions. From this, $\overline{Sh}_0$ from the tip of the sample is modified by multiplying it with d/R so it has the same characteristic length, d, as the mantle and it is used in Equation (7).

$$G = \frac{1}{A_1 + A_2}(A_1 G_1 + A_2 G_2) \tag{8}$$

With this approach, two diffusivities were calculated. The first diffusivity, $D = 5.06{\cdot}10^{-11}\ (m^2/s)$, corresponds to the calculation that uses the simulation $Sh_0\, Sc^{-1/3}$ profile for the mantle and Levich's equation for the unknown tip. The second value, $D = 5.52{\cdot}10^{-11}\ (m^2/s)$, is calculated by using the simulations for the mantle and the approximation to the tip and has a minor deviation from the diffusivity by using a simulation for the mantle and Levich's equation for the tip. Therefore, we conclude that the approximation of the unknown tip geometry does not significantly influence the end value of the diffusivity.

Furthermore, with the known diffusivity, we are able to compute a prediction for the corroded profile at the end of the 1 h dissolution step by interpolating the local mass transfer coefficient profile that is obtained with a simulation to the laser measurement at the beginning of the step. The prediction is done with a solute mass balance. This is achieved by integrating the rate of the solute radius change (Equation (9)) under the hypothesis that this flux remains constant during the integration.

$$\frac{dR}{dt} = \frac{-1}{\rho^r} j_{model} \tag{9}$$

Subsequently, we compared this prediction for the corrosion profile at 3 h of corrosion with the laser measurements, in which we observed good agreement between the curves.

3.3.2. Diffusivity calculation by curve fitting

The second approach is motivated by the good agreement between the measured and simulated profiles for the end of the step shown in Fig. 9. A least-squares problem was formulated in which the diffusivity is the design variable. The advantage of this method is that no assumptions are needed for the mass flux from the tip of the sample. This is because we only focused on fitting the predicted simulation profile to the laser measurement at the end of the step. The minimization problem was solved by using MATLAB's unconstrained, derivative-free, fminunc solver, which is based on the Nelder-Mead simplex algorithm. The solution is the global minimum and the value of the optimum is $D = 4.80{\cdot}10^{-11} m^2/s$. The fitting can be observed in Fig. 10. This diffusivity is comparable to the values in Table 3, wherein two indicators of the goodness of the solution are displayed, namely, the Akaike information criterion (AIC) and the Bayes information criterion (BIC). A clear explanation of the calculation and interpretation of these parameters can be found in a study by Spiess et al. [33]. These indicators are used to compare the different models and the models with the lowest values (the highest absolute values) are considered to be optimal. Clearly, the optimal result was obtained by fitting the model to the experimental data with the least-squares problem. In addition, in this table, the error that is incurred by using the other approaches were compared to the curve fitting, which is given in the last column. From this, we can conclude that the methods are consistent, and they provide similar results.

For this solution, we also computed the 95% confidence interval, $D = [4.63 \cdot 10^{-11} 4.97 \cdot 10^{-11}]$.

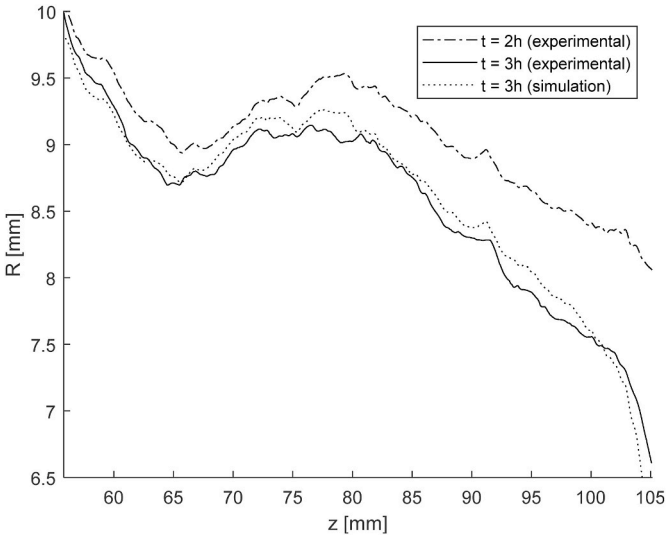

Fig. 9. Experimental corrosion profile and simulated corrosion profile after 3 h of dissolution.

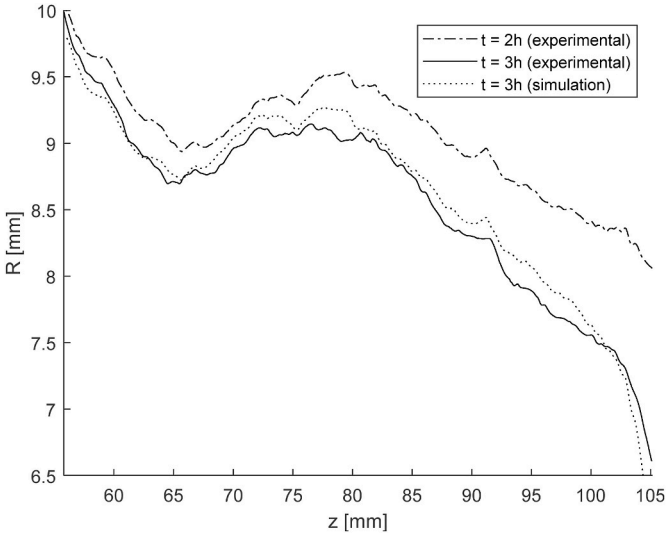

Fig. 10. Experimental corrosion profile and simulated profile after 3 h of dissolution with diffusivity out of curve fitting method.

Table 3
Diffusivity values and statistical indicators.

Disc	Mantle	D (m^2/s)	AIC	BIC	Error
Levich	Simulation	5.06E-11	−481.0	−476.9	5.4%
Simulation	Simulation	5.52E-11	−427.6	−423.4	15.0%
–	Curve Fit	4.80E-11	−489.9	−485.7	–

3.4. Literature discussion

The results (Section 3.3.2) were compared with the relevant reported mass transfer equations, which can be found in our previous publication [25], where we found a good qualitative agreement between the data trend and the equations by Eisenberg et al. [23] and Kosaka and Minowa [34] for the typical Reynolds range of these experiments. In terms of the error, the closest relation was between the Kosaka and Minowa equations with an error of 7–19%. All these calculations and comparisons were conducted for the ideal cylindrical samples. The comparison here is for the corroded surface; the comparison results are summarized in Table 4, in which all the equations with average quantities were employed. As expected, a larger deviation from the simulated values as with the case of an ideal cylindrical sample is observed. The smallest error is obtained with a modified version of the equation by Tachibana et al. [35], in which the $Sc^{1/4}$ factor is exchanged with $Sc^{1/3}$. However, a sound theoretical background for the utilization of this equation is lacking because the flow regimen is entirely different. The second-best approximation is given by Eisenberg's equation, which has a relative error of 30%.

In Section 2.1, we introduced a study by Cooper and Kingery [3] and employed diffusivity values presented by these authors as a first approximation to estimate the Schmidt numbers. This section compares their results with the diffusivities that were calculated with our methods. In their study, three different configurations were employed with a different evaluation method to determine the diffusivity. Starting with the molecular diffusion experiments, the evaluation method that was employed is the one that was previously proposed by Cooper [36]. For these investigations, the experimental times were much shorter than those in the investigations based on natural and forced convection. This is because the static fluid used for pure molecular diffusion cannot be maintained. After a certain time, the appearance of natural convection and/or hydrodynamic instabilities is unavoidable. However, for a static sample at 1550 °C and under 15 min, the experimental data appear to be reasonably well explained by pure molecular diffusion; therefore, the presented value of diffusivity $D = 3{\cdot}10^{-11}\ m^2/s$ is noteworthy. For the natural convection, a Sherwood correlation for the vertical cylinders was employed and the change in the radius of the sample was used to compute the average mass flux density. Forced convection experiments were also conducted using a rotating cylinder that had a smaller length to radius ratio. However, the mass loss from the cylinder mantle was not investigated because they measured the length of the cylinder with time, which became smaller due to the dissolution from the disc-shaped surface. For this surface, the authors employed Levich's equation to calculate the mass transfer rate. Given that their experiments were conducted at a much higher rotational speed (1200 rpm) and as observed in our previous study with a similar set-up [25], it is expected that Levich's equation can accurately describe this mass flux very. Nevertheless, the evaluation method that these authors employed for the experiments in natural and forced convection both lack the correction for the influence of the Stefan velocity on the species boundary layer thickness. For their evaluation method for the forced convection experiments, this correction is easily achievable. Introducing this rectification results in a diffusivity value of $D = 6.69{\cdot}10^{-11} m^2/s$. It is assumed that this value is more reliable than the other two reported in Ref. [3] because of the clear definition of the Sherwood number. These values agree reasonably well with our calculation, with the largest error being 29%.

The main differences to the discussed literature and references provided in the introduction section are owed to the incorporation of dissolution-related phenomena which are commonly neglected: firstly, in our method, we account for the advection of the solute/solution interface and also its effect on the boundary layer thickness. Secondly, a more accurate estimation of the Sherwood number is given by conducting a simulation of the actual sample shape, where no approximations are taken by using reported Sherwood equations that do not exactly correlate with the finger test set-up. A drawback of this is that unlike the correlations used by other authors where the radius or length of the sample are used for computing Sherwood numbers no clear global parameters are identifiable in this method because the shape of the geometry is approximated with higher accuracy. Moreover, the appropriateness of the handling of large Schmidt numbers is assured by the asymptotic boundary layer method, whereas most reported Sherwood or Nusselt's relationships are given for much smaller Schmidt or Prandtl numbers.

Table 4
Comparison of the Sherwood number for the model and documented equations.

	Sh_0	Error (%)
Simulation	215.1	–
Tachibana	190.8	11.3
Eisenberg	150.8	29.9
Kosaka	98.45	54.2
Srinivasan	74.44	65.4

4. Conclusions

The calculations of the mass transfer coefficients for the dissolution of a pure dense alumina fine ceramic in a liquid CAS slag were performed for a worn ceramic sample. The calculations were conducted for an already corroded geometry that was approximated from the laser measurements of a real sample. Good qualitative agreement was observed between the experimental wear rates and the calculated mass transfer coefficient profile. These results strengthened the model, which allows for an accurate estimation of the effective binary diffusivity.

This might be regarded as a main disadvantage of this method because it is very case-specific because the geometry is not easily described by global parameters. But for this same reason, it is precisely relevant because there are currently no equations that are available in the literature for these set-ups. In particular, we consider the progressive change of the geometry within the experiment and the deviation from a cylindrical shape. When comparing some documented equations for the cylindrical geometries, we determined that the equation by Eisenberg et al. [23] is a good approximation for the mass flux density that comes from the dissolution of the cylinder mantle.

The effective binary diffusivity was determined by applying two different methods. The first approach equalized the experimental mass flux density with the average mass flux density that was calculated with the simulation. The second method applied curve fitting along the end worn profile with a simulated profile. We believe that the latter approach is the most accurate because it includes fewer approximations for the unknown geometry of the tip sample; however, both methods are consistent in that they deliver similar results. In addition, the values for both methods agree reasonably well with the values that were reported by Cooper and Kingery [3].

The methodology emerges as trustable and it provides a valuable tool to characterize the wear resistance of ceramic materials in different systems, which can potentially be used for process and cost optimization.

Declaration of competing interest

The authors declare that they have no known competing financial interests or personal relationships that could have appeared to influence the work reported in this paper.

Acknowledgments

The authors gratefully acknowledge the financial support under the scope of the COMET program within the K2 Center "Integrated

Computational Material, Process and Product Engineering (IC-MPPE)" (Project No 859480). This program is supported by the Austrian Federal Ministries for Climate Action, Environment, Energy, Mobility, Innovation and Technology (BMK) and by the Digital and Economic Affairs (BMDW). This is represented by the Austrian research funding association (FFG), and the federal states of Styria, Upper Austria, and Tyrol.

References

[1] L. Chen, A. Malfliet, P.T. Jones, B. Blanpain, M. Guo, Influence of Al2O3 level in CaO-SiO2-MgO-Al2O3 refining slags on slag/magnesia-doloma refractory interactions, Metall. Mater. Trans. Mater. Process. Sci. 50 (2019) 1822–1829, https://doi.org/10.1007/s11663-019-01596-y.

[2] W.K. Banda, J.D. Steenkamp, E. Matinde, An investigation into the wear mechanisms of carbon- and silicon carbide-based refractory materials by silicomanganese alloy, J. South. African Inst. Min. Metall. 120 (2020) 333–344, https://doi.org/10.17159/2411-9717/959/2020.

[3] A.R. Cooper, W.D. Kingery, Dissolution in ceramic systems: I, molecular diffusion, natural convection, and forced convection studies of sapphire dissolution in calcium aluminum silicate, J. Am. Ceram. Soc. 47 (1964) 37–43, https://doi.org/10.1111/j.1151-2916.1964.tb14638.x.

[4] S. Jansson, V. Brabie, P. Jönsson, Corrosion mechanism of commercial doloma refractories in contact with CaO-Al2O3-SiO2-MgO slag, Ironmak. Steelmak. 35 (2008) 99–107, https://doi.org/10.1179/030192307X231595.

[5] A.H. Bui, H.M. Ha, I.S. Chung, H.G. Lee, Dissolution kinetics of alumina into mold fluxes for continuous steel casting, ISIJ Int. 45 (2005) 1856–1863, https://doi.org/10.2355/isijinternational.45.1856.

[6] J. Jeon, Y. Kang, J.H. Park, Y. Chung, Corrosion-erosion behavior of MgAl2O4 spinel refractory in contact with high MnO slag, Ceram. Int. 43 (2017) 15074–15079, https://doi.org/10.1016/j.ceramint.2017.08.034.

[7] L. Chen, M. Guo, H. Shi, S. Huang, P.T. Jones, B. Blanpain, A. Malfliet, Effect of ZnO level in secondary copper smelting slags on slag/magnesia-chromite refractory interactions, J. Eur. Ceram. Soc. 36 (2016) 1821–1828, https://doi.org/10.1016/j.jeurceramsoc.2016.02.004.

[8] L. Chen, M. Guo, H. Shi, L. Scheunis, P.T. Jones, B. Blanpain, A. Malfliet, The influence of ZnO in fayalite slag on the degradation of magnesia-chromite refractories during secondary Cu smelting, J. Eur. Ceram. Soc. 35 (2015) 2641–2650, https://doi.org/10.1016/j.jeurceramsoc.2015.03.013.

[9] D. Kim, H.T. Kim, S.S. Ryu, H.J. Kim, Microstructure changes of aluminum titanate refractory doped SiO2 and ZrO2 in molten steel, J. Korean Inst. Met. Mater. 53 (2015) 116–122, https://doi.org/10.3365/KJMM.2015.53.2.116.

[10] H. Um, K. Lee, K.Y. Kim, G. Shin, Y. Chung, Effect of carbon content of ferromanganese alloy on corrosion behaviour of MgO-C refractory, Ironmak. Steelmak. 41 (2014) 31–37, https://doi.org/10.1179/1743281212Y.0000000098.

[11] H. Um, K. Lee, J. Choi, Y. Chung, Corrosion behavior of MgO-C refractory in ferromanganese slags, ISIJ Int. 52 (2012) 62–67, https://doi.org/10.2355/isijinternational.52.62.

[12] M. Guo, S. Parada, P.T. Jones, J. Van Dyck, E. Boydens, D. Durinck, B. Blanpain, P. Wollants, Degradation mechanisms of magnesia-carbon refractories by high-alumina stainless steel slags under vacuum, Ceram. Int. 33 (2007) 1007–1018, https://doi.org/10.1016/j.ceramint.2006.03.009.

[13] M. Guo, P.T. Jones, S. Parada, E. Boydens, J.V. Dyck, B. Blanpain, P. Wollants, Degradation mechanisms of magnesia-chromite refractories by high-alumina stainless steel slags under vacuum conditions, J. Eur. Ceram. Soc. 26 (2006) 3831–3843, https://doi.org/10.1016/j.jeurceramsoc.2005.12.025.

[14] W.E. Lee, S. Zhang, Melt corrosion of oxide and oxide-carbon refractories, Int. Mater. Rev. 44 (1999) 77–104, https://doi.org/10.1179/095066099101528234.

[15] C. Reynaert, E. Śnieżek, J. Szczerba, Corrosion tests for refractory materials intended for the steel industry - a review, Ceram. - Silikaty. 64 (2020) 278–288, https://doi.org/10.13168/cs.2020.0017.

[16] M. Guo, S. Parada, P.T. Jones, E. Boydens, J.V. Dyck, B. Blanpain, P. Wollants, Interaction of Al2O3-rich slag with MgO-C refractories during VOD refining-MgO and spinel layer formation at the slag/refractory interface, J. Eur. Ceram. Soc. 29 (2009) 1053–1060, https://doi.org/10.1016/j.jeurceramsoc.2008.07.063.

[17] G.Y. Shi, T.A. Zhang, Z.H. Dou, L.P. Niu, Dissolution behavior of al2o3 inclusions in cao-al2o3 based slag representing aluminothermic reduction slag, Crystals 10 (2020) 1–12, https://doi.org/10.3390/cryst10111061.

[18] L. Deng, F. Yun, R. Jia, H. Li, X. Jia, Y. Shi, X. Zhang, Effect of SiO2/MgO ratio on the crystallization behavior, structure, and properties of wollastonite-augite glass-ceramics derived from stainless steel slag, Mater. Chem. Phys. 239 (2020), https://doi.org/10.1016/j.matchemphys.2019.122039.

[19] V.G. Levich, Physicochemical Hydrodynamics, Prentice-Hall, Inc., 1962, https://doi.org/10.1021/ed040pA827.2.

[20] W.G. Cochran, The flow due to a rotating disc, Math. Proc. Camb. Phil. Soc. 30 (1934) 365–375, https://doi.org/10.1017/S0305004100012561.

[21] K.H. Sandhage, G.J. Yurek, Direct and indirect dissolution of sapphire in calcia–magnesia–alumina–silica melts: dissolution kinetics, J. Am. Ceram. Soc. 73 (1990) 3633–3642, https://doi.org/10.1111/j.1151-2916.1990.tb04269.x.

[22] I. Kasimagwa, V. Brabie, P.G. Jönsson, Slag corrosion of MgO–C refractories during secondary steel refining, Ironmak. Steelmak. 41 (2014) 121–131, https://doi.org/10.1179/1743281213Y.0000000110.

[23] M. Eisenberg, C.W. Tobias, C.R. Wilke, Ionic mass transfer and concentration polarization at rotating electrodes, J. Electrochem. Soc. 101 (1954) 306, https://doi.org/10.1149/1.2781252.

[24] A.R. Cooper, Modification of noyes-nernst equation, J. Chem. Phys. 38 (1963) 284–285, https://doi.org/10.1063/1.1733489.

[25] J. Guarco, H. Harmuth, S. Vollmann, Method for determination of mass transfer coefficients for dissolution of dense ceramics in liquid slags, Int. J. Heat Mass Tran. 186 (2021), 122494, https://doi.org/10.1016/j.ijheatmasstransfer.2021.122494.

[26] V. Kircher, Burhanuddin, H. Harmuth, Design, operation and evaluation of an improved refractory wear testing technique, Measurement 178 (2021), 109429, https://doi.org/10.1016/j.measurement.2021.109429.

[27] J. Xin, L. Gan, L. Jiao, C. Lai, Accurate density calculation for molten slags in SiO2-Al2O3-CaO-MgO systems, ISIJ Int. 57 (2017) 1340–1349, https://doi.org/10.2355/isijinternational.ISIJINT-2017-070.

[28] J. Xin, N. Wang, M. Chen, L. Gan, Surface tension calculation of molten slag in SiO2–Al2O3–CaO–MgO systems based on a statistical modelling approach, ISIJ Int. 59 (2019) 759–767, https://doi.org/10.2355/isijinternational.ISIJINT-2018-746.

[29] Ansys®, Ansys Fluent, (n.d.).

[30] G.I. Taylor, Stability of a viscous liquid contained between two rotating cylinders, Philos. Trans. R. Soc. A Math. Phys. Eng. Sci. 223 (1923) 289–343, https://doi.org/10.1098/rsta.1923.0008.

[31] R.C. DiPrima, P.M. Eagles, B.S. Ng, The effect of radius ratio on the stability of Couette flow and Taylor vortex flow, Phys. Fluids 27 (1984) 2403, https://doi.org/10.1063/1.864544.

[32] I. ANSYS, Ansys Fluent 12.0 Theory Guide, 2009.

[33] A.-N. Spiess, N. Neumeyer, An evaluation of R2 as an inadequate measure for nonlinear models in pharmacological and biochemical research: a Monte Carlo approach, BMC Pharmacol. 10 (2010) 6, https://doi.org/10.1186/1471-2210-10-6.

[34] M. Kosaka, S. Minowa, Mass-transfer from solid metal cylinder into liquid metal, Tetsu-To-Hagane 52 (1966) 1748–1762, https://doi.org/10.2355/tetsutohagane1955.52.12_1748.

[35] F. Tachibana, S. Fukui, H. Mitsumura, Heat transfer in an annulus with an inner rotating cylinder, Trans. Japan Soc. Mech. Eng. 25 (1959) 788–792, https://doi.org/10.1299/kikai1938.25.788.

[36] A.R. Cooper, The effect of the moving boundary on molecular diffusion controlled dissolution or growth kinetics, Trans. Faraday Soc. 58 (1962) 2468–2472, https://doi.org/10.1039/tf9625802468.

7.3 Publication III

Application of an improved testing device for the study of alumina dissolution in silicate slag

Burhanuddin, Jerónimo Guarco, Harald Harmuth, Sandra Vollmann

Journal of the European Ceramic Society 42 (2022) 3652–3659

Contents lists available at ScienceDirect

Journal of the European Ceramic Society

journal homepage: www.elsevier.com/locate/jeurceramsoc

Application of an improved testing device for the study of alumina dissolution in silicate slag

Burhanuddin *, Jerónimo Guarco, Harald Harmuth, Sandra Vollmann

Montanuniversität Leoben, Peter-Tunner Straße 5, 8700 Leoben, Austria

ARTICLE INFO

Keywords:
Dissolution
Mass transfer
Diffusivity
Finger test

ABSTRACT

This study entailed a dissolution study of alumina fine ceramics in a CaO–Al_2O_3–SiO_2–MgO silicate slag system with a CaO/SiO_2 weight ratio of 0.65. Finger-test experiments with several corrosion steps were carried out in a contemporary continuous wear testing device at 1450, 1500, and 1550 °C with 200 rpm. The corroded sample profiles were measured using a high-resolution laser scanner, and the processed measurement data were used to extract the dissolution parameters (i.e. corroded volume, surface area, mean radius, tip radius and immersion length). The diffusivity determination method using Sherwood relations was developed for the dynamic finger-test setup. The diffusivities for all corrosion steps were determined from these dissolution parameters, and those obtained from the Sherwood relations were compared with the ones received by a simulation approach that includes deviations from the cylindrical shape. The results obtained using Sherwood relations are sufficiently accurate in several cases.

1. Introduction

The dissolution studies are conducted for lifetime assessment of refractories used in industrial vessels for high-temperature operations [1–14]. Improved refractory materials with enhanced lifetimes are desired for cost and resource efficiency, and their design necessitates an in-depth understanding and accurate quantification of the dissolution parameters. Several dynamic corrosion studies have been reported in the literature [3,15–32], and most of them are based on the post-mortem analysis yielding a wear mechanism by microstructure evaluation [21,22,32–35] but fail to determine a wear measuring quantity. In some studies [15,17,18,23–31,36,37], the dissolution parameters, such as change in dimension and sample weight, were used to quantify corrosion. The measurement techniques used in the documented studies were not accurate enough as the measurements were taken manually at few locations of the corroded sample. Kircher et al. reported a contemporary corrosion testing device with an in-situ measurement technique [38]. The superior accuracy of this device is because of a laser scanner used to measure the whole surface of the sample. A resolution of 100 μm along the length and 20 μm in the circumferential direction of a cylinder specimen can be achieved. In this study, this device has been used for the dynamic corrosion study of alumina fine ceramics in a CaO–Al_2O_3–SiO_2–MgO (CASM) silicate slag system with a CaO/SiO_2 weight ratio of 0.65. Alumina has been chosen here as it is an important refractory material for the glass and steel industries [3,20,27,28,39–45]. The dissolution of alumina in molten slag is controlled by diffusion through a boundary layer, as reported by many researchers [18,37,41,46–53]. This study aimed to determine the effective binary diffusion coefficient, which is the most important parameter to quantify the dissolution process, by applying the mass transfer equations to the corrosion experiments. Based on Cochran's equation [54], Levich introduced the famous equation for the mass transfer from a disc-shaped surface of infinite radius, submerged in a semi-infinite medium [55]. This equation provides an accurate approximation of the mass flux density for real finite geometries if the boundary layer thickness is much smaller than the disc radius. Furthermore, the mass flux density is uniform throughout the disc surface. As a result this equation can be applied to estimate the change in the length of a cylindrical sample which was reported by Cooper and Kingery [18]. While the Levich equation is derived for the disc surface, Eisenberg et al. [56] proposed an equation for the ionic mass flux from the mantle of a cylindrical sample. Kosaka and Minowa [57] introduced the Sherwood relations for the dissolution of cylindrical shaped metals into liquid metals. Tachibana and Fukui [58] reported equations for the heat transfer through the annular region. These equations, after necessary modifications, can be implemented for the dissolution of the solid in a melt. Um et al. [24] used Eisenberg's

* Corresponding author.
E-mail address: burhanuddin.burhanuddin@unileoben.ac.at (Burhanuddin).

https://doi.org/10.1016/j.jeurceramsoc.2022.02.056
Received 25 January 2022; Accepted 28 February 2022
Available online 2 March 2022

equation [56] to determine the mass transfer coefficient of MgO in ferromanganese slags.

Guarco et al. [59] reported a simulated method to determine the diffusivities from rotating finger experiments of dense ceramic materials applicable even for large Schmidt numbers, which exist also for the case of interest in this study. This method also considers the advection that occurs in an orthogonal direction to the solid/melt interface, characteristic of the dissolution process, and furthermore the effect of Stefan's velocity on the boundary layer thickness. All these considerations make this method more appropriate for the dissolution investigations than other extant methodologies in the literature, where these effects are commonly neglected. The device reported by Kircher et al. [38] was used for the experiment. The effective binary diffusivity is determined via two different approaches: In the first approach the experimental mass flux density is equalized with the average mass flux density calculated by simulation. For the second method, curve fitting along the end worn profile with a simulated profile is applied. The simulated results were compared with those of different equations reported in the literature and were found to be in agreement with the results of the modified Tachibana equation [58]. This agreement may vary in other experiments as the results depend on the shape of the corroded sample. Though the method reported by Guarco et al. produces more reliable results than other reported equations, its application requires much effort. Therefore, the present work aimed to compare this method with a simpler one and examined the advantages of the testing device presented by Kircher et al. [38] to quantify the alumina diffusivity. As a result, improved effective binary diffusivities are expected owing to more accurate measurements and evaluation methods. Further, the availability of accurate but yet simpler evaluation methods should be clarified. For that purpose, dissolution experiments were carried out at 1450, 1500, and 1550 °C with nine, eight, and six corrosion steps, respectively. The diffusivity was determined for all the corrosion steps using the modified Tachibana equation, and the diffusivity of one step at each temperature was compared with the results obtained by the application of the method reported by Guarco et al. [59]. Further, the Arrhenius plot of the diffusivities was checked as a test for plausibility.

2. Materials and methods

2.1. Materials

In this study, alumina fine ceramics (Ants Ceramics Private Limited, India) with an alumina content of 99.7 wt% and a bulk density of 3.8706 g/cc have been investigated. The alumina cylinders had a 20 mm diameter and 110 mm length. All samples have an axial drill of 5 mm diameter and 32 mm depth, and a side drill of 3.5 mm diameter to fix the cylinder with the rotor shaft.

The silicate slag was prepared using decarburized $CaCO_3$, alumina powder, quartz powder, and MgO powder (S3 Handel und Dienstleistungen UG). Table 1 shows the slag properties, where η, ρ, and T_L are dynamic viscosity, density, and liquidus temperature, respectively. The viscosities of the original slag and alumina saturated slag, and the saturation limits of alumina in this slag at different temperatures are represented in Fig. 1. The viscosities, liquidus temperature, and saturation limits were calculated using FactSage 7.2. The density of the slag was calculated according to Xin et al. [60]. Fig. 1 shows that viscosity is higher for the saturated slag, and the viscosity increase at a lower temperature is larger than that at a higher temperature.

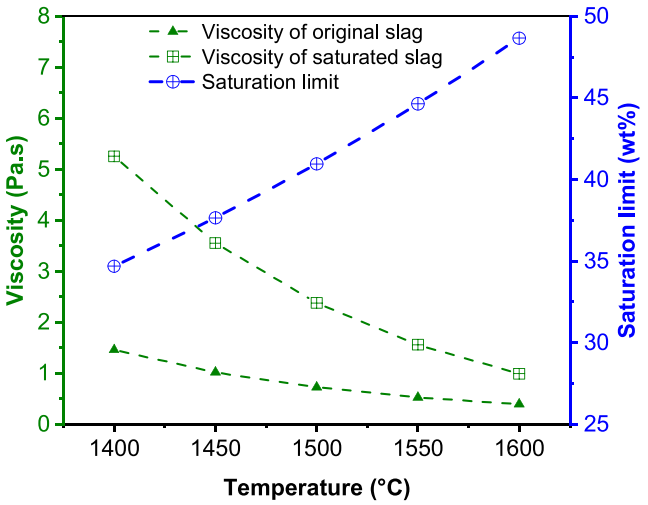

Fig. 1. Viscosities of slag and saturation limits of Al_2O_3 over temperature.

2.2. Experiment

In the present work, dynamic corrosion experiments were carried out using a continuous wear testing device (CWTD) with 200 rotations per minute (rpm) at 1450 °C, 1500 °C, and 1550 °C. The detailed description of the CWTD and measurement technique can be found in the publication reported by Kircher et al. [38]. For each experiment, 580 g of slag was filled in a platinum-10% rhodium (Pt-Rh10) crucible of 65 mm inner diameter and 100 mm height. Initially, the clearance between the crucible bottom and sample tip was set to 20 mm which continuously increased with the dissolution of the sample. The heating and cooling rate of the furnace incorporating the slag and alumina sample were defined to 5 °C per minute. The dissolution times per corrosion step at 1450 °C, 1500 °C, and 1550 °C were set to 135, 105, and 90 min, respectively. After each corrosion step the corroded sample rested above the crucible for 30 min to allow the slag to drop down from the sample surface, and then the laser device scanned the whole sample surface. The corrosion step and sample scan cycle were repeated at an isothermal experimental temperature until the last step specified or until the test was terminated because of reasonably small sample diameter.

2.3. Continuous wear curve evaluation

The laser device scans the sample, rotating at 2 rpm, with a profile scan rate of 100 s^{-1} to produce 3000 profiles for one complete rotation. All the profiles were averaged after some preprocessing to get a unique, axisymmetric, and representative continuous wear (CW) curve. Kircher et al. [38] has reported the detailed description of profile processing. The sample length and radius can easily be measured from this CW curve. The dissolution parameters (corroded volume, surface area, mean radius, tip radius, and immersion length) can be extracted from the CW curve to determine the mass flux density and diffusivity. The intersection point of the initial curve of the uncorroded sample and the actual CW curve defines the onset for the corroded part. The immersion length is defined from the sample tip to the onset of the corroded part. The remaining volume and mantle surface area were determined by integration along the immersion length. The area of the disc shape tip was added to get the total surface area. The mean radius along the immersion length was used as the representative cylinder radius for the diffusivity

Table 1
Slag properties.

Slag	CaO [wt%]	Al_2O_3 [wt%]	SiO_2 [wt%]	MgO [wt%]	$\eta_{1450\ °C}$ [Pa s]	$\eta_{1500\ °C}$ [Pa s]	$\eta_{1550\ °C}$ [Pa s]	$\rho_{1550\ °C}$ [kg/m^3]	T_L [°C]
CASM slag, C/S = 0.65	32.42	11.16	49.56	6.86	1.02	0.73	0.53	2579	1265

determination and is larger than the tip radius. The tip radius was used to calculate the mass flux from the bottom of the sample by the Levich equation. All the corrosion parameters required for the diffusivity calculations tend to change with the dissolution time within the corrosion step, so it is wise to evaluate the diffusivity at the middle of the corrosion step which will be representative for that particular step. The parameters are defined in Table 2. The surface is scanned before dipping the sample into the slag, thereby yielding the initial profile at t_0. The profiles are measured at time steps t_i, $1 \le i \le m$, where m is the number of laser scans performed in addition to the first scan at t_0.

2.4. Diffusivity determination

The Sherwood correlations are frequently used to calculate the mass transfer coefficient. The knowledge of mass flux aids in determining the diffusivity from the mass transfer equations. In addition to the already mentioned procedure by Guarco et al. [59], the diffusivity has been calculated from the total mass flux density using the modified Sherwood relation (translated from Nusselt correlation reported by Tachibana and Fukui [58]) for the mantle and the Sherwood relation (reported by Levich [55]) for the bottom of the sample. The determination procedure has been derived as follows:

Eq. (1) represents the diffusive mass flux density including the convective flow, and considers the influence of the Stefan flow on the fluid flow field.

Table 2
Definition of parameters required to evaluate diffusivity for the interval (t_i,t_{i-1}).

Quantity	Measured at	Evaluation at
	t_i	$(t_i + t_{i-1})/2$
Refractory volume	V_i^r	$V^r_{i-\frac{1}{2}} = \frac{V_i^r + V_{i-1}^r}{2}$
Volume loss relative to initial volume	$\Delta V_i^r = V_0^r - V_i^r$	$\Delta V^r_{i-\frac{1}{2}} = V_0^r - V^r_{i-\frac{1}{2}}$
Mass loss relative to initial mass	$\Delta m_i^r = \rho^r \cdot \Delta V_i^r$	$\Delta m^r_{i-\frac{1}{2}} = \rho^r \cdot \Delta V^r_{i-\frac{1}{2}}$
Bulk concentration of species k in slag		$c^s_{0,k,i-\frac{1}{2}} = \frac{c^s_{0,k,0} V_0^s + \Delta m^r_{i-\frac{1}{2}} w_k^r}{V^s_{i-\frac{1}{2}}} = \frac{c^s_{0,k,0} V_0^s + \Delta m^r_{i-\frac{1}{2}} w_k^r}{m_0^s + \Delta m^r_{i-\frac{1}{2}}} \rho^s; \quad w^s_{0,k,i-\frac{1}{2}} = \frac{c^s_{0,k,0} V_0^s + \Delta m^r_{i-\frac{1}{2}} w_k^r}{m_0^s + \Delta m^r_{i-\frac{1}{2}}}$
Dimension less concentration difference		$B_{i-\frac{1}{2}} = \frac{w_s^s - w^s_{0,i-\frac{1}{2}}}{1 - w_s^s}$
Viscosity		$\eta = \eta\left(w_{0,k,i-\frac{1}{2}}\right)$
Immersion specimen length	l_i	$l_{i-\frac{1}{2}} = \frac{l_i + l_{i-1}}{2}$
Specimen effective radius	$R_{1,i}$	$R_{1,i-\frac{1}{2}} = \sqrt{\frac{V_{i-\frac{1}{2}}}{\pi l_{i-\frac{1}{2}}}}$
Submerged surface area	A_i	$A_{i-\frac{1}{2}} = \frac{A_i + A_{i-1}}{2}$
Mass flux density		$j_{i-\frac{1}{2}} = \frac{\Delta m_i^r - \Delta m_{i-1}^r}{A_{i-\frac{1}{2}} (t_i - t_{i-1})}$

$$j = X \frac{D}{L} \frac{1}{1 - w_s} Sh_0 \cdot \Delta c \tag{1}$$

Here, j is the mass flux density, D is the effective binary diffusivity, L is the characteristic length, w_s is the mass fraction of the dissolving species in the saturated slag, Sh is the Sherwood number, and Δc is the concentration difference. The quantities used in Eq. (1) have been defined in Eqs. (2)–(5).

$$Sh_{(0)} = \frac{\beta_{(0)} L}{D} = Sh_{(0)}(Re, Sc, \Gamma) \tag{2}$$

$$Sh_0 = Sh(B = 0); \quad \beta = \frac{D}{\delta}; \quad \beta_0 = \beta(B = 0) \tag{3}$$

$$B = \frac{w_s - w_0}{1 - w_s} \tag{4}$$

$$X = X(B, Sc) = \frac{Sh}{Sh_0} \tag{5}$$

Here, w_0 is the mass fraction of the dissolving species in the slag bulk, Re is the Reynolds number, Sc is the Schmidt number, Γ is the ratio of the gap width of the annuli to the cylinder radius, δ is the effective boundary layer thickness, and β is the mass transfer coefficient.

The quantity X can be approximated by a linear expansion in B:

$$X = \frac{Sh}{Sh(B = 0)} = X \approx \frac{1}{1 + 0.566B} \tag{6}$$

Tachibana et al. reported different empirical equations for heat transfer in different setups [58]. The heat transfer in the annuli with a rotating inner cylinder is similar to that in the dynamic finger test for the dissolution with the exception of the bottom gap. Eq. (7) is the Sherwood relation transformed from the Nusselt relation for the aforesaid setup.

$$Sh = \frac{\beta \cdot (R_2 - R_1)}{D} = 0.21 \cdot \left(Ta^2 \cdot Sc\right)^{\frac{1}{4}} = 0.21 \cdot Re^{\frac{1}{2}} \cdot Sc^{\frac{1}{4}} \cdot \left(\frac{R_2 - R_1}{R_1}\right)^{\frac{1}{4}}; Ta \le 10^4 \tag{7}$$

$$\text{with} \quad Ta = \frac{\omega \cdot R_1^{\frac{1}{2}} \cdot (R_2 - R_1)^{\frac{3}{2}}}{\nu} \quad \text{and} \quad Re = \frac{\omega \cdot R_1 \cdot (R_2 - R_1)}{\nu}$$

Here, R_1 is the mean cylinder radius, R_2 is the crucible radius, Ta is the Taylor number, ω is the angular velocity of the rotating cylinder, and ν is the kinematic viscosity of the melt.

According to Guarco et al.[59], the change in the exponent value of the Sc number from ¼ to $^1/_3$ exhibited better results for the corroded sample. After this modification, the Sh number in this equation is in good agreement with the simulation results for the CWTD dissolution experiment. Eq. (8) represents the modified Sherwood relation for the mantle of the cylindrical sample.

$$Sh_{0,m} = \frac{\beta_0 \cdot (R_2 - R_1)}{D} = 0.21 \cdot Re^{\frac{1}{2}} \cdot Sc^{\frac{1}{3}} \cdot \left(\frac{R_2 - R_1}{R_1}\right)^{\frac{1}{4}}; \quad Re = \frac{\omega \cdot R_1 \cdot (R_2 - R_1)}{\nu} \tag{8}$$

Eq. (9) represents the Sherwood relation for the bottom of a rotating cylinder in a finger-test setup according to Levich [55].

$$Sh_{0,b} = \frac{\beta_0 \cdot R_t}{D} = 0.62 \cdot Re^{\frac{1}{2}} \cdot Sc^{\frac{1}{3}}; \quad Re = \frac{\omega \cdot R_t^2}{\nu} \tag{9}$$

Here, R_t is the tip radius.

According to Eq. (1), the total mass flux can be represented as Eqs. (10) and (11) for the submerged mantle and cylinder bottom, respectively.

$$j_{tot} \cdot A_{tot} = j_m \cdot A_m + j_b \cdot A_b; \quad A_m = 2R_1 \pi l; \; A_b = R_t^2 \pi; \; A_{tot} = A_m + A_b \tag{10}$$

$$j \cdot A_{tot} = X \cdot D \cdot \left\{ A_m \cdot \frac{Sh_{0,m}}{R_2 - R_1} + A_b \cdot \frac{Sh_{0,b}}{R_t} \right\} \rho_s \cdot B \tag{11}$$

Here, j_{tot}, j_m, j_b and A_{tot}, A_m, A_b are the mass flux densities and surface areas of the total surface, mantle, and bottom of the cylinder, respectively, l is the immersion length, and ρ_s is the density of the slag. On combining Eqs. (6), (8), (9), and (11), we can get Eq. (12).

$$j = \frac{1}{1 + 0.566 \cdot B} \cdot \frac{1}{2l \cdot R_1 + R_t^2} \cdot \frac{\omega^{\frac{1}{2}} \cdot \rho_s \cdot B}{\nu^{\frac{1}{6}}} \cdot D^{\frac{2}{3}} \cdot \left\{ 0.42 \cdot \frac{l \cdot R_1^{\frac{5}{4}}}{(R_2 - R_1)^{\frac{1}{4}}} + 0.62 \cdot R_t^2 \right\} \tag{12}$$

After rearranging Eq. (12), the effective binary diffusivity ($D_{i,i+1}$) can be determined for each corrosion step using Eq. (13). In one dissolution experiment, there are several data of the in-situ measured profiles. The average of the diffusivities of several corrosion steps provides the representative diffusivity ($D_{0,i}$).

$$D_{i,i+1} = \left[\frac{j \cdot (1 + 0.566 \cdot B) \cdot \left(2l \cdot R_1 + R_t^2\right) \cdot (R_2 - R_1)^{\frac{1}{4}} \cdot \nu^{\frac{1}{6}}}{\omega^{\frac{1}{2}} \cdot \rho_s \cdot B \cdot \left\{ 0.42 \cdot l \cdot R_1^{\frac{5}{4}} + 0.62 \cdot R_t^2 \cdot (R_2 - R_1)^{\frac{1}{4}} \right\}} \right]^{\frac{3}{2}} \tag{13}$$

3. Results and discussion

3.1. CW curves

After each corrosion step, one representative CW curve was generated by the averaging of all the profiles along the circumference. This procedure has two major advantages. Firstly, the individual profiles of the corroded sample may be slightly inclined with a positive or negative angle to the theoretical axis of rotation due to the nonconcentric rotation of the sample during the laser measurement, and this inclination can be eliminated. Secondly, the corroded sample is not axisymmetric, which makes the dimensional analysis equivocal; the CW curve offers an equivalent axially-symmetric shape. Fig. 2 shows the CW curves for the dissolution experiments at 1450 °C, 1500 °C, and 1550 °C. Kircher et al. [38] have reported the CW curves at 1550 °C as an example without further evaluation of the dissolution parameters. The uncorroded parts of all the CW curves coincide with each other and also with the CW curve of the virgin sample. The onset of the corroded part shifted towards the uncorroded part with time because of an increase in the slag quantity with dissolution. The corroded parts of all the CW curves are distinguished and do not coincide. The corroded sample radius and length decreased with the dissolution time, and for a particular dissolution time, the decrease was greater with increasing temperature. For the first corrosion step, the dissolution at the bottom edge was comparatively higher. Fig. 3 shows the virgin and corroded samples. The CW curves for the last corrosion steps depict a well-defined corroded sample shape. There was no Marangoni groove formation at the three phase boundary (slag/refractory/atmosphere), and this indicates that the experimental Reynold's number is sufficiently high to suppress the Marangoni convection.

3.2. Dissolution parameters

The dissolution parameters, namely corroded volume, surface area, mean radius, tip radius, and immersion length were extracted from the CW curves. As these parameters were determined from the CW curves, they are expected to be more accurate than the manual measurements of the post-mortem analysis. The change in the sample length, mean corroded radius, volume, and mass over dissolution time are represented in Fig. 4 to understand the effect of temperature on the dissolution behavior of alumina in the CASM slag being studied. All these parameters increased in value with the rising experimental temperature. The average rate of change in the mean corroded radius, volume, and mass

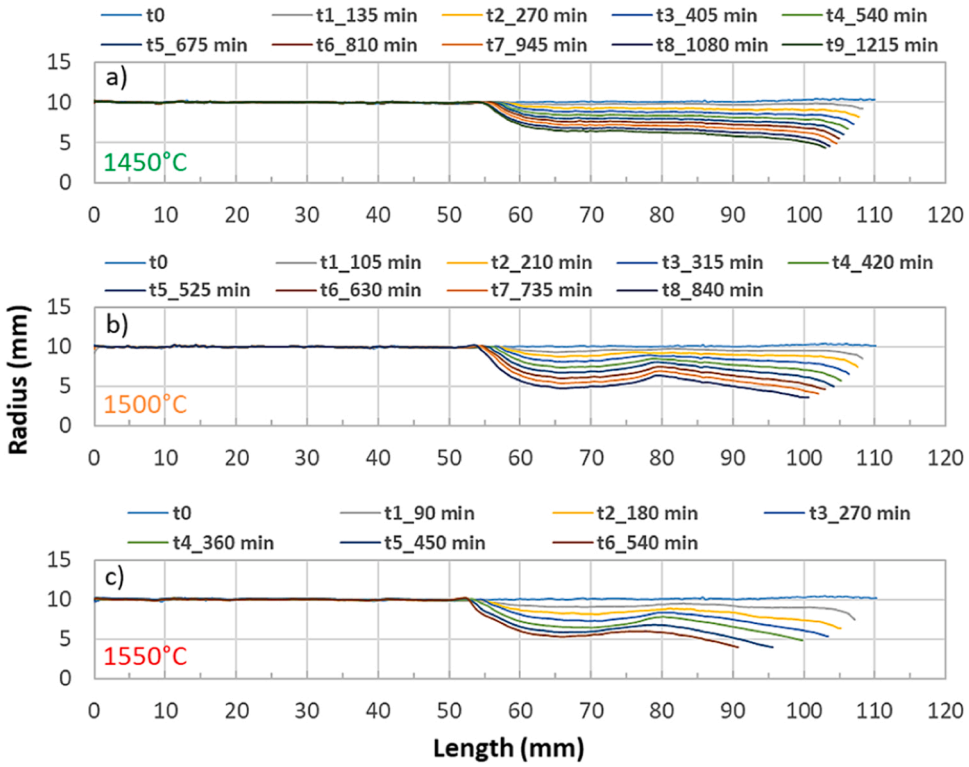

Fig. 2. CW curves at different dissolution time steps; a) at 1450 °C, b) at 1500 °C, and c) at 1550 °C. (For interpretation of the references to colour in this figure legend, the reader is referred to the Web version of this article.)

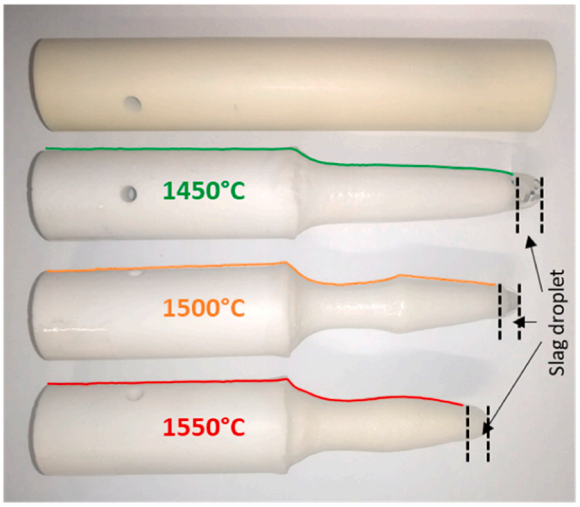

Fig. 3. Virgin and corroded samples with CW curves of last steps inserted.

increased 1.6–1.7 times with an increase in temperature from 1450 °C to 1500 °C and 1500 °C to 1550 °C. The average rate of change in the sample length increased 3.27 times with an increase in temperature from 1500 °C to 1550 °C, contrary to the 1.83 times increase for the temperature rise from 1450 °C to 1500 °C. The higher average rate of change in length at 1550 °C may have occurred because of the faster dissolution of the relatively thinner sample (compared to sample thickness at lower temperatures), especially at the ending steps in the low viscosity slag. A slightly decreasing slope or almost linear trend of the dissolution parameters indicates a quasi-steady dissolution.

3.3. Diffusivity

The diffusivities for all the steps were calculated with Eq. (13) using the dissolution parameters extracted from the CW curves and the parameters tabulated in Table 3. The mean sample radius, tip radius, and immersion length continuously decreased with the dissolution time. whereas the bulk concentration of alumina and slag viscosity increased with the alumina dissolution. Fig. 5 represents the diffusivities ($D_{i,i+1}$ and $D_{0,i}$) for all the corrosion steps at three experimental temperatures. The diffusivity increased with increasing temperature. The Arrhenius plot was produced with the diffusivities of the corresponding corrosion steps where a similar mass loss, relative to the initial mass (m1: 23.06–26.10 g, m2: 34.14–36.57 g, and m3: 41.55–43.34 g), was observed at different temperatures. The diffusivities received are functions of temperature and slag composition, which changes during dissolution. For the Arrhenius plot, the diffusivities were converted to those for the virgin slag composition using the Stokes-Einstein relation that defines the product of diffusivity and viscosity to be constant. This conversion makes the Arrhenius behavior of diffusivity a function of temperature only, else the alumina content of slag would have been another parameter. Fig. 6 represents the Arrhenius plot which shows the linear tendency, thereby confirming the plausibility of diffusivities. The linear fit is better when the mass losses of the corrosion steps are comparable. The activation energy of diffusion for the m1, m2, and m3 cases are 288.1, 262.0, and 258.6 kJ/mol, respectively.

Table 4 compares the diffusivities determined by Eq. (13) and obtained from the simulation according to Guarco et al. [59]. The second, thirds and second steps of 1450 °C, 1500 °C, and 1550 °C experiments, respectively, were chosen arbitrarily for this comparison. Diffusivities obtained from both methods show a good agreement for the chosen corrosion steps.

4. Conclusions

In conclusion, the alumina diffusivity was successfully quantified from the total mass flux density using Sherwood relations. Therefore dissolution experiments of alumina fine ceramics in molten CASM slag were carried out in CWTD with in-situ measurements. The dissolution parameters were extracted from the CW curves which include the measurement from the whole corroded surface. This enhances the

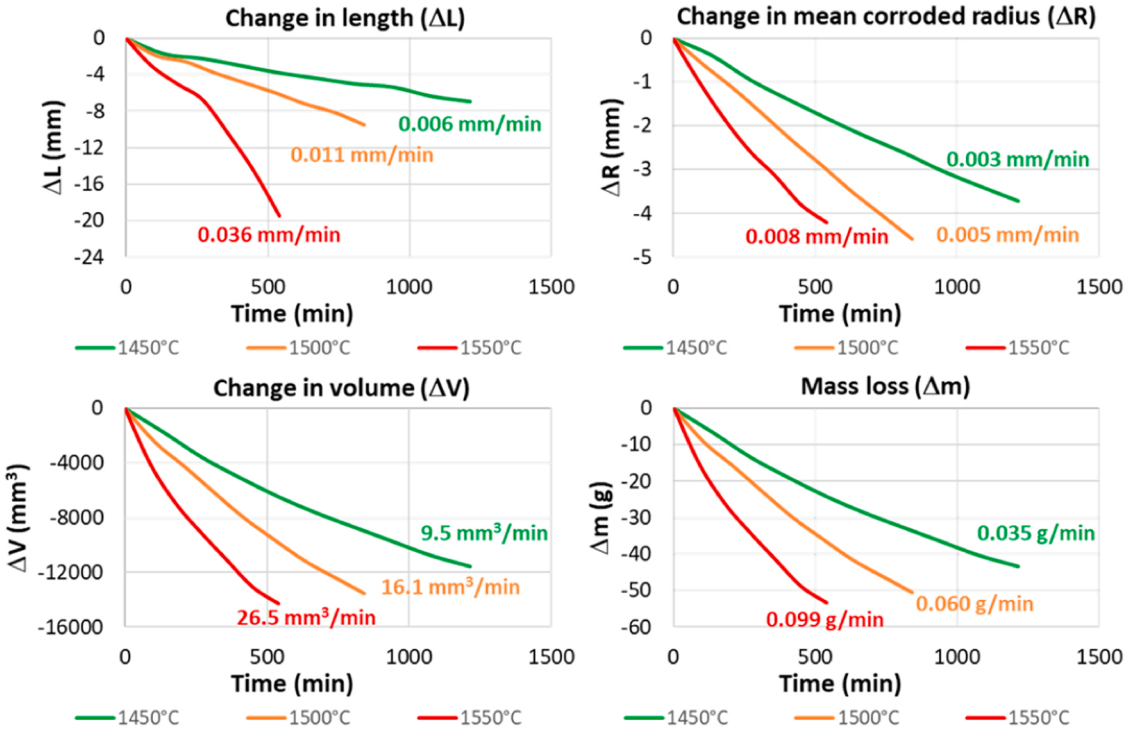

Fig. 4. Dissolution parameters over time at different experimental temperatures. The numbers inserted give the mean value over the total dissolution time. (For interpretation of the references to colour in this figure legend, the reader is referred to the Web version of this article.)

Table 3
Dissolution parameters used for diffusivity calculation.

Temperature (°C)	Step	Mean sample radius, $R_{1,i-1/2}$ (m)	Tip radius, $R_{t,i-1/2}$ (m)	Bulk concentration, $w_{0,i-1/2}$ (%/100)	Viscosity, $\eta_{i-1/2}$ (Pa s)	Immersion length, $l_{i-1/2}$ (m)	Mass flux density, $j_{i-1/2}$ (kg/m^2 s)
1450	$t_{1/2}$	0.00997	0.0097874	0.11654	1.0448	0.050903	0.000229709
	$t_{3/2}$	0.00949	0.0087264	0.12656	1.0949	0.049998	0.000263853
	$t_{5/2}$	0.00899	0.0077656	0.13573	1.1422	0.049848	0.000232004
	$t_{7/2}$	0.00854	0.007016	0.14353	1.1863	0.049736	0.000228111
	$t_{9/2}$	0.00813	0.0063779	0.15038	1.2263	0.049603	0.000208675
	$t_{11/2}$	0.00774	0.0057755	0.15625	1.2603	0.049346	0.000195567
	$t_{13/2}$	0.00734	0.0052053	0.16164	1.2958	0.049174	0.000206012
	$t_{15/2}$	0.00695	0.0047347	0.16689	1.3302	0.049042	0.000215812
	$t_{17/2}$	0.00660	0.0044655	0.17142	1.3585	0.048686	0.000175272
1500	$t_{1/2}$	0.00984	0.0093310	0.11859	0.7495	0.051863	0.000419619
	$t_{3/2}$	0.00927	0.0079871	0.13043	0.7885	0.050737	0.000337636
	$t_{5/2}$	0.00871	0.0070036	0.14048	0.8227	0.050007	0.000393276
	$t_{7/2}$	0.00810	0.0061416	0.15046	0.8602	0.049265	0.000420668
	$t_{9/2}$	0.00751	0.0053674	0.15934	0.8949	0.048863	0.000391632
	$t_{11/2}$	0.00692	0.0048332	0.16719	0.9275	0.048323	0.000417434
	$t_{13/2}$	0.00636	0.0043644	0.17400	0.9565	0.047708	0.000369672
	$t_{15/2}$	0.00582	0.0038412	0.17990	0.9827	0.047013	0.000406564
1550	$t_{1/2}$	0.00967	0.0088281	0.12317	0.5533	0.054858	0.000791799
	$t_{3/2}$	0.00875	0.0069313	0.14222	0.5969	0.051981	0.000666008
	$t_{5/2}$	0.00795	0.0058652	0.15546	0.6297	0.049671	0.000578386
	$t_{7/2}$	0.00729	0.0050890	0.16602	0.6576	0.047435	0.000613556
	$t_{9/2}$	0.00669	0.0043837	0.17584	0.6850	0.044512	0.000709582
	$t_{11/2}$	0.00615	0.0039540	0.18354	0.7081	0.040365	0.000523108

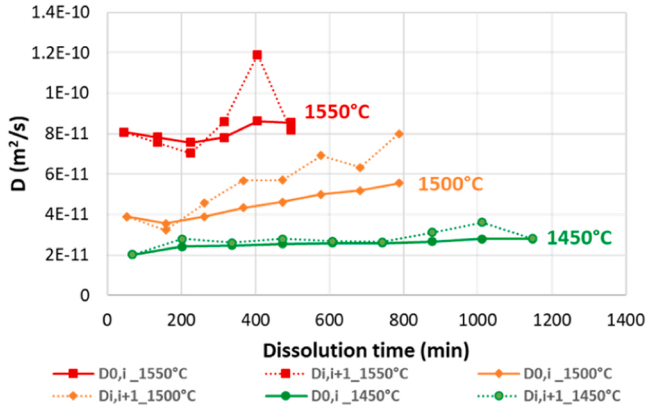

Fig. 5. Diffusivities for all corrosion steps at three experimental temperatures.

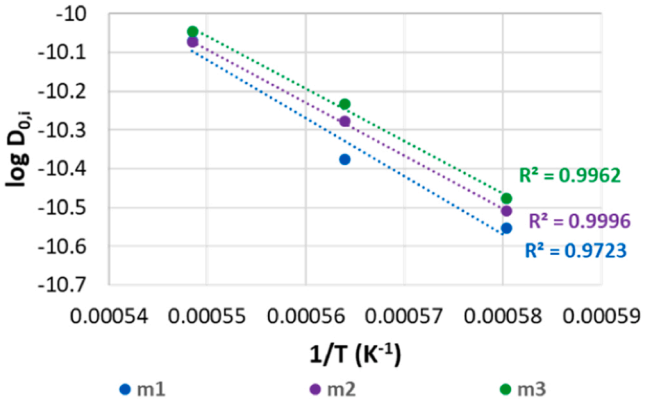

Fig. 6. Arrhenius plot of diffusivities. (For interpretation of the references to colour in this figure legend, the reader is referred to the Web version of this article.)

accuracy and reliability of the results. A defined experimental rotational speed was sufficient to suppress the Marangoni convection at the three phase boundary allowing the use of the presented Sherwood relation and of a method reported by Guarco et al. [59]. A slightly decreasing slope or almost linear trend of dissolution parameters indicates a quasi-steady dissolution. The rates of change of the mean corroded radius, volume, and mass also show a linear trend with temperature in the experimental temperature range. Dissolution rates and determined diffusivities increased with increasing temperature, as expected. Arrhenius plot shows a linear tendency which confirms the plausibility of diffusivities. The diffusivities obtained from the mass transfer equation and simulation show a good agreement. Although the diffusivity from the simulation is more reliable as it considers the flow field around the actual sample geometry of that particular step, the diffusivity can be reliably determined using the given equation with less effort.

Hence, using the quoted equation with the accurate measurement

Table 4
Comparison of diffusivities obtained from two methods.

Experimental step	Diffusivity using Eq. (13) (D_i), m^2/s	Diffusivity from simulation, m^2/s	Error (%), relative to Eq. (13)
$D_{1450,2}$	2.80E-11	2.09E-11	25.41
$D_{1500,3}$	4.56E-11	4.74E-11	3.99
$D_{1550,2}$	7.56E-11	7.31E-11	3.36

results obtained from the CWTD yield improved the effective binary diffusivities as shown for alumina in the CASM slag in this study.

Declaration of Competing Interest

The authors declare that they have no known competing financial interests or personal relationships that could have appeared to influence the work reported in this paper.

Acknowledgements

The authors gratefully acknowledge the financial support under the scope of the COMET program within the K2 Center "Integrated Computational Material, Process and Product Engineering (IC-MPPE)" (Project No. 859480). This program is supported by the Austrian Federal Ministries for Transport, Innovation and Technology (BMVIT) and for Digital and Economic Affairs (BMDW), represented by the Austrian research funding association (FFG), and the Federal States of Styria, Upper Austria and Tyrol. Further guidance of Volkmar Kircher during the experimental procedures is thankfully acknowledged.

References

[1] W.E. Lee, S. Zhang, Melt corrosion of oxide and oxide–carbon refractories, Int. Mater. Rev. 44 (1999) 77–104, https://doi.org/10.1179/095066099101528234.
[2] H. Harmuth, S. Vollmann, Refractory corrosion by dissolution in slags – challenges and trends of present fundamental research, Iron Steel Rev. 58 (2014) 157–170.
[3] Z. Wang, T. Maotsela, P.M. Toperesu, G.M. Kale, J. Daji, D. Parkinson, Dynamic and static corrosion of alpha-alumina bonded refractory in contact with molten soda–lime–silica (SLS) glass, Ceram. Int. 45 (2019) 725–732, https://doi.org/10.1016/j.ceramint.2018.09.235.
[4] S. Jansson. A Study on the Influence of Steel, Slag or Gas on Refractory Reactions (Doctoral thesis), Applied Process Metallurgy, KTH, Stockholm, 2008.
[5] H.Y. Tang, G.H. Wu, Y. Wang, J.S. Li, P. Lan, J.Q. Zhang, Comparative evaluation investigation of slag corrosion on Al_2O_3 and MgO-Al_2O_3 refractories via experiments and thermodynamic simulations, Ceram. Int. 43 (2017) 16502–16511, https://doi.org/10.1016/j.ceramint.2017.09.034.
[6] M.K. Cho, M.A. Van Ende, T.H. Eun, I.H. Jung, Investigation of slag-refractory interactions for the Ruhrstahl Heraeus (RH) vacuum degassing process in steelmaking, J. Eur. Ceram. Soc. 32 (2012) 1503–1517, https://doi.org/10.1016/j.jeurceramsoc.2012.01.005.
[7] C. Reynaert, E. Śniezek, J. Szczerba, Corrosion tests for refractory materials intended for the steel industry – a review, Ceram. Silik. 64 (2020) 278–288, https://doi.org/10.13168/cs.2020.0017.
[8] J.H. Park, J.G. Park, D.J. Min, Y.E. Lee, Y.-B. Kang, In situ observation of the dissolution phenomena of SiC particle in CaO–SiO_2–MnO slag, J. Eur. Ceram. Soc. 30 (2010) 3181–3186, https://doi.org/10.1016/j.jeurceramsoc.2010.07.020.
[9] J. Liu, M. Guo, P.T. Jones, F. Verhaeghe, B. Blanpain, P. Wollants, In situ observation of the direct and indirect dissolution of MgO particles in CaO-Al_2O_3-SiO_2-based slags, J. Eur. Ceram. Soc. 27 (2007) 1961–1972, https://doi.org/10.1016/j.jeurceramsoc.2006.05.107.
[10] F. Cirilli, et al., Corrosion mechanisms of zirconia/carbon based refractory materials by slag in presence of steel, La Metall. Ital. 100 (2008) 43–50.
[11] C. Baudín, E. Criado, J.J. Bakali, P. Pena, Dynamic corrosion of Al_2O_3–ZrO_2–SiO_2 and Cr_2O_3-containing refractories by molten frits. Part I: Macroscopic analysis, J. Eur. Ceram. Soc. 31 (2011) 697–703, https://doi.org/10.1016/j.jeurceramsoc.2010.11.023.
[12] S. Jansson, V. Brabie, L. Bohlin, Corrosion mechanism and kinetic behaviour of refractory materials in contact with CaO–Al_2O_3–MgO –SiO_2 slags, in: Proceedings of the Int. Conf. on Molten Slags Fluxes and Salts VII, 2004, pp. 341–8.
[13] M.A.L. Braulio, A.G.T. Martinez, A.P. Luz, C. Liebske, V.C. Pandolfelli, Basic slag attack of spinel-containing refractory castables, Ceram. Int. 37 (2011) 1935–1945, https://doi.org/10.1016/j.ceramint.2011.02.007.
[14] K. Goto, B.B. Argent, W.E. Lee, Corrosion of MgO-$MgAl_2O_4$ spinel refractory bricks by calcium aluminosilicate slag, J. Am. Ceram. Soc. 80 (2005) 461–471, https://doi.org/10.1111/j.1151-2916.1997.tb02852.x.
[15] S. Amini, M. Brungs, S. Jahanshahi, O. Ostrovski, Effects of additives and temperature on the dissolution rate and diffusivity of lime in Al_2O_3-CaO-SiO_2 based slags, Metall. Mater. Trans. B 37b (2006) 773–780.
[16] H. Wang, R. Caballero, D. Sichen, Dissolution of MgO based refractories in CaO-Al_2O_3-MgO-SiO_2 slag, J. Eur. Ceram. Soc. 38 (2018) 789–797, https://doi.org/10.1016/j.jeurceramsoc.2017.09.030.
[17] T. Deng, B. Glaser, D. Sichen, Experimental design for the mechanism study of lime dissolution in liquid slag, Steel Res. Int. 83 (2012) 259–268, https://doi.org/10.1002/srin.201100258.
[18] A.R. Cooper, W.D. Kingery, Dissolution in ceramic systems: I, Molecular diffusion, natural convection, and forced convection studies of sapphire dissolution in calcium aluminum silicate, J. Am. Ceram. Soc. 47 (1964) 37–43, https://doi.org/10.1111/j.1151-2916.1964.tb14638.x.
[19] J. Goriupp, A. Rief, J. Schenk, Quantifying of a dynamic refractory wear test setup for MgO-C products, Berg. Huettenmaenn Mon. 157 (2012) 340–344, https://doi.org/10.1007/s00501-012-0028-5.
[20] Y. Liang, A. Huang, X. Zhu, H. Gu, L. Fu, Dynamic slag/refractory interaction of lightweight Al_2O_3–MgO castable for refining ladle, Ceram. Int. 41 (2015) 8149–8154, https://doi.org/10.1016/j.ceramint.2015.03.026.
[21] M. Guo, P.T. Jones, S. Parada, E. Boydens, J.V. Dyck, B. Blanpain, P. Wollants, Degradation mechanisms of magnesia-chromite refractories by high-alumina stainless steel slags under vacuum conditions, J. Eur. Ceram. Soc. 26 (2006) 3831–3843, https://doi.org/10.1016/j.jeurceramsoc.2005.12.025.
[22] H. Um, K. Lee, K.-Y. Kim, G. Shin, Y. Chung, Effect of carbon content of ferromanganese alloy on corrosion behaviour of MgO–C refractory, Ironmak. Steelmak. 41 (2014) 31–37, https://doi.org/10.1179/1743281212Y.0000000098.
[23] A.-H. Bui, S.-C. Park, I.-S. Chung, H.-G. Lee, Dissolution behavior of zirconia-refractories during continuous casting of steel, Met. Mater. Int. 12 (2006) 435–440, https://doi.org/10.1007/BF03027711.
[24] H. Um, K. Lee, J. Choi, Y. Chung, Corrosion behavior of MgO–C refractory in ferromanganese slags, ISIJ Int. 52 (2012) 62–67, https://doi.org/10.2355/isijinternational.52.62.
[25] S. Jansson, V. Brabie, P. Jönsson, Corrosion mechanism and kinetic behaviour of MgO–C refractory material in contact with CaO-Al_2O_3-SiO_2-MgO slag, Scand. J. Metall. 34 (2005) 283–292, https://doi.org/10.1111/j.1600-0692.2005.00748.x.
[26] J. Jeon, Y. Kang, J.H. Park, Y. Chung, Corrosion-erosion behavior of $MgAl_2O_4$ spinel refractory in contact with high MnO slag, Ceram. Int. 43 (2017) 15074–15079, https://doi.org/10.1016/j.ceramint.2017.08.034.
[27] H. Zuo, C. Wang, Y. Liu, Dissolution behavior of a novel Al_2O_3-SiC-SiO_2-C composite refractory in blast furnace slag, Ceram. Int. 43 (2017) 7080–7087, https://doi.org/10.1016/j.ceramint.2017.02.138.
[28] K. Jiao, X. Fan, J. Zhang, K. Wang, Y. Zhao, Corrosion behavior of alumina-carbon composite brick in typical blast furnace slag and iron, Ceram. Int. 44 (2018) 19981–19988, https://doi.org/10.1016/j.ceramint.2018.07.265.
[29] T. Hirata, T. Morimoto, S. Ohta, N. Uchida, Improvement of the corrosion resistance of alumina-chromia ceramic materials in molten slag, J. Eur. Ceram. Soc. 23 (2003) 2089–2096, https://doi.org/10.1016/S0955-2219(03)00023-2.
[30] X. Yu, R.J. Pomfret, K.S. Coley, Dissolution of alumina in mold fluxes, Metall. Mater. Trans. B 28 (1997) 275–279, https://doi.org/10.1007/s11663-997-0094-3.
[31] S.A. Nightingale, G.A. Brooks, B.J. Monaghan, Degradation of MgO refractory in CaO-SiO_2-MgO-FeO_x and CaO-SiO_2-Al_2O_3-MgO-FeO_x slags under forced convection, Metall. Mater. Trans. B 36 (2005) 453–461, https://doi.org/10.1007/s11663-005-0036-x.
[32] C.G. Aneziris, E.M. Pfaff, H.R. Maier, Corrosion mechanisms of low porosity ZrO_2 based materials during near net shape steel casting, J. Eur. Ceram. Soc. 20 (2000) 159–168, https://doi.org/10.1016/S0955-2219(99)00149-1.
[33] L. Chen, M. Guo, H. Shi, S. Huang, P.T. Jones, B. Blanpain, A. Malfliet, Effect of ZnO level in secondary copper smelting slags on slag/magnesia-chromite refractory interactions, J. Eur. Ceram. Soc. 36 (2016) 1821–1828, https://doi.org/10.1016/j.jeurceramsoc.2016.02.004.
[34] M. Guo, S. Parada, P.T. Jones, E. Boydens, J.V. Dyck, B. Blanpain, P. Wollants, Interaction of Al_2O_3-rich slag with MgO-C refractories during VOD refining-MgO and spinel layer formation at the slag/refractory interface, J. Eur. Ceram. Soc. 29 (2009) 1053–1060, https://doi.org/10.1016/j.jeurceramsoc.2008.07.063.
[35] W.K. Banda, J.D. Steenkamp, E. Matinde, An investigation into the wear mechanisms of carbon- and silicon carbide-based refractory materials by silicomanganese alloy, J. South. Afr. Inst. Min. Metall. 120 (2020) 333–344, https://doi.org/10.17159/2411-9717/959/2020.
[36] S. Jansson, V. Brabie, P. Jönsson, Corrosion mechanism of commercial doloma refractories in contact with CaO-Al_2O_3-SiO_2-MgO slag, Ironmak. Steelmak. 35 (2008) 99–107, https://doi.org/10.1179/030192307×231595.
[37] A.H. Bui, H.M. Ha, I.S. Chung, H.G. Lee, Dissolution kinetics of alumina into mold fluxes for continuous steel casting, ISIJ Int. 45 (2005) 1856–1863, https://doi.org/10.2355/isijinternational.45.1856.
[38] V. Kircher, Burhanuddin, H. Harmuth, Design, operation and evaluation of an improved refractory wear testing technique, Measurement 178 (2021), 109429, https://doi.org/10.1016/j.measurement.2021.109429.
[39] A. Huang, Y. Wang, Y. Zou, H. Gu, L. Fu, Dynamic interaction of refractory and molten steel: corrosion mechanism of alumina–magnesia castables, Ceram. Int. 44 (2018) 14617–14624, https://doi.org/10.1016/j.ceramint.2018.05.085.
[40] B. Ma, Y. Yin, Q. Zhu, Y. Zhai, Y. Li, G. Li, J. Yu, Slag corrosion and penetration behaviors of $MgAl_2O_4$ and Al_2O_3 based refractories, Refract. Ind. Ceram. 56 (2016) 494–501, https://doi.org/10.1007/s11148-016-9876-y.
[41] F. Verhaeghe, J. Liu, M. Guo, S. Arnout, B. Blanpain, P. Wollants, Determination of the dissolution mechanism of Al_2O_3 in CaO-Al_2O_3-SiO_2 liquids using a combined experimental-numerical approach, J. Appl. Phys. 103 (2008), 023506, https://doi.org/10.1063/1.2830852 (023506–023501).
[42] W.A. Calvo, P. Pena, A.G. Tomba Martinez, Post-mortem analysis of alumina–magnesia-carbon refractory bricks used in steelmaking ladles, Ceram. Int. 45 (2019) 185–196, https://doi.org/10.1016/j.ceramint.2018.09.150.
[43] K.H. Sandhage, G.J. Yurek, Direct and indirect dissolution of sapphire in calcia-magnesia–alumina–silica melts: dissolution kinetics, J. Am. Ceram. Soc. 73 (1990) 3633–3642, https://doi.org/10.1111/j.1151-2916.1990.tb04269.x.
[44] V. Muñoz, S. Camelli, A.G. Tomba Martinez, Slag corrosion of alumina–magnesia-carbon refractory bricks: experimental data and thermodynamic simulation, Ceram. Int. 43 (2017) 4562–4569, https://doi.org/10.1016/j.ceramint.2016.12.114.

[45] P. Korgul, D.R. Wilson, W.E. Lee, Microstructural analysis of corroded alumina–spinel castable refractories, J. Eur. Ceram. Soc. 17 (1997) 77–84, https://doi.org/10.1016/S0955-2219(96)00073-8.
[46] F. Verhaeghe, J. Liu, M. Guo, S. Arnout, B. Blanpain, P. Wollants, Dissolution and diffusion behavior of Al_2O_3 in a CaO–Al_2O_3–SiO_2 liquid: an experimental-numerical approach, Appl. Phys. Lett. 91 (2007), 124104, https://doi.org/10.1063/1.2786854 (124104–124101).
[47] B.J. Monaghan, S.A. Nightingale, L. Chen, G.A. Brooks, The dissolution behaviour of selected oxides in CaO-SiO_2-Al_2O_3 slags, in: Proceedings of the Int. Conf. on Molten Slags Fluxes and Salts VII, 2004, pp. 585–94.
[48] B.J. Monaghan, L. Chen, J. Sorbe, Comparative study of oxide inclusion dissolution in CaO-SiO_2-Al_2O_3 slag, Ironmak. Steelmak. 32 (2005) 258–264, https://doi.org/10.1179/174328105×28793.
[49] B.J. Monaghan, L. Chen, Dissolution behavior of alumina micro-particles in CaO–SiO_2–Al_2O_3 liquid oxide, J. Non Cryst. Solids 347 (2004) 254–261, https://doi.org/10.1016/j.jnoncrysol.2004.09.011.
[50] K.W. Yi, C. Tse, J.-H. Park, M. Valdez, A.W. Cramb, S. Sridhar, Determination of dissolution time of Al_2O_3 and MgO inclusions in synthetic Al_2O_3-CaO-MgO slags, Scand. J. Met. 32 (2003) 177–184, https://doi.org/10.1034/j.1600-0692.2003.20631.x.
[51] J. Liu, F. Verhaeghe, M. Guo, B. Blanpain, P. Wollants, In situ observation of the dissolution of spherical alumina particles in CaO-Al_2O_3-SiO_2 melts, J. Am. Ceram. Soc. 90 (2007) 3818–3824, https://doi.org/10.1111/j.1551-2916.2007.02062.x.
[52] S. Sridhar, A.W. Cramb, Kinetics of Al_2O_3 dissolution in CaO-MgO-SiO_2-Al_2O_3 slags: in situ observations and analysis, Metall. Mater. Trans. B 31 (2000) 406–410, https://doi.org/10.1007/s11663-000-0059-2.
[53] M. Valdez, K. Prapakorn, A.W. Cramb, S. Sridhar, Dissolution of alumina particles in CaO-Al_2O_3-SiO_2-MgO slags, Ironmak. Steelmak. 29 (2002) 47–52, https://doi.org/10.1179/030192302225001965.
[54] W.G. Cochran, The flow due to a rotating disc, Math. Proc. Camb. Philos. Soc. 30 (1934) 365–375, https://doi.org/10.1017/S0305004100012561.
[55] V.G. Levich, Physicochemical Hydrodynamics, Prentice Hall, Englewood Cliffs, New Jersey, 1962.
[56] M. Eisenberg, C.W. Tobias, C.R. Wilke, Ionic mass transfer and concentration polarization at rotating electrodes, J. Electrochem. Soc. 101 (1954) 306, https://doi.org/10.1149/1.2781252.
[57] M. Kosaka, S. Minowa, Mass-transfer from solid metal cylinder into liquid metal, Tetsu-to-Hagane 52 (1966) 1748–1762, https://doi.org/10.2355/tetsutohagane1955.52.12_1748.
[58] F. Tachibana, S. Fukui, Convective heat transfer of the rotational and axial flow between two concentric cylinders, Bull. JSME 7 (1964) 385–391, https://doi.org/10.1299/jsme1958.7.385.
[59] J. Guarco, S. Burhanuddin, S. Vollmann, H. Harmuth, Method for determination of effective binary diffusivities in dissolution of dense ceramic materials, Ceram. Int. (2021), https://doi.org/10.1016/j.ceramint.2021.11.264.
[60] J. Xin, L. Gan, L. Jiao, C. Lai, Accurate density calculation for molten slags in SiO_2-Al_2O_3-CaO-MgO systems, ISIJ Int. 57 (2017) 1340–1349, https://doi.org/10.2355/isijinternational.ISIJINT-2017-070.

7.4 Publication IV

Sherwood correlation for finger-test experiments

Jerónimo Guarco, Burhanuddin, Sandra Vollmann, Harald Harmuth

Results in Engineering 15 (2022) 100610

Contents lists available at ScienceDirect

Results in Engineering

journal homepage: www.sciencedirect.com/journal/results-in-engineering

Sherwood correlation for finger-test experiments

Jerónimo Guarco *, Burhanuddin, Sandra Vollmann, Harald Harmuth

Chair of Ceramics, Montanuniversität Leoben, Peter-Tunner Straße 5, 8700, Leoben, Austria

ARTICLE INFO

Keywords:
Mass transfer
Finger test
Sherwood equation
Dissolution
Rotating cylinder

ABSTRACT

Finger-test experiments are frequently conducted in continuous-wear investigations of ceramic materials. However, mass transfer equations accurately representing these scenarios are not yet available, which can lead to erroneous estimation of dissolution-related parameters due to poor approximations. In this study, a Sherwood correlation for finger-test experiments was developed. The equation applies to rods or nearly cylindrical specimens that are rotated in a liquid contained in a cylindrical receptacle. The equation is derived from numerical results simulating the dissolution of ceramic materials in liquid slags, where the dissolution is dominated by mass transfer in the liquid. For these simulations, surface profiles from the experimental results were employed. Based on the derived equation, a methodology for the calculation of mass transfer coefficients for dissolution processes was designed that enables diffusivity determination. This equation is also suitable for heat transfer calculations. The equation is in agreement with the results obtained by simulation and other documented heat and mass transfer equation, for the latter the fit is poorer due to differences in the experiment configuration.

1. Introduction

Finger-test experiments are frequently used in investigations of continuous wear in ceramic systems, where the dissolution of the material in liquid slags or melts is commonly analysed. In these experiments, a cylindrical sample of the material is immersed in a liquid and rotated at a constant speed. When the dissolution process is dominated by the diffusion of the dissolved species in the liquid, as is frequently the case [1–4], the dissolving mass flux can be estimated through Sherwood equations, which are used to describe the mass flux density in dimensionless form. However, a mass transfer equation that is directly applicable to finger-test experiments has not yet been introduced. Consequently, researchers have employed approximations based on Sherwood equations, for which the geometry and conditions are not exactly related [5–8].

Previous publications by the authors addressed simulations of finger-test experiments and provided an appropriate framework for dissolution investigation. In the first publication [9], the method was verified in a comparison to other documented Sherwood equations. Later, it was validated against real experiments and was used to determine effective binary diffusivities [10,11]. In this communication, a Sherwood correlation that is applicable to the sample mantle in finger-test experiments is presented for systems with large Schmidt numbers. The correlation is based on the authors' previous works and experimentally determined surface profiles.

2. Review of mathematical model

A simulation method was applied in a previous study by the authors [9–11]. Herein, computational fluid dynamics (CFD) simulations of the finger-test experiments are conducted using a multiphase model developed in ANSYS Fluent. The flow is laminar and both the atmospheric and slag flow fields are resolved using the volume of fluid method. Table 1 present a summary of the numerical schemes used for the CFD simulations.

Given the large Schmidt number present in slag/refractory systems, the species equation is not solved with CFD to avoid fine domain discretisation and consistent time steps. Rather, an asymptotic boundary layer approach for large Schmidt numbers based on the work introduced by Lighthill in 1950 [12] is applied in the post-processing step. The equation first introduced for heat transfer problems is adapted here for mass transfer problems and axisymmetric bodies. It is presented in Equation (1):

$$Sh_0(x) = \frac{lSc^{\frac{1}{3}}}{9^{\frac{1}{3}}\nu^{\frac{1}{3}}\Gamma\left(\frac{4}{3}\right)}\sqrt{\mathscr{R}\,\beta(x)}\left[\int_{\ell}\mathscr{R}\sqrt{\mathscr{R}\beta(\zeta)}\,ds\right]^{-\frac{1}{3}}. \tag{1}$$

Here, Sh_0 is the Sherwood number without consideration of the Stefan velocity in the boundary conditions, which makes it equivalent to

* Corresponding author.
E-mail address: jeronimo.guarco@unileoben.ac.at (J. Guarco).

https://doi.org/10.1016/j.rineng.2022.100610
Received 20 June 2022; Received in revised form 8 August 2022; Accepted 22 August 2022
Available online 27 August 2022

Nomenclature

Symbols

B	dimensionless saturation weight content
BC	clearance from crucible bottom to sample tip
d	gap width from average radius
D	effective diffusivity
j	mass flux density
l	characteristic length
L	immersion length
$\hat{n}$	normal direction to wall
r	radial coordinate
R	average radius of specimen
$\mathscr{R}$	radius of revolution body
Re	Reynolds number
S	deviation from cylindrical shape
Sc	Schmidt number
Sh	Sherwood number
Sh_0	Sherwood number without consideration of Stefan velocity
$\hat{t}$	tangential direction to wall
Ta	Taylor number
Ta_c	critical Taylor number
$\vec{v}$	velocity
v_t	velocity in tangential direction
w_s	saturation mass content
w_∞	bulk mass content
z	axial coordinate
R_2	radius of containing cylindrical receptacle

Greek symbols

β	derivative of velocity in normal direction
Γ	gamma function
η	outer to inner radius ratio
μ	dynamic viscosity
ν	kinematic viscosity
ρ	density of liquid
τ	shear stress
χ	correction for influence of Stefan velocity
ω	rotational speed

Table 1
Summary of CFD simulation set-up.

Multiphase	Volume of fluid with geometric reconstruction
Surface tension	Continuous surface force model
Pressure-velocity coupling	Coupled scheme
Momentum and swirl equations	Second order upwind schemes
Pressure cell to face interpolation	PRESTO! scheme
Mesh type and size	0.125 mm quadrilateral element for sample wall vicinity 0.25 mm triangular elements for the rest of the domain
Time advancement/ Time-step	First order implicit/0.0001s

the Nusselt number in heat transfer. Equation (1) can be used for the calculation of local, steady-state mass, or heat transfer coefficients, and this profile can be integrated to calculate the average Sherwood numbers. Variable β is a result of the flow field and can be computed from the shear stresses on the rotating sample, as per Equation (2):

$$\beta = \frac{\partial v_t}{\partial \hat{n}} = \frac{\partial(\vec{v}\cdot\hat{t})}{\partial \hat{n}} = \frac{\partial \vec{v}}{\partial \hat{n}}\cdot\hat{t} = \frac{1}{\mu}(\tau_z t_z + \tau_r t_r). \tag{2}$$

The simulations here involve the geometries of corroded samples that are obtained from laser measurements of the sample after the corrosion steps, as described by Kircher et al. [13]. The method was applied to several samples with slags having different properties (density and viscosity). Fig. 1 gives an overview of the methodology applied.

3. Sherwood correlation

The repetitive application of the method yields several results. Curve fitting of these results is conducted with the influencing parameters. It engenders a formula that is useful for conducting finger tests or similar experiments on both heat and mass transfer. The experiments consider corroded samples, rather than perfect cylindrical surfaces, where the deviation of the sample from the cylindrical shape of the average radius $\overline{R}$ is given by S and computed as the standard error,

$$S = \sqrt{\frac{1}{N-1}\sum_{i=1}^{N}(R(z_i) - \overline{R})^2}.$$

A schematic description of the setup and influencing parameters is displayed in Fig. 2.

Here L represents the length of the sample that is immersed in the fluid, $\overline{R}$ is the average radius of the sample only considering the immersed part, d is the gap width between the vessel and the average radius, BC represents the clearance from the sample to the vessel bottom, and ω is the rotational speed of the sample.

The dependency of the mass flux on the Schmidt number was fixed by the asymptotic boundary layer approach employed with a factor of $Sc^{1/3}$. For this correlation, 18 simulations were completed, where the Taylor number (Ta) was at most 53% of the critical Taylor number (Ta_c), implying centrifugal instabilities in the form of Taylor vortices were not considered. The Taylor number is defined as $Ta = \frac{2\omega^2 d^4 \eta^2}{(1-\eta^2)\nu^2}$, where η is the ratio of the sample to containing receptacle radii, and ν is the kinematic viscosity of the liquid. To calculate the critical Taylor number, the

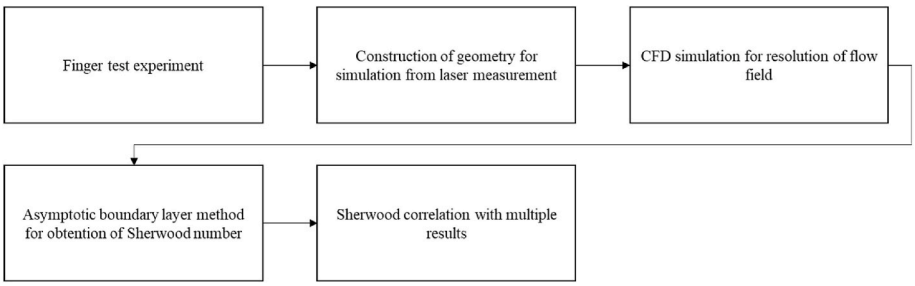

Fig. 1. Flowchart of method applied for obtention of Sherwood correlation.

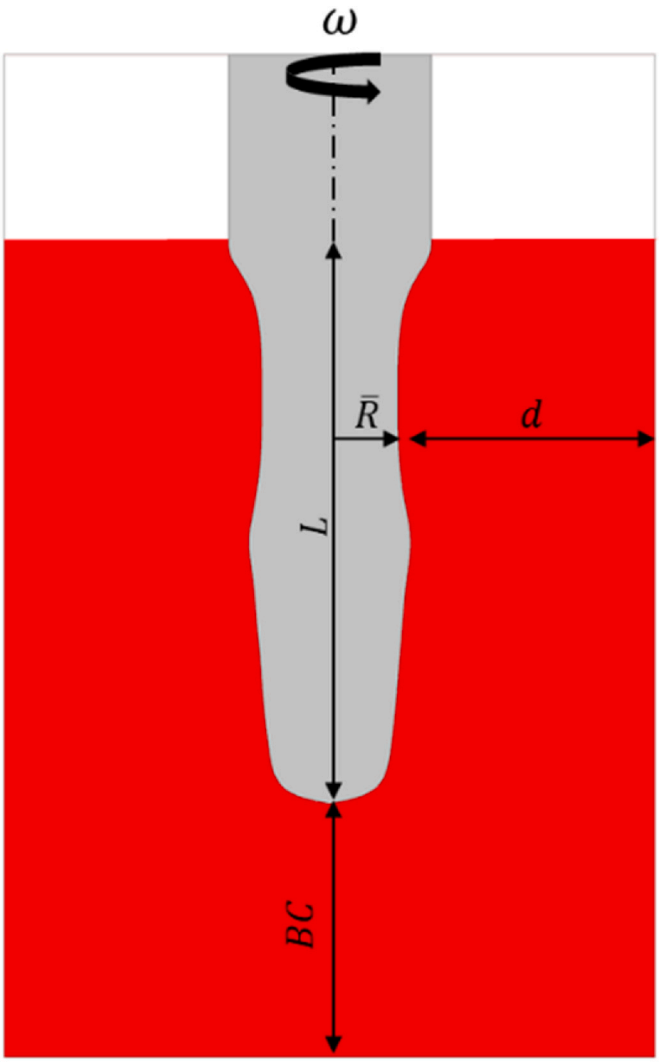

Fig. 2. Illustration of simulated experiments and influencing parameters.

following correlation of the data presented by DiPrima et al. [14], $Ta_c = 1600/\eta^{1.005}$, can be employed.

The fitting was obtained by minimization of the sum of squares of residuals using Matlab's *fminunc* optimization function. The Sherwood correlation is given by Equation (3), where $Sh_d = \frac{jd}{D\Delta c}$ is the Sherwood number with the gap width (d) as the characteristic length, D is the effective binary diffusivity, Δc is the concentration difference between saturation and bulk, j is the mass flux density, $Re = \frac{v\rho\overline{R}}{\mu}$ is the Reynolds number with the average radius ($\overline{R}$) as the characteristic length, v is the linear velocity of the rotating cylinder circumference ($\omega\overline{R}$), ρ is the fluid density, μ is the dynamic viscosity, and $Sc = \frac{\mu}{D\rho}$ is the Schmidt number. The physical significance of the parameters can be seen from this equation.

$$Sh_d = 0.10\, Re^{0.65} Sc^{1/3} \left(\frac{d}{\overline{R}}\right)^{1.49} \left(\frac{BC}{L}\right)^{0.32} \tag{3}$$

The Sherwood values computable with Equation (3) do not consider the effect of the Stefan velocity on the mass transfer rate. This effect can be easily incorporated as demonstrated by Merk [15] and with the methods proposed in our previous works [9,10]. This means that Equation (3) is directly applicable to heat transfer calculations when exchanging the Sherwood number for the Nusselt number and the Schmidt number for the Prandtl number.

The fit of Equation (3) to the values obtained by simulation is displayed in Fig. 3, where the Sherwood numbers are normalised by the factor $X = Sc^{1/3}\left(\frac{d}{\overline{R}}\right)^{1.49}\left(\frac{BC}{L}\right)^{0.32}$ for representation as a function of Re only. The value of R^2 of 0.93 indicates the satisfactory fit of the data.

Because the simulations were performed from the profiles of experiments conducted by the authors, the range of the parameter validity must be observed and is documented in Table 2.

3.1. Application to dissolution studies

To avoid erroneous application of the results, it should be stated that, in dissolution, determination of the mass flux density with this Sherwood relation requires the following calculation:

$$j = \chi \frac{D}{d} Sh_d \rho B; B = \frac{w_s - w_\infty}{1 - w_s}. \tag{4}$$

Here, B is a dimensionless concentration difference composed of the mass contents of the diffusing species in the saturated liquid w_s and bulk liquid w_∞, and χ allows for the aforementioned influence of the Stefan flow on the effective diffusive boundary layer thickness. An approximation based on [15] that is valid for a high Sc number is

$$\chi \approx \frac{1}{1 + 0.566B}. \tag{5}$$

While χ accounts for the influence of the Stefan flow on fluid dynamics, the denominator of B considers its direct convective contribution to diffusion.

3.2. Comparison to documented equations

The same comparison that was performed between the simulation results and documented equations in a previous publication [9] was conducted here considering the presented Sherwood correlation. Table 3 presents the correlation together with the equations for setups similar to the finger-test experiments, where the name given to the equations corresponds to the first author of the publication where each one is presented.

Notably, the power dependency on the Reynolds number of the correlation is close to that of the equation presented by Eisenberg et al. [16] and differs only marginally from that of Kosaka and Minowa [17]. This matches our observations in Ref. [9], where it was also clearly noted that the logarithm of the simulated data shared a similar slope to the logarithm of the Reynolds numbers for both equations. From all the equations compared in Ref. [9], Kosaka and Minowa demonstrated the

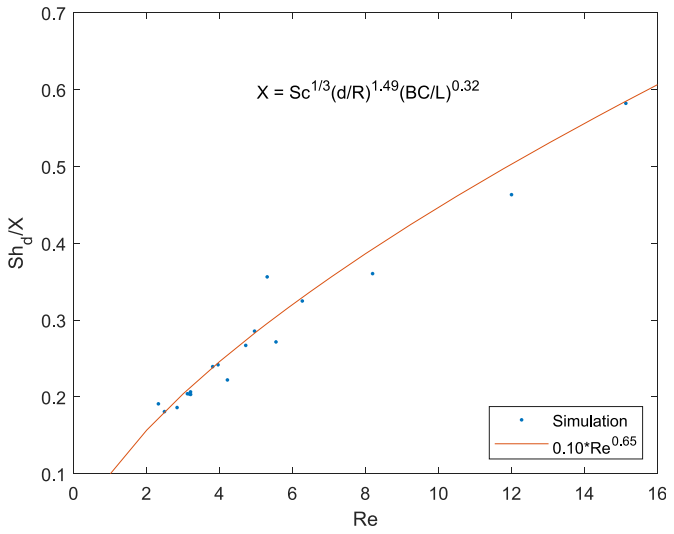

Fig. 3. Fitting of correlation to values obtained by simulation.

Table 2
Valid parameter ranges.

Parameter		
2.3	$< Re <$	15.1
2.53	$< d/\overline{R} <$	4.34
0.37	$< BC/L <$	0.88
0.03	$< S/\overline{R} <$	0.23
56	$< Ta <$	3958
0.01	$< Ta/Ta_c <$	0.53
	$Sc \rightarrow$	∞

Table 3
Sherwood correlations from literature for similar setups.

	Equation
Correlation	$Sh_d = 0.10\, Re^{0.65} Sc^{1/3} \left(\frac{d}{\overline{R}}\right)^{1.49} \left(\frac{BC}{L}\right)^{0.32}$
Eisenberg [16]	$Sh_d = 0.0642 Re^{0.7} Sc^{0.356} \frac{d}{\overline{R}}$
Kosaka [17]	$Sh_d = 0.0547 Re^{0.75} Sc^{\frac{1}{3}} \frac{d}{\overline{R}}$
Tachibana [18]	$Sh_d = 0.21 Re^{1/2} Sc^{1/4} \left(\frac{d}{\overline{R}}\right)^{\frac{3}{4}}$
Srinivasan [20]	$Ta < Ta_c$
	$Sh_d = \frac{3d}{\overline{R}\log\left(\frac{R_2}{\overline{R}}\right)} + 0.0048 Re Sc^{1/3} \frac{d}{\overline{R}} \left(\frac{\overline{R}}{R_2}\right)^{-1.25}$

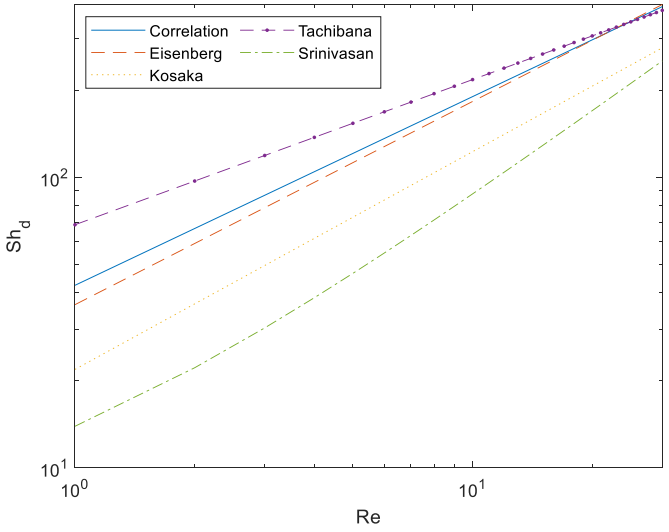

Fig. 4. Comparison of correlation and documented Sherwood equations.

best fit with the newly established calculation procedure based on Equation (1) above. Its maximum error of 18% occurred for $Re = 1$ and decreased for Reynolds numbers up to 30. The discrepancy with Tachibana and Fukui [18] can be attributed to the flow regimen, as the authors conducted experiments within the Taylor vortex regime. The deviation from the Srinivasan findings could have occurred because their results, which were obtained via simulation, considered only a Couette flow; hence, the end effects on the velocity dropped out. In the setup considered herein, the bottom clearance serves as a region for the development of axial flow as a consequence of the rotation of the sample tip, which acts as a centrifugal pump. The dependency on the Schmidt number is fixed by the asymptotic boundary layer method and is the theoretical dependency for a large Schmidt number [19]. Only Tachibana presented a clearly different dependency on this number, which can be attributed to fluids of considerably low Prandtl numbers, from which the equation was derived. Clearly, the effects of other geometrical simplexes cannot be compared because none of the equations found in the literature considers these, and most of them are based only on an annular gap with no bottom clearance.

The equations in Table 3 are plotted in logarithmic form in Fig. 4. For correlation, the geometrical parameters employed (BC, L, d, and $\overline{R}$) were considered as in Ref. [9]. The dependency of the Schmidt number on the Tachibana and Fukui equation is changed from $Sc^{1/4}$ to $Sc^{1/3}$. The above remarks are clearly visible in this figure. For the ideal cylinder shape, the best agreement is obtained with the equation of Kosaka and Minowa [17]. For the actual specimen shapes of the dissolution experiments characterised by the parameter $\frac{S}{\overline{R}}$ as given in Table 2, the correlation is closest to Eisenberg's Equation [16] for all Reynolds numbers.

4. Conclusions

A novel Sherwood correlation for finger-test experiments was presented. The equation was obtained by CFD simulations of finger test experiments together with an asymptotic boundary layer method for the calculation of Sherwood number. The simulations considered the corroded shape of the rotating sample, for which the geometry was obtained from laser measurements. This equation can be applied to both heat and mass transfer calculations in experiments where a cylindrical or nearly cylindrical sample is rotated within a liquid in a cylindrical receptacle. This can be significant in refractory and ceramic testing, where these experiments are largely established. However, to date, no equation has been available for a setup with bottom clearance and consideration of the actual wear profiles. A main advantage of such an equation is the simple application compared to the large effort and expertise necessary for conducting the simulations. Moreover, finger test investigations can benefit from more accurate estimation of dissolution related parameters, such as diffusivities. The accuracy of the proposed equation was validated by comparing documented equations in similar setups. Here, we found the equation of Eisenberg gave the closest fit, and the error between equations decreased with Reynolds number. A method for application in dissolution studies considering the Stefan flow and its effect on the species boundary layer thickness was also presented.

CRediT author statement

Jerónimo Guarco: Conceptualization, Methodology, Software, CFD Simulations and Validation, Formal analysis, Investigation, Writing – Original, Visualization. **Burhanuddin:** Investigation – Performing experiments. **Sandra Vollmann:** Conceptualization, Writing - Review & Editing, Supervision, Project administration. **Harald Harmuth:** Writing – Review & Editing, Supervision, Resources, Funding acquisition.

Declaration of competing interest

The authors declare that they have no known competing financial interests or personal relationships that could have appeared to influence the work reported in this paper.

Acknowledgements

The authors gratefully acknowledge the financial support under the scope of the COMET program within the K2 Center "Integrated Computational Material, Process and Product Engineering (IC-MPPE)" (Project No. 859480). This program is supported by the Austrian Federal Ministries for Climate Action, Environment, Energy, Mobility, Innovation and Technology (BMK) and for Digital and Economic Affairs (BMDW), represented by the Austrian research funding association (FFG), and the federal states of Styria, Upper Austria, and Tyrol.

References

[1] S. Jansson, V. Brabie, P. Jonsson, Corrosion mechanism and kinetic behaviour of MgO-C refractory material in contact with CaO-Al2O3-SiO2-MgO slag, Scand. J. Metall. 34 (2005) 283–292, https://doi.org/10.1111/j.1600-0692.2005.00748.x.

[2] P. Lian, A. Huang, H. Gu, Y. Zou, L. Fu, Y. Wang, Towards prediction of local corrosion on alumina refractories driven by Marangoni convection, Ceram. Int. 44 (2018) 1675–1680, https://doi.org/10.1016/j.ceramint.2017.10.095.

[3] J. Pötschke, C. Brüggmann, Premature wear of refractories due to Marangoni-convection, Steel Res. Int. 83 (2012) 637–644, https://doi.org/10.1002/srin.201100294.

[4] L.F. Verdeja, R. Parra, F. Barbés Fernández, V. Bazán, Application of the nodal wear model to the static finger test of refractories corrosion, Steel Grips 3 (2005) 105–110. https://www.researchgate.net/publication/265216342.

[5] A.H. Bui, H.M. Ha, I.S. Chung, H.G. Lee, Dissolution kinetics of alumina into mold fluxes for continuous steel casting, ISIJ Int. 45 (2005) 1856–1863, https://doi.org/10.2355/isijinternational.45.1856.

[6] G.Y. Shi, T.A. Zhang, Z.H. Dou, L.P. Niu, Dissolution behavior of al2o3 inclusions in cao-al2o3 based slag representing aluminothermic reduction slag, Crystals 10 (2020) 1–12, https://doi.org/10.3390/cryst10111061.

[7] I. Kasimagwa, V. Brabie, P.G. Jönsson, Slag corrosion of MgO–C refractories during secondary steel refining, Ironmak. Steelmak. 41 (2014) 121–131, https://doi.org/10.1179/1743281213Y.0000000110.

[8] H. Um, K. Lee, J. Choi, Y. Chung, Corrosion behavior of MgO-C refractory in ferromanganese slags, ISIJ Int. 52 (2012) 62–67, https://doi.org/10.2355/isijinternational.52.62.

[9] J. Guarco, H. Harmuth, S. Vollmann, Method for determination of mass transfer coefficients for dissolution of dense ceramics in liquid slags, Int. J. Heat Mass Tran. 186 (2022), 122494, https://doi.org/10.1016/j.ijheatmasstransfer.2021.122494.

[10] J. Guarco, Burhanuddin, S. Vollmann, H. Harmuth, Method for determination of effective binary diffusivities in dissolution of dense ceramic materials, Ceram. Int. 48 (2022) 7456–7463, https://doi.org/10.1016/j.ceramint.2021.11.264.

[11] Burhanuddin, J. Guarco, H. Harmuth, S. Vollmann, Application of an improved testing device for the study of alumina dissolution in silicate slag, J. Eur. Ceram. Soc. (2022), https://doi.org/10.1016/j.jeurceramsoc.2022.02.056.

[12] M. Lighthill, Contributions to the theory of heat transfer through a laminar boundary layer, Proc. R. Soc. Lodn. Ser. A Math. Phys. Sci. 202 (1950) 359–377, https://doi.org/10.1098/rspa.1950.0106.

[13] V. Kircher, Burhanuddin, H. Harmuth, Design, operation and evaluation of an improved refractory wear testing technique, Measurement 178 (2021), 109429, https://doi.org/10.1016/j.measurement.2021.109429.

[14] R.C. DiPrima, P.M. Eagles, B.S. Ng, The effect of radius ratio on the stability of Couette flow and Taylor vortex flow, Phys. Fluids 27 (1984) 2403, https://doi.org/10.1063/1.864544.

[15] H.J. Merk, Mass transfer in laminar boundary layers calculated by means of a perturbation method, Appl. Sci. Res. 8 (1959) 237–260, https://doi.org/10.1007/BF00411753.

[16] M. Eisenberg, C.W. Tobias, C.R. Wilke, Ionic mass transfer and concentration polarization at rotating electrodes, J. Electrochem. Soc. 101 (1954) 306, https://doi.org/10.1149/1.2781252.

[17] M. Kosaka, S. Minowa, On the Rate of Dissolution of Carbon into Molten Fe-C Alloy, vol. 8, Transactions of the Iron and Steel Institute of Japan, 1968, pp. 392–400, https://doi.org/10.2355/isijinternational1966.8.392.

[18] F. Tachibana, S. Fukui, H. Mitsumura, Heat transfer in an annulus with an inner rotating cylinder, Trans. Jpn. Soc. Mech. Eng. 25 (1959) 788–792, https://doi.org/10.1299/kikai1938.25.788.

[19] K. Gersten, H. Herwig, Grundlagen der Impuls-, Wärme- und Stoffübertragung aus asymptotischer Sicht, 1992.

[20] R. Srinivasan, S. Jayanti, A. Kannan, Effect of Taylor Vortices on mass transfer from a rotating cylinder, AIChE J. 51 (2005) 2885–2898, https://doi.org/10.1002/aic.10553.

7.5 Publication V

Method for inverse calculation of erosion parameters in slag-refractory systems

Jerónimo Guarco, Sandra Vollmann, Burhanuddin, Harald Harmuth

Method for inverse calculation of erosion parameters in slag-refractory systems

Jerónimo Guarco[a,b,], Sandra Vollmann[b], Harald Harmuth[b], Burhanuddin[b]*

a K1-MET GmbH Metallurgical Competence Center, Linz, Austria
b Chair of Ceramics, Montanuniversität Leoben, Peter-Tunner Straße 5, 8700 Leoben, Austria
* Corresponding author. Tel.: +43 38424023211. E-mail: jeronimo.guarco@unileoben.ac.at

Abstract

Refractory erosion due to fluid flow is caused by the shear stresses acting on the liquid/solid interface. This mechanism of continuous wear has not been extensively investigated based on appropriate physical considerations. This study proposes a novel method for the inverse calculation of erosion parameters in slag-refractory systems. A computational fluid dynamic model is coupled with optimisation software to solve a nonlinear least-squares problem for the identification of erosion parameters from experimental erosion profiles. Erosion-rate modelling is performed based on a three-parameter law of the acting shear stress. A test problem is studied using artificially generated erosion profiles. The feasibility of the approach with two parameters is proven; however, using three parameters causes the problem to become ill-posed. Moreover, the method is successfully applied to a real experiment with an alumina coarse-grain refractory. Statistical analysis of the solutions is performed for both the test problem and real experimental profile. Confidence intervals and regions calculated via linearisation are examined, but their use is limited and should be evaluated for each case. This method can serve as a basis for further investigations concerning the quantification of refractory erosion.

Keywords

Inverse problem, erosion modelling, test-problem, parameter estimation, refractory wear

List of symbols

$\dot{\varepsilon}$.. *erosion rate*

k_d.. *detachment rate*

τ_c.. *critical shear stress*

a.. *exponent*

τ.. *wall shear stress*

v_θ.. *swirl velocity*

Ω_1.. *rotational speed of inner cylinder*

Ω_2.. *rotational speed of outer cylinder*

μ_Ω.. $\frac{\Omega_1}{\Omega_2}$

R_1.. *radius of the sample*

R_2.. *radius of the crucible*

d.. $R_2 - R_1$ *gap width*

η.. R_1/R_2 *radii ratio*

r.. *radial coordinate*

Ta.. $\frac{2{\Omega_1}^2 d^4 \eta^2}{(1-\eta^2)\left(\frac{\mu}{\rho}\right)^2}$ *Taylor number*

μ.. *dynamic viscosity*

ρ.. *density*

z.. *axial coordinate*

v_z.. *axial velocity*

v_r.. *radial velocity*

Φ.. *transport scalar*

V.. *element volume*

∂V.. *boundary of volume element*

$\vec{u}$.. *fluid velocity vector*

$\vec{u}_g$.. *mesh velocity vector*

$\vec{A}$.. *edge area vector in normal direction*

Γ_Φ.. *scalar diffusivity*

S_Φ.. *scalar source term*

Δt.. *time-step*

n_f.. *number of faces of a grid element*

δV.. *volume swept by grid displacement*

w_i.. *weight function*

X.. *node coordinates*

X_i .. *face centroid coordinates*

$\vec{n}$.. *unit normal vector*

$\vec{F}_i$.. *fictitious force caused by node displacement*

K_{ij}.. *spring constant*

$\Delta\vec{x}$.. *node displacement vector*

θ.. $\theta = (k_d, \tau_c, a)^T$.

$\vec{r}$.. *residuals vector*

n.. *number of residual terms*

H.. *Hessian matrix*

J.. *Jacobian matrix*

m.. *number of parameters*

y_i.. *model response (radial surface coordinate at z_i)*

$y_{i,exp}$.. *experimental value (radial surface coordinate at z_i)*

σ.. *standard deviation*

f_{χ^2}.. *chi-square probability density function*

Γ.. *gamma function*

ν.. *degrees of freedom*

N_{exp}.. *number of experiments*

s.. *estimate of standard deviation*

Cov.. *covariance matrix*

$t_{\nu,0.975}$.. *critical value of t-student distribution*

Δ^2.. *95th percentile of χ^2 distribution with m degrees of freedom*

ρ_{k_d,τ_c}.. *coefficient of correlation between k_d and τ_c*

1. Introduction

Refractory erosion is the mechanism of continuous wear caused by fluid movement along a material surface. The flow is responsible for shear forces that cause detachment of the material grains, which are then washed away in the liquid. Generally, the forces are not sufficiently large to initiate the erosion process; this necessitates preconditioning by corrosion through infiltrated liquid, which weakens the grain/matrix bonds [1,2]. The quantification of refractory erosion has not been extensively investigated based on appropriate physical

considerations. One reason for this is the lack of an established erosion law and experimental and computational methods for its depiction.

This study aims to address this problem by introducing a method for the inverse calculation of erosion parameters for refractory materials in liquid slags with experimental erosion profiles. Here, the erosion process is modelled on the macroscale based on Partheniades' equation (Equation (1)), which is firmly established in the field of soil erosion [3]. The use of this equation is rooted in the similarities between soils and refractories, which are both representable by a grain/matrix structure. The erosion law is a function of the wall shear stress (τ), and the erosion parameters include the critical shear stress (τ_c), which characterises the flow condition upon which the shear stress is sufficient to begin grain detachment, the rate of detachment k_d [4], and the exponent a.

$$\dot{\varepsilon} = k_d(\tau - \tau_c)^a \tag{1}$$

$\dot{\varepsilon}$ has dimensions of length/time and is considered as a velocity. This is in contrast to most continuous-wear investigations, where the output of the studies is the mass flux density. The units of τ and τ_c are Pa, and the units of k_d depend on the dimensionless power a as follows: $[k_d] = ms^{-1}Pa^{-a}$.

For reference, a study by Hanson and Simon on soil erosion [5] reported τ_c values for cohesive stream beds between 0.001 and 1000 Pa, with values of k_d in the range of 0.001 to 10 $cm^3/(N{\cdot}s)$. Their study classified erodibility into five groups, which ranged from very erodible to very resistant. Low values of k_d and high values of τ_c correspond to very resistant soil, whereas large values of k_d and low values of τ_c are indicative of very erodible soil. To measure these parameters, an *in-situ* jet testing apparatus is prevalently used in soil-erosion investigations [4–7]. The identification of these parameters is typically based on the measurement of scour depth and consideration of equilibrium depth, as described by Hanson and Cook [7]. Exponent a in Equation (1) is frequently fixed at 1.0 [4,5,7].

The jet testing apparatus is not the only approach that can be used to characterise the erosion process of soils. For example, Karmaker et al. [8] conducted an inverse estimation of erodibility parameters using satellite images of eroded river banks at sites with limited accessibility. They applied three different optimisation methods and successfully obtained the erodibility parameters; their study provides an example of how erodibility parameters can be determined from the erosion profile without *in situ* measurements. Other experimental

approaches for soil-erosion investigations include rotating-cylinder experiments and flume tests [9,10].

Although refractory wear via erosion is often quantified in practice by wear measurement, to our knowledge, there is no mathematical treatment in the literature that is similar to that presented herein for refractories. In this study, the coupling of a computational fluid dynamics (CFD) model with an optimisation routine is introduced for the resolution of a nonlinear least-squares problem. This study aims to identify the erosion parameters of Equation (1) that result in the best fit of the model and the experimental erosion profile.

This study provides a detailed analysis on the feasibility of the proposed method and its applicability to real experimental setups. It is the first presented method for the quantification of refractory erosion with erosion profiles. First, a brief description of the experimental setup is provided in Section 2, followed by a comprehensive description of the simulation model. Subsequently, the implementation of the inverse problem is explained, followed by a description of the test problem, where a statistical assessment of the goodness-of-fit is also discussed. Section 3 is divided between the results of the test problem and those of the real experimental profile. The test problem includes both an exact problem, where the erosion profile is obtained from the simulation, and an artificial problem created by random-noise generation. The inverse calculation is investigated for a model with the three erosion parameters of Equation (1) and also with a fixed exponent a of 1.0. Moreover, identification with the inverse calculation was attempted through multiple experiments. Finally, the conclusions are presented in Section 4.

2. Materials and methods

The objective of this study is to establish a method for the inverse calculation of erosion parameters from experimental erosion profiles. This was achieved by coupling CFD simulations with an optimisation solver to solve a nonlinear least-squares problem. The procedure is summarised in the flowchart shown in Figure 1.

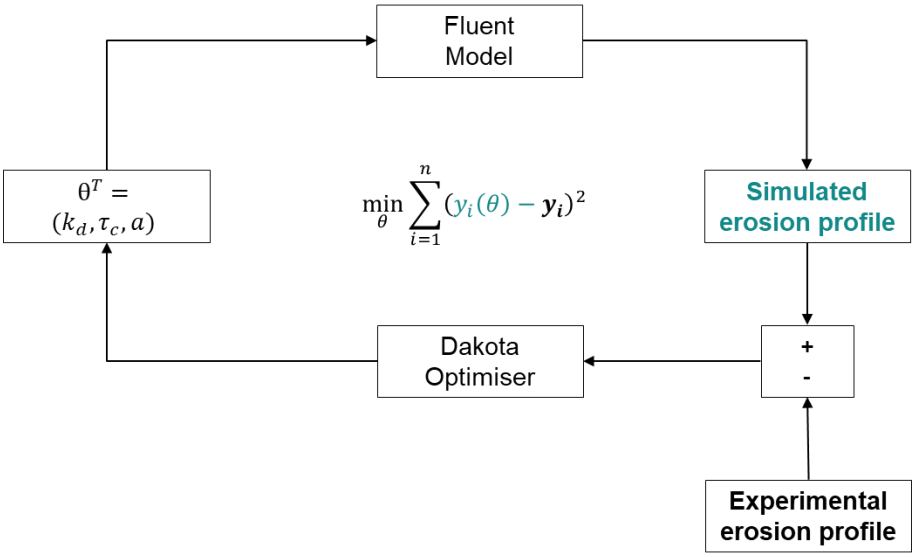

Figure 1. Coupling of model and optimisation routine

When solving the inverse problem, the model can be considered a black box because no explicit formulas for the relationship between the simulation output and erosion parameters are available. Instead, the model is a simulation routine which, in short, consists of solving nonlinear differential equations in a discretised domain through an iterative process. Therefore, this problem must be addressed as a nonlinear one.

The following sections describe the experimental setup, simulation model, and inverse problem.

2.1 Experimental set-up

Kircher et al. presented an experimental setup and method to obtain worn profiles [11]. This provided an experimental basis for the inverse calculation of erosion parameters using erosion profiles. The experimental setup represented a finger test. These experiments involved a furnace with a temperature that was monitored using thermocouples and maintained at the prescribed value. Inside the furnace, a cylindrical sample of the refractory material was rotated within a slag bath at a constant rotational speed. Figure 2 shows a schematic description of the experimental set-up, henceforth referred to as a continuous wear-testing device (CWTD). This rotation generated the bath movement and shear forces that act on the refractory surface. After a defined rotation time, the sample was pulled up and left to drip for 30 min. Subsequently, the furnace plug was removed, and a laser device was placed in its position. The laser scanned the surface of the corroded sample while it rotated at 2 rpm. The processing of the laser measurement data and averaging in the circumferential direction provided the necessary erosion

profile used for the inverse calculation of the erosion parameters. A detailed description of this setup and the processing of the laser measurements is presented in Ref. [11].

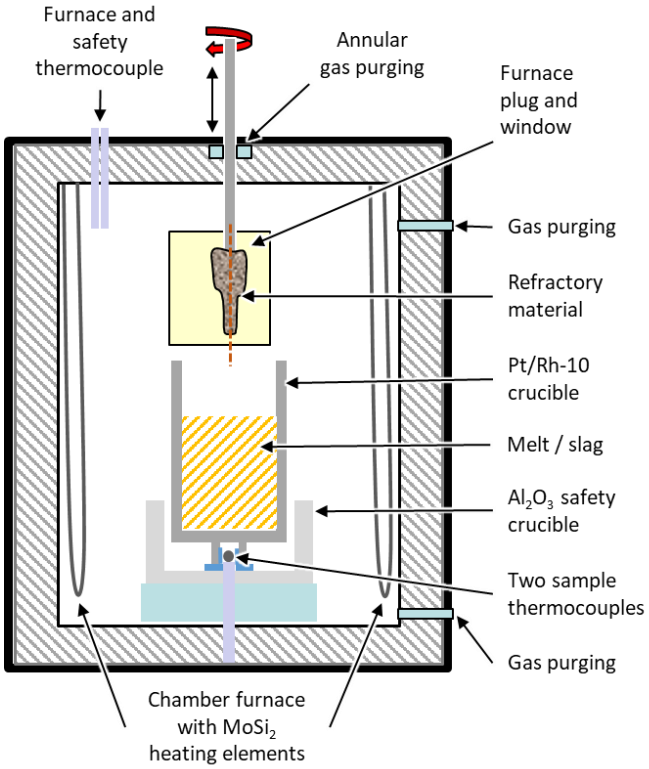

Figure 2. Schematic of the CWTD

2.2 Simulation model

Simulations of the CWTD experiments were conducted with a CFD model developed using ANSYS Fluent v.19.0; the flow field of the slag bath was resolved, and the refractory merely represented the boundary of the model. The model was a two-dimensional (2D), isothermal, axisymmetric model with swirl. Turbulence was not considered in the model; therefore, the exact Navier–Stokes equations were solved. The assumption of laminar flow was based on a comparison with a benchmark problem of fluid dynamics, that is, the flow inside an annular region with rotating cylinders. The first stable flow in such set-ups is a circular Couette (CC) flow, and the azimuthal velocity (v_θ) is given as follows:

$$v_\theta = \Omega_1 \left(\frac{\mu_\Omega - \eta^2}{1 - \eta^2} \right) r + \Omega_1 R_1^2 \left(\frac{1 - \mu_\Omega}{1 - \eta^2} \right) \frac{1}{r}. \quad (2)$$

Centrifugal instabilities appear with increasing rotational speed and the flow-field deviates from the CC flow. Taylor was the first to apply linear stability theory to determine the locus of the first transition [12]. This regime is known as the Taylor vortex flow, where laminar, axisymmetric vortical structures appear. Generally, the transition between different flow structures is determined by the Taylor number (Ta), which represents the ratio between centrifugal and viscous forces [13–16]. For finger-test experiments, the values of the Taylor number are sufficiently low, such that the CC flow is the preferred mode of stability; therefore, a laminar axisymmetric flow is appropriate for the model. Our setup has some fundamental differences to this benchmark problem, such as a relatively short cylinder length, a bottom clearance to the crucible, and a two-phase interface; therefore, this comparison is only done for flow-regimen characterisation. Nevertheless, as will be shown in Section 3, the CC solution provided a good prediction of the velocities in our experiments.

Figure 3 shows a schematic of the model with the discretised domain and boundary conditions. These include a no-shear condition at the slag/atmosphere interface, a no-slip condition at the crucible wall, a constant rotational speed at the refractory wall, and symmetry around the axis of the rotating sample. Furthermore, the refractory wall is a moving boundary because it is subject to erosion. The continuity equation (Equation (3)) and governing equations for the axial (v_z), radial (v_r), and azimuthal (v_θ) velocities are given as follows [17]:

$$\frac{\partial}{\partial z}(\rho v_z) + \frac{\partial}{\partial r}(\rho v_r) + \frac{\rho v_r}{r} = 0, \tag{3}$$

$$\begin{aligned}\frac{\partial}{\partial t}(\rho v_z) + \frac{1}{r}\frac{\partial}{\partial z}(r\rho v_z v_z) + \frac{1}{r}\frac{\partial}{\partial r}(r\rho v_z v_r) \\ = -\frac{\partial p}{\partial z} + \frac{1}{r}\frac{\partial}{\partial z}\left[r\mu\left(2\frac{\partial v_z}{\partial z} - \frac{2}{3}\nabla\cdot\vec{v}\right)\right] \\ + \frac{1}{r}\frac{\partial}{\partial r}\left[r\mu\left(\frac{\partial v_z}{\partial r} + \frac{\partial v_r}{\partial z}\right)\right],\end{aligned} \tag{4}$$

$$\begin{aligned}\frac{\partial}{\partial t}(\rho v_r) + \frac{1}{r}\frac{\partial}{\partial z}(r\rho v_r v_z) + \frac{1}{r}\frac{\partial}{\partial r}(r\rho v_r v_r) \\ = -\frac{\partial p}{\partial r} + \frac{1}{r}\frac{\partial}{\partial z}\left[r\mu\left(\frac{\partial v_r}{\partial z} + \frac{\partial v_z}{\partial r}\right)\right] \\ + \frac{1}{r}\frac{\partial}{\partial r}\left[r\mu\left(2\frac{\partial v_r}{\partial r} - \frac{2}{3}\nabla\cdot\vec{v}\right)\right] - 2\mu\frac{v_r}{r^2} + \frac{2}{3}\frac{\mu}{r}(\nabla\cdot\vec{v}) + \rho\frac{v_\theta^2}{r},\end{aligned} \tag{5}$$

$$\frac{\partial}{\partial t}(\rho v_\theta) + \frac{1}{r}\frac{\partial}{\partial z}(r\rho v_z v_\theta) + \frac{1}{r}\frac{\partial}{\partial r}(r\rho v_r v_\theta) = \frac{1}{r}\frac{\partial}{\partial z}\left[r\mu\left(\frac{\partial v_\theta}{\partial z}\right)\right] + \frac{1}{r^2}\frac{\partial}{\partial r}\left[r^3\mu\frac{\partial}{\partial r}\left(\frac{v_\theta}{r}\right)\right] - \rho\frac{v_r v_\theta}{r}, \quad (6)$$

where $\nabla \cdot \vec{v}$ is

$$\nabla \cdot \vec{v} = \frac{\partial v_z}{\partial z} + \frac{\partial v_r}{\partial r} + \frac{v_r}{r}. \quad (7)$$

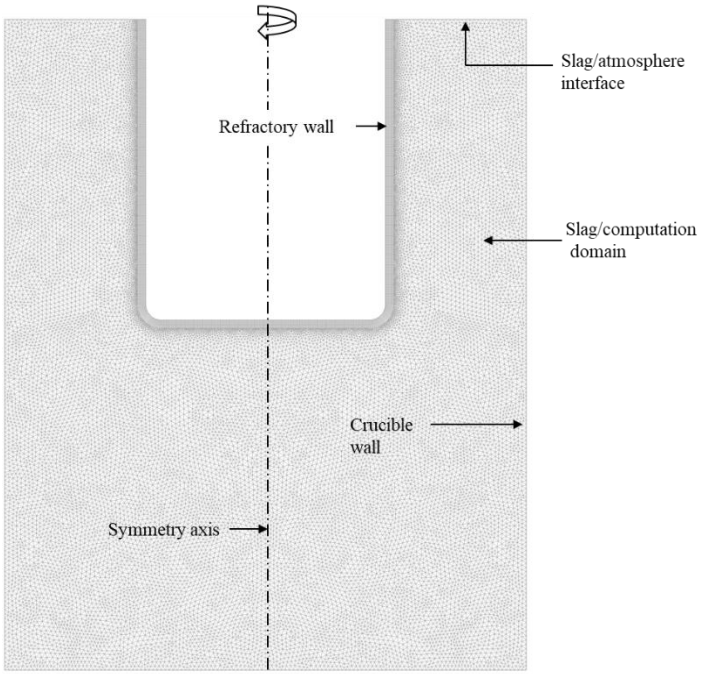

Figure 3. Computational domain

The movement of the refractory wall creates a moving boundary problem, in which the slag domain increases with time. This phenomenon was incorporated into the model using dynamic meshing methods.

The CFD model uses the discretisation of the flow domain with the finite volume method (FVM) to solve the integral form of the Navier–Stokes equations. This means that Equations (3)–(6) are not directly solved; rather, these equations are first integrated over volume. This leads to a balance at each FV element, whereby the conservation of all transport variables is ensured, both for the FV element and globally. Other methods for numerical fluid dynamics include the finite differences and finite element methods. The general form of an

integral conservation equation for an element or cell of the FV method is shown in Equation (8), where the transient and convective terms of the transport scalar (Φ) are given on the LHS, and the diffusive and source terms are shown on the RHS. This transport scalar Φ may represent the magnitude of the x-, y-, or z-velocities, species mass fraction, temperature, or any other user-defined scalar, where the so-called diffusion coefficient Γ_Φ does not necessarily represent mass diffusion and is defined accordingly. Equation (8) is the most general form of the conservation equation, where the grid movement is also considered. When the mesh velocity ($\vec{u}_g$) vanishes, the frequent form of the conservation equation for the rigid flow domains is obtained. Equation (8) and the following equations and formulae are based on Fluent's documentation [17] and should be considered as balances for one element or cell of the FVM, as employed in our model.

$$\frac{d}{dt}\int_V \rho\Phi dV + \int_{\partial V} \rho\Phi\left(\vec{u} - \vec{u}_g\right)\cdot d\vec{A} = \int_{\partial V} \Gamma_\Phi \nabla\Phi \cdot d\vec{A} + \int_V S_\Phi dV \tag{8}$$

The first term on the LHS of Equation (8) is worth discussing because it involves the change in volume of an FVM cell. This term is solved using a first-order backward difference formula for the time derivative and the midpoint rule for volume integration, where Φ represents the average of this scalar in the element.

$$\frac{d}{dt}\int_{V_i} \rho\Phi dV \approx \frac{d(\rho\Phi \mathrm{V})_\mathrm{i}}{dt} = \frac{(\rho\Phi \mathrm{V})_i^{\,n} - (\rho\Phi \mathrm{V})_i^{\,n-1}}{\Delta t} \tag{9}$$

The element's change in volume from time $n-1$ to n must obey the mesh conservation law or space conservation law [18]. This is achieved through the following considerations.

$$V^n = V^{n-1} + \frac{dV}{dt}\Delta t, \tag{10}$$

where

$$\frac{dV}{dt} = \int_{\partial V} \vec{u}_g \cdot d\vec{A} = \sum_j^{n_f} \vec{u}_{g,j} \cdot \vec{A}_j\,, \tag{11}$$

where n_f is the number of faces that shape the element, and $\vec{u}_{g,j} \cdot \vec{A}_j$ is calculated from the volume swept by the control volume face j. The quantity δV_j results from the node displacements and is expressed as

$$\vec{u}_{g,j} \cdot \vec{A}_j = \frac{\delta V_j}{\Delta t}. \tag{12}$$

The typical structure of an element or cell of an FVM is shown in Figure 4. All quantities are computed and stored in the cell or face centroids, and some are extrapolated from cell centroid to cell faces, whereas the nodes define the geometry of the element. The erosion process mandates that the boundary defined by the refractory wall must evolve over time; for this, the movement must be prescribed to the nodes. The node displacement over the refractory wall is a vector field, the magnitude of which is given by the product of the erosion rate with the time step, and the direction is normal to the refractory wall. The erosion rate for a node is computed using Equation (1), for which the wall shear stress (WSS) at the node is necessary. Finally, the normal direction for the nodes is required. All nodes lying on the refractory wall have two neighbouring cells and faces (see Figure 5); therefore, the approach taken here is to use a distance-weighted average of the WSS stored on the neighbouring face centroids, where the weights w_i are defined as follows:

$$w_i = \frac{1}{\|X - X_i\|_2}, \tag{13}$$

where $\|X - X_i\|_2$ represents the Euclidean norm, which is expressed as

$$\|X - X_i\|_2 = \sqrt{(x - x_i)^2 + (y - y_i)^2}, \tag{14}$$

and the wall shear stress for the node is computed as

$$\tau(X) = \frac{\tau_i w_i + \tau_{i+1} w_{i+1}}{w_i + w_{i+1}}. \tag{15}$$

Similarly, the normal direction is determined by unit vectors with an area-weighted average.

$$\vec{n} = \frac{\vec{A}_i + \vec{A}_{i+1}}{\left\|\vec{A}_i + \vec{A}_{i+1}\right\|}, \tag{16}$$

where $\vec{A}$ is a vector in the direction normal to the face that has the magnitude of the element face area. Finally, the displacement vector is given by

$$\vec{\varepsilon}(X) = \dot{\varepsilon}\Delta t \cdot \vec{n} = k_d(\tau(X) - \tau_c)^a \Delta t \cdot \vec{n}. \tag{17}$$

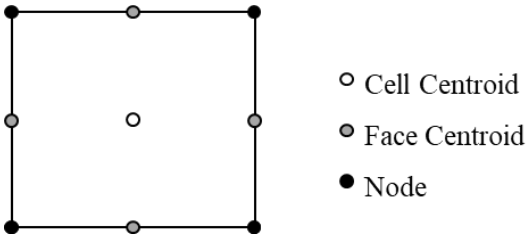

Figure 4. Schematic of 2D cell volume in FVM

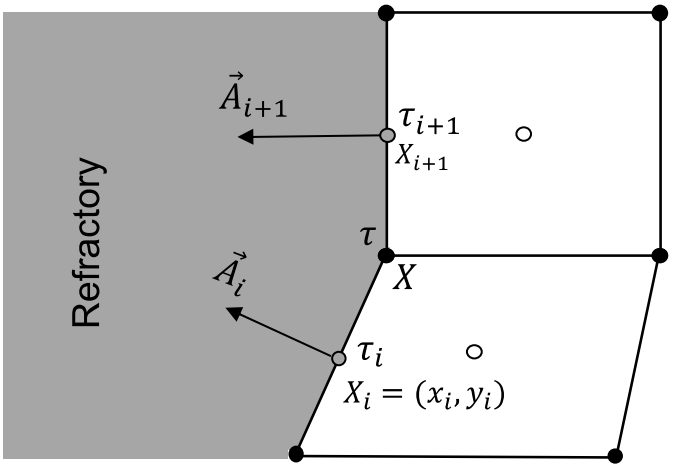

Figure 5. Refractory wall boundary

The node displacement is incorporated into the program with a user-defined function (UDF) written in the C programming language, and it is applied to the refractory wall boundary.

It is important to maintain a good mesh quality after the node updates because an insufficient mesh quality can generate poor results and affect the convergence of the model. For this purpose, different methods that ensure the quality of the mesh are implemented, and the mesh is constructed in a special manner. A boundary-layer mesh composed of quadrilateral elements was used adjacent to the refractory wall, and the rest of the domain was meshed with triangular elements. The nodes lying on the refractory wall were updated with the UDF depending on the prevailing WSS. The boundary-layer mesh was preserved using a boundary-layer-smoothing method, where the node displacement of all interior nodes in this zone was the same as those prescribed for the wall nodes. The nodes in the triangular region were updated using a spring-based smoothing method. In this method, all edges connecting nodes are idealised as a network of springs. Node displacements ($\Delta\vec{x}_i$) result in fictitious forces, which are modelled by Hooke´s law and defined for each node i using Equation (18). The spring constant is defined by Equation (19), where k_{fact} is set as 1. The end position of the nodes was set by determining the equilibrium of these forces (Equation (20)). This method generally yields high-quality meshes. Furthermore, remeshing is possible in the triangular region when

smoothing leads to low-quality elements, and these elements can be marked and coarsened or refined for quality improvement. Remeshing was controlled with a skewness criterion of 0.7, which was based on the relative difference between the optimal and actual cell volumes. Further information on the described methods is presented in the Fluent user manual [19]. Figure 6 presents a schematic of the application of the dynamic meshing methods on the discretised domain.

$$\vec{F}_i = \sum_j^{n_i} k_{ij}\left(\Delta\vec{x}_j - \Delta\vec{x}_i\right) \tag{18}$$

$$k_{ij} = \frac{k_{fact}}{\sqrt{\left|\vec{x}_i - \vec{x}_j\right|}} \tag{19}$$

$$\Delta\vec{x}_i^{m+1} = \frac{\sum_j^{n_i} k_{ij}\Delta\vec{x}_i^m}{\sum_j^{n_i} k_{ij}} \tag{20}$$

The simulation time is important because the model is used in an inverse problem to estimate erosion parameters; therefore, multiple simulations are necessary. A typical inverse problem may require more than 250 simulations. Thus, it is necessary to find a compromise between accuracy and simulation time by adapting the simulation time-step and mesh sizes and neglecting effects such as the resolution of the slag/atmosphere interface with consideration to surface-tension effects. Moreover, the model was solved using parallel computation with a maximum of four partitions.

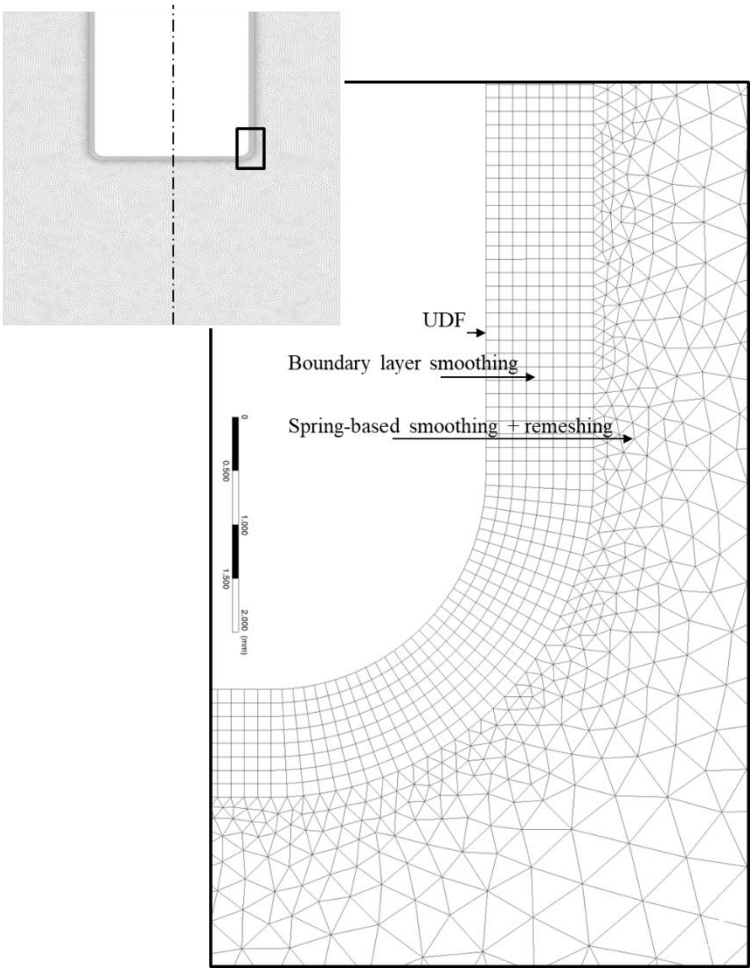

Figure 6. Dynamic meshing methods

As shown in Figure 6, the sample tip is rounded on the edge because a sharp corner would be problematic for the dynamic meshing approach employed, especially for the corner node. However, this corner represents only a very small portion of the entire sample, and its influence is negligible. The dynamic meshing method is applied using an implicit method. This implies that the mesh is updated within the iterations used to solve the governing equations at each time step. The update frequency is 5; that is, the mesh is updated every fifth iteration within the time-step resolution. Furthermore, relaxation factors were employed to improve stability.

From Equation (8) we noticed that although variables are stored at cell centroids, the values at the faces are necessary for the calculation of convective fluxes. Cell-to-face interpolation for the x-, y-, and swirl-velocities was achieved with a convective upstream interpolation for convection kinetics (QUICK) scheme. This method uses quadratic

interpolation with the values of the two neighbouring elements and a further element at an upstream location. Pressure was interpolated using a different method: the pressure staggering option (PRESTO!). This method imitates the characteristics of a staggered grid arrangement, in which the pressure is stored in the cell centroids and the velocities at the faces.

Equations (3)–(6) show that a pressure gradient is necessary when solving for the velocity components, which is also part of the solution process. However, no independent equation for pressure is available for an incompressible flow, and the velocities must satisfy the continuity equation (7). The pressure-velocity coupling is achieved using the pressure-implicit with splitting of operators (PISO) algorithm. References [20,21] or any fundamental book on CFD provide a detailed description of this method. Fundamentally, this is an iterative method, in which a guess of the pressure field is first used to solve the equations for the velocity components, and then a correction for the pressure and velocities is applied. Notably, in the case of large erosion, particularly at the corner, the stability of the solvers can be significantly improved using the coupled solver, where all equations are solved simultaneously. Time resolution is achieved with the first-order implicit method; that is, the time derivative is approximated with a first-order backward formula, and the fluxes and source terms are considered at the current time-step, which makes it implicit.

2.3 Inverse Problem

The model was used with the optimisation software Dakota v.6.11 for the inverse calculation of the erosion parameters $\theta = (k_d, \tau_c, a)^T$. A least-squares problem (Equation (21)) was formulated with the residual vector ($\vec{r}$) computed from the difference between the experimental and simulated erosion profiles.

$$\min_{\theta} f(\theta) = \min_{\theta} \frac{1}{2} \sum_{j}^{n} r_j^2(\theta) \tag{21}$$

The resolution of the minimisation problem given by Equation (21) translates into solving the system of equations for the first-order optimality condition:

$$\frac{\partial f(\theta)}{\partial \theta_i} = 0, \;\; i = 1..m. \tag{22}$$

Here, *m* takes the value of 2 if *a* is set to unity, and 3 otherwise. The NL2SOL method proposed by Dennis et al. was used as the solver [22]. This is a modified version of the Gauss–

Newton (GN) method shown in Equation (23), where J is the Jacobian matrix, and $\Delta\theta = \theta_{k+1} - \theta_k$ is the difference between the current and next iterations. In the GN method, the Hessian matrix of $f(\theta)$: $H = J_k^T J_k + \sum_{j=1}^{n} r_j(\theta_k) H(r_{j(\theta_k)})$ is approximated by $J_k^T J_k$, where $H(r_{j(\theta_k)})$ represents the Hessian matrix of the residual term r_j with respect to parameter θ. The method proposed by Dennis et al. [22] consists of an augmentation of this Hessian to include the effects of the terms neglected in the GN method. Furthermore, the method utilises a trust-region method to determine the optimal step length, and it can choose whether augmentation to the Hessian is necessary because in some cases, the GN method will exhibit better performance. The Jacobian was computed using finite differences with a step size of 0.001 relative to each parameter. For convergence, the relative objective function reduction of a full Newton step (no damping of the step through the trust-region method) was compared with the convergence criterion $\varepsilon = 10^{-3}$. This reduction was relative to the minimal actual value of the objective function between the current and previous iteration results.

$$J_k^T J_k \Delta\theta = -{J_k}^T \vec{r}_k \tag{23}$$

It is necessary for the model to run automatically with the parameters passed by the optimisation solver and return the residuals at the end of the simulation, which is achieved with C-shell scripting. This is performed in conjunction with a Fluent journal file to automate the execution of the CFD model. The first step is the generation of the UDF source files with the current erosion parameters. Then, the CFD model is launched with the journal file, the UDFs are compiled, and the simulation is started from a converged steady-state solution and advanced with the prescribed time step for the corresponding erosion time. At the end of the simulation, the erosion profile is printed to a file, namely a profile of the radius of the sample along the axial direction. Because the resolution of the model is not necessarily equal to that of the experimental erosion profile, interpolation of the former into the latter was performed using a Python script based on the NumPy library to calculate the residuals. Each model run used a separate directory, in which the end simulation results were also stored. CFD simulations were conducted without a graphical output and in parallel mode with up to four nodes to reduce the simulation time. One iteration of the NL2SOL solver requires one full CFD model run. Additionally, the gradients were computed numerically via forward differences; therefore, each iteration requires $m + 1$ simulations for computation, where m is the number of parameters being determined. Moreover, model failure, that is, the premature ending of the simulation is

communicated to the optimisation software in a special way by passing very large residuals to discourage exploration of the solver in this region of the parameter space. Model failure is generally associated with poor meshing issues, which is related to a combination of erosion parameters that results in an excessively high erosion rate.

2.4 Test-problem

A test problem was employed to study the behaviour of the identification method and determine the best choice of solver. The test problem consisted of arbitrarily choosing erosion parameters and constructing artificial experimental data using model prediction and adding artificial noise. Noise was obtained by drawing random numbers from a normal distribution with a zero mean and a given standard deviation. MATLAB's *normrnd* command was used with a standard deviation $\sigma = 10^{-3}mm$. Notably, when the experimental errors are independent and normally distributed, the least-squares solution is also the maximum likelihood solution. This justifies the chosen design of the artificial experiments, particularly because experimental errors are typically normally distributed as a consequence of the central limit theorem [23].

In the test problem, the real solution was known beforehand; thus, the assessment of the solution was straightforward. However, this information was not used to solve this problem. Multiple random initial points were employed to sort out convergence to local minima. If different solutions were encountered, they were discriminated based on the minimal value of the objective function.

Furthermore, the standard deviation of the constructed experimental data was known; therefore, a chi-square (χ^2) test was used to assess the goodness-of-fit provided by the solution. The observed χ^2_{obs} provides a measurement of the misfit between the experimental data and model, as defined in Equation (24). Under the hypothesis used in the least-squares problem, that is, an uncorrelated, normally distributed error with standard deviation σ, this variable is chi-square distributed with $\nu = n - m$ degrees of freedom [23]. For a large ν, at a level of significance $\alpha = 0.05$, χ^2_{obs} must lie in the interval given by Equation (25) if the model parameter θ represents the experiment. This was used to check the statistical acceptability of the solutions.

$$\chi^2_{obs} = \sum_{i=1}^{\mathrm{n}} \frac{\left(y_i(\theta) - y_{i,exp}\right)^2}{\sigma^2} \tag{24}$$

$$\frac{\left(\sqrt{2\nu - 1} - 1.96\right)^2}{2} \leq \chi^2_{obs} \leq \frac{\left(\sqrt{2\nu - 1} + 1.96\right)^2}{2} \tag{25}$$

Moreover, a plot of the residuals scaled by the standard deviation exhibits no clear tendencies, and they appear to be randomly distributed around zero.

In Equation (24), $y_{i,exp}$ are the values obtained from the superposition of the noise with the simulated radii, and σ is the standard deviation of the noise. With this approach, the behaviour of the problem with different configurations was studied: both a two-parameter erosion rate, obtained by fixing parameter a to 1, ($m = 2$) and a three-parameter rate ($m = 3$) were considered for the noisy generated profiles. Furthermore, an analysis of the exact problem, that is, no noise added to the data, was also conducted, where the chi-square test was not applied because the data had no errors.

For the test problem, a refractory with a radius of 10 mm and an immersion length of 57 mm was considered. The clearance to the crucible bottom was 20 mm, and the crucible radius was 32.5 mm. The slag viscosity and density were 0.6186 Pa · s and 2589 kg/m3, respectively. The Taylor number was 412, which was well below the critical Taylor number of 5231 calculated from DiPrima et al. [13]. Additionally, the Reynolds number with the gap width as the characteristic length is 19.7. Figure 7 shows the simulated flow field for this setup. Here, a typical CC flow was observed in the annular region, where the velocity magnitude decreased from the prescribed rotational speed at the inner cylinder to zero at the crucible wall.

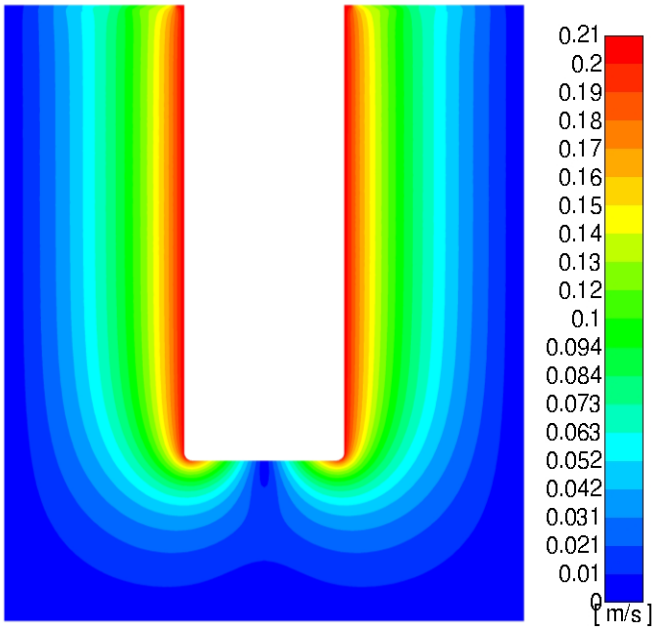

Figure 7. Velocity contours of the simulated test-problem

Figure 8 (a) shows a comparison of the analytical CC solution (Equation (2)) with our simulation results at two different axial positions: at half the cylinder length and near the sample tip. It is evident that the velocity magnitude is well predicted by the CC solution at the half-length line, with an average relative error of 0.2%, whereas the flow field deviates from the prediction toward the end of the sample. The velocity gradient at the refractory wall results in the WSS distribution shown Figure 8 (b); the axial coordinate begins at the slag/atmosphere interface and increases toward the tip of the sample. The WSS is the variable of interest that dominates the erosion process, according to Equation (1). Additionally, in this figure, the theoretical CC-WSS was computed from the analytical solution given in Equation (26). The simulated WSS deviated from the analytical values more noticeably near the slag/atmosphere interface, where the no-shear boundary condition was imposed, and close to the sample tip, where these stresses were larger.

$$\tau = 2\mu\Omega_1\left(\frac{1-\mu_\Omega}{1-\eta^2}\right) \tag{26}$$

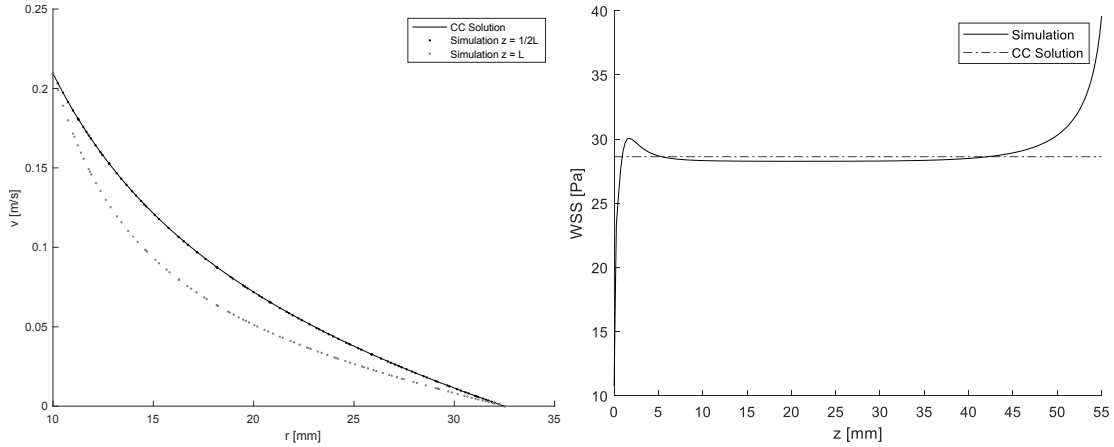

(a) (b)

Figure 8. Velocity magnitude at different axial positions in the annular gap (a). Wall shear stress profile (b)

3. Results and discussion

3.1 Results of test-problem

The inverse problem was conducted with the following choice of erosion parameters: $\theta = (k_d, \tau_c, a)^T = (2 \cdot 10^{-9} m \text{ Pa}^{-1} \text{ s}^{-1}, 5\ Pa, 1)$, and the erosion time was 30 min.

Simulation with the chosen parameters for 30 min of flowtime permits the computation of our erosion profile, which is shown in Figure 9. The continuous line represents the model profile used in the exact problem, and the scatter plot represents the solution with random noise added to the data. A grid independence test was conducted, where refining the mesh from 20307 to 81228 elements only led to a change of 1.3% on average in the WSS distribution; therefore, the coarser mesh was chosen. Furthermore, a time step of 1 s was used for the simulation, and the independence of this choice was checked by performing simulations with a time step of 0.1 s. The predicted erosion profile changed by 0.001% when the average radius of the sample was considered. Moreover, simulations comparing the multiphase model were conducted, where the surface-tension effects were considered as described in our previous study [24]. However, this approach requires significantly smaller time steps for the stability of the Volume of Fluid solver. Additionally, the results of the single-phase model, where the slag/atmosphere interface is modelled as a no-shear boundary, are in good qualitative agreement with those of the multiphase simulation.

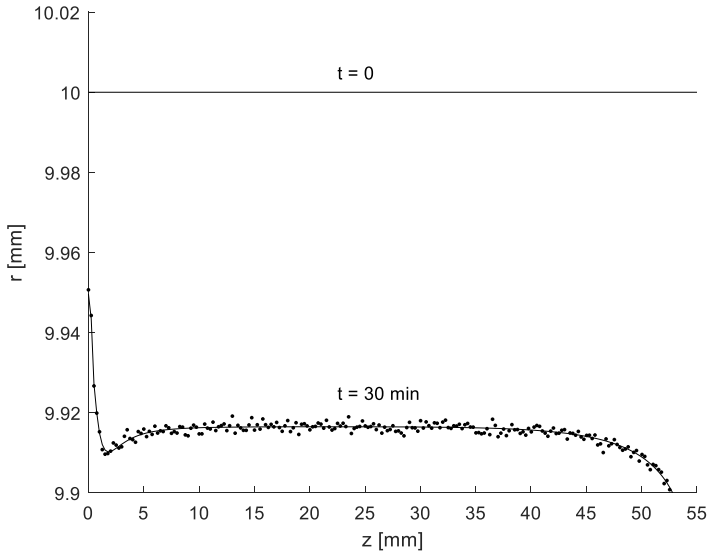

Figure 9. Erosion profile (exact) and noisy data

3.1.1 Exact problem, *m = 2*

The first configuration that was studied was the simplest, where a two-parameter erosion rate was considered by fixing the exponent a to 1, and no artificial noise was added to the simulated profile. The solution of five multiple random starts is summarised in Table 1, where f represents half of the sum of squares of residuals. For the exact problem at the optimum (θ^*), $f(\theta^*)$ is 0.

Table 1. Solutions of exact problem with *m* = 2

	f	k_d (m/s)	τ_c (Pa)	$det(J^T J)$
1	4.00E-22	2.00E-9	5.00	6.55
2	4.50E-22	2.00E-9	5.00	6.56
3	4.50E-22	2.00E-9	5.00	6.56
4	5.00E-22	2.00E-9	5.00	6.59
5	8.35E-22	2.00E-9	5.00	6.54

In all cases, the solution was the true solution with very small values of the objective function, and changes in these values did not affect the parameters, at least in the first five decimals. In most cases, convergence occurs owing to the absolute convergence criterion. Additionally, the determinant of the approximated Hessian matrix is shown in this table; the determinant is similar for all solutions and is indicative of nonsingular matrices. Furthermore,

the appropriateness of the NLS2SOL solver was verified, which is an ideal outcome, owing to the quadratic convergence of this gradient-based solver.

3.1.2 Exact problem, *m = 3*

Here, a three-parameter problem and an exact simulated profile were employed. The results for the inverse problem are presented in Table 2.

Table 2. Solutions of exact problem with *m* = 3

	f	k_d $(m/(s\,Pa^a))$	τ_c (Pa)	a	$det(J^TJ)$
1	1.80E-21	2.00E-9	5.00	1.00	4.76E-10
2	5.75E-21	2.00E-9	5.00	1.00	5.09E-10
3	6.60E-21	2.00E-9	5.00	1.00	5.05E-10
4	5.78E-13	9.00E-10	0.005	1.18	9.24E-05
5	5.79E-13	9.00E-10	0.000	1.18	8.81E-05

The first three solutions corresponded to the exact solution, whereas solutions 4 and 5 were different and corresponded to local subminima based on the larger value of the objective function. This highlights the necessity of using multiple random initial points for the inverse calculation. Notably, the determinant of the approximated Hessian matrices were close to zero, and the matrices were close to singular. Aster et al. [23] claimed that in practical cases, this is indicative of an ill-posed problem. In this case, the true solution was found; however, the situation with noisy data will be proven to be different.

3.1.3 Artificial experimental problem, *m = 2*

For these experiments, random noise was added to the simulated profile, as explained in Section 2.4, and the erosion parameters were calculated with a fixed to 1.0. With a known standard deviation σ of random noise, the least-squares problem was transformed such that the residuals were scaled by the standard deviation, as follows:

$$r = \frac{y_i - y_{exp,i}}{\sigma}. \tag{27}$$

The value of the objective function f now represents half of the sum of the squared scaled residuals, and $\chi^2_{obs} = 2f$. The solutions are listed in Table 3.

Table 3. Solutions with artificial erosion profile with $m = 2$

	f	k_d (m/s)	τ_c (Pa)	χ^2_{obs}	$det(J^T J)$
1	101.4	2.0046E-9	5.10	202.7	6.5
2	101.4	2.0049E-9	5.10	202.7	6.6
3	101.4	2.0046E-9	5.10	202.7	6.6
4	101.4	2.0051E-9	5.10	202.7	6.6
5	101.4	2.0046E-9	5.10	202.7	6.5

All solutions with the five random starting points were the same and were close to the parameters used for the design of the problem with errors of 0.2% and 2% for k_d and τ_c, respectively. The calculated interval for χ^2_{obs} using Equation (25) was [177.6 259.2], and the reported values lie within this interval. In all cases, the determinant of the Hessian matrix was similar to those presented in Table 1. This was expected because these values are only dependent on the model itself, and the experimental data has no influence on them. Moreover, this matrix was nonsingular, and unique solutions were obtained. In the Figure 10, the scaled residuals are shown, and they appear randomly distributed with no apparent trends in their distribution.

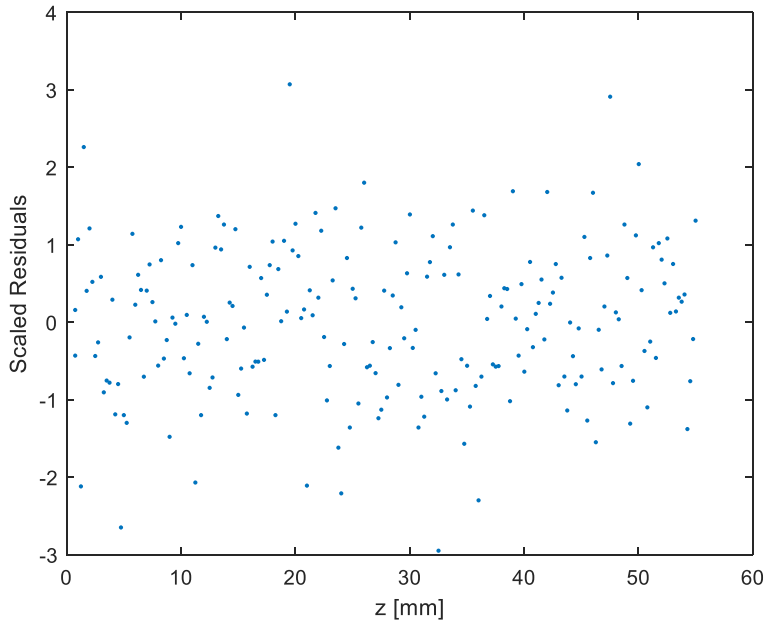

Figure 10. Scaled residuals of the solution along the axial coordinate

3.1.3 Artificial experimental problem, *m = 3*:

The same problem was attempted with the power law of the excess shear stress; the results are shown in Table 4 for five different starting points.

Table 4. Solutions with artificial erosion profile and m = 3

	f	k_d $(m/(s\,Pa^a))$	τ_c (Pa)	a	χ^2_{obs}	$\dot{\varepsilon_{CC}}$ (m/s)	$det(J^TJ)$
1	101.4	2.77E-9	7.16	0.92	202.7	4.715E-8	3.48E-10
2	101.7	1.30E-9	2.39	1.10	203.5	4.715E-8	1.49E-09
3	101.9	1.16E-9	1.65	1.13	203.8	4.715E-8	2.02E-09
4	102.0	4.07E-9	9.65	0.83	204.1	4.715E-8	3.18E-10
5	1E14	6.07E-9	8.73	1.43	2E14	4.310E-7	-

In this case, no unique solution was obtained; similar values of the objective function led to different solutions, and none corresponded to the parameters used in the design of the test problem. Moreover, from a statistical point of view, all solutions except solution 5 are acceptable because the values of χ^2_{obs} lie within the calculated interval of [176.7, 258.1]. These solutions all produced the same characteristic erosion rate, which was calculated using the solution parameters and analytical CC-WSS. This is characteristic of an ill-posed problem. This was also noticeable in the determinants of the Hessian matrices, which were indicative of nearly singular matrices. A possible explanation for this behaviour is the relatively low variation in the WSS distribution along the axial coordinate resulting from the CC flow field. This is easily understood when a constant WSS distribution is considered. Then, an infinite combination of parameters would produce the same erosion rate, and therefore, the same erosion profile. Solution number 5 is a case of divergence owing to the repetitive failure of the model, where large residuals are passed.

3.1.4 Artificial experimental problem, m = 3, N_{exp} = 2:

Finally, it is feasible to perform multiple experiments with different erosion times. Here, the determination was attempted using combined data from two experiments: one with an erosion time of 30 min and the other of 15 min, as shown in Table 5.

Table 5. Solutions with artificial erosion profile for m = 3 using two experiments (t = 15 min and t = 30 min erosion)

	f	k_d $(m/(s\,Pa^a))$	τ_c (Pa)	a	χ^2_{obs}	$\dot{\varepsilon_{CC}}$ (m/s)	$det(J^TJ)$
1	204.7	3.24E-9	8.19	0.89	409.5	4.713E-8	6.25E-10
2	204.7	3.28E-9	8.26	0.88	409.5	4.714E-8	6.33E-10
3	204.8	3.53E-9	8.74	0.87	409.6	4.713E-8	5.64E-10
4	206.6	8.82E-10	0.00	1.19	413.2	4.713E-8	2.33E-04

Convergence to the design optimum was not achieved, and the multimodality of the problem was evident and explained by the Hessian matrix determinant. Repetition of the experiment, that is, using the same erosion time with a new set of random errors, also led to the same conclusions, shown in Table 6.

Table 6. Solutions of artificial erosion profile for m = 3 and two experiments

	f	k_d $(m/(s\,Pa^a))$	τ_c (Pa)	a	χ^2_{obs}	$\dot{\varepsilon_{CC}}$ (m/s)	$det(J^TJ)$
1	228.0	2.55E-9	6.72	0.95	456.1	4.722E-8	3.58E-10
2	228.2	3.06E-9	7.88	0.90	456.2	4.722E-8	3.42E-10
3	229.3	1.28E-9	2.37	1.10	458.5	4.722E-8	1.56E-09
4	230.6	8.75E-10	0.005	1.19	461.1	4.721E-8	1.14E-06

In both cases, the calculated interval for χ^2_{obs} was [378.6 494.2], and all solutions lie within it.

3.2 Result from real experiments

The experimental setup consisted of an alumina coarse-grained refractory material. The slag was in the CaO-Al2O3-SiO2-MgO system with weight percentages of 32.42%, 11.16%, 49.56%, and 6.86% for calcia, alumina, silica, and magnesia, respectively. The experimental temperature was 1450 °C, and the slag density and viscosity were 2595.2 kg/m3 and 1.0187 Pas, respectively. The rotational speed was 200 rpm with an erosion time of 30 min. All the other experimental parameters were as defined in Section 2.4. The results for the five initial random points are presented in Table 7. The information from the test problem already indicated the infeasibility of inverse calculation with $m = 3$; therefore, we attempted the determination with a at a fixed value of 1.

Table 7. Solutions with real experimental erosion profile

	f	k_d $(m/(s\,Pa^a))$	τ_c (Pa)	$\dot{\varepsilon_{CC}}$ (m/s)	$det(J^TJ)$
1	3.159E-7	7.220E-9	29.58	1.771E-7	7.25E8
2	3.159E-7	7.224E-9	29.60	1.771E-7	5.90E3
3	3.159E-7	7.205E-9	29.50	1.773E-7	2.02E3
4	3.161E-7	7.304E-9	29.95	1.765E-7	3.77E9
5	3.166E-7	7.380E-9	30.24	1.762E-7	6.48E8

The results are unique and differed only in decimals, owing to the premature convergence of the solver. The solution is shown graphically in Figure 11, where the fit between the model and experiment can be estimated. The largest discrepancies between the model and experimental data were observed in the slag/atmosphere near z below approximately 5 mm. This may have been caused by parameters k_d and τ_c not being constant over the entire specimen length. Lower erodibility was expected close to the slag surface because this region might be less affected by pre-corrosion. This effect could be cancelled by evaluating the profile for $z > 5\ mm$ only. Notably, the determinants of the Hessian matrices were indicative of a nonsingular matrix (see Table 7).

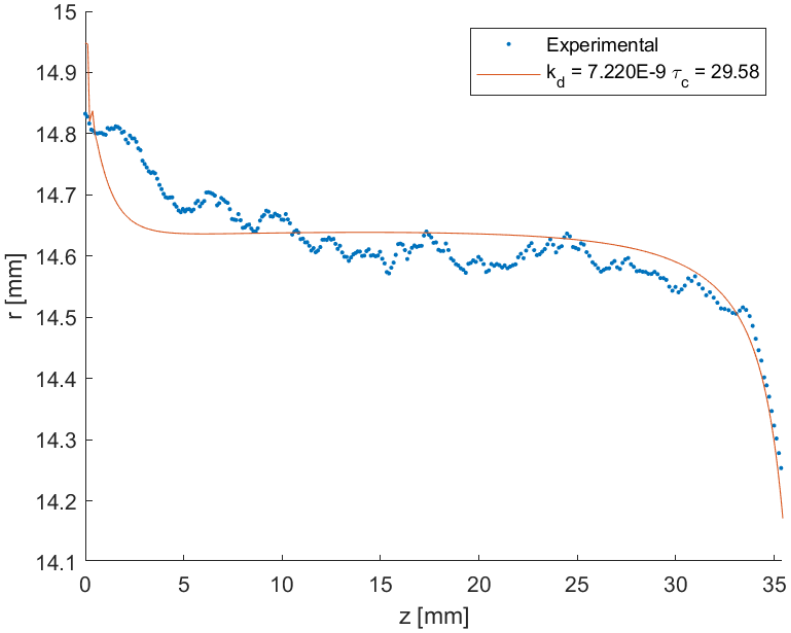

Figure 11. Results of inverse calculation of parameters for real experimental erosion profile

The standard deviation was not known when the real experimental erosion profiles were used. One approach is to approximate the standard deviation from the residuals, as per Equation (28). This incurs a statistical cost, and with this standard deviation, the solution always passes the chi-square test; therefore, other methods for statistical assessment are necessary.

$$s = \sqrt{\frac{\sum_i^n (y_i(\theta) - y_{i,exp})^2}{\nu}} \tag{28}$$

Confidence intervals and regions were calculated to evaluate the solutions. Here, a nonlinear problem was considered, but the calculations for confidence intervals and regions were based on the linearisation of the model, as described in the literature [23,25]. This

approximation does not necessarily lead to a good estimation of such intervals or regions; therefore, caution must be exercised. Other methods for calculating confidence regions, not based on linearisation, include the F-test, log-likelihood method, and Monte Carlo techniques. However, these methods require many more function evaluations, which translates to significant simulation effort. Linearisation was performed with the approximated Hessian matrix, which was computed using the Jacobian matrix calculated with difference approximations at the optimum solution ($H = J(\theta^*)^T J(\theta^*)$). The covariance matrix was approximated using Equation (29), which was reported by Donaldson and Schnabel as the best linearisation approach [25] in terms of results and computation effort. The confidence intervals were calculated based on a t-student distribution with a confidence level of 95%, as shown in Equation (30), with s calculated from Equation (28):

$$Cov(\theta) = s^2 (J^T J)^{-1} \tag{29}$$

$$\theta \pm t_{\nu,0.975}\, diag\big(Cov(\theta)\big)^{\frac{1}{2}}. \tag{30}$$

Here, $diag\big(Cov(\theta)\big)^{\frac{1}{2}}$ refers to a vector of m components obtained from the diagonal of the covariance matrix by taking the square root of each element.

The difference between the confidence intervals and regions is that the regions allow for correlations between the parameters. When using linearisation, the shape of the regions is elliptical, centred on the solution, as given by Equation (31). The confidence level is determined from the χ^2 distribution with m degrees of freedom, as expressed in Equation (32), for which a 95% confidence is employed.

$$(\theta - \theta^*)^T s^{-2} J^T J (\theta - \theta^*) \leq \Delta^2 \tag{31}$$

$$\Delta^2 = F^{-1}_{\chi^2,m}(0.95) \tag{32}$$

The Hessian and covariance matrices for the first solution presented in Table 7 are given as follows:

$$H = \begin{pmatrix} 9.153 \cdot 10^{11} & -123.403 \\ -123.403 & 7.927 \cdot 10^{-4} \end{pmatrix};\ Cov = \begin{pmatrix} 2.422 \cdot 10^{-21} & 3.771 \cdot 10^{-16} \\ 3.771 \cdot 10^{-16} & 2.797 \cdot 10^{-6} \end{pmatrix}.$$

The confidence intervals are

$$7.123 \cdot 10^{-9} \leq k_d \leq 7.317 \cdot 10^{-9},$$

$$29.579 \leq \tau_c \leq 29.586.$$

The confidence intervals were narrow for both parameters. The confidence region is plotted in Figure 12 with the box defined by the confidence intervals. It can be observed that both the region and intervals are similar, but the region is slightly larger.

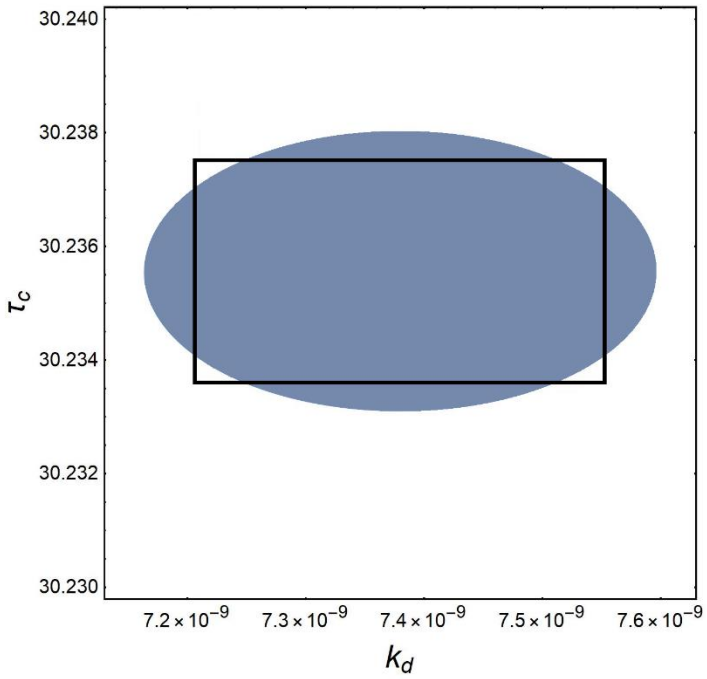

Figure 12. Confidence regions (shaded ellipsoidal area) and confidence region (box) for solution 1

The low inclination with respect to the parameter axis k_d can be observed from the coefficient of correlation between the parameters.

$$\rho_{k_d,\tau_c} = \frac{Cov(k_d, \tau_c)}{\sqrt{Var(k_d)Var(\tau_c)}} = 0.0046$$

Table 8 shows confidence intervals and parameter correlation for all solutions presented in Table 7, where the lower and upper bounds of the intervals are denoted with subscripts L and U, respectively. It can be observed that similar solutions, such as solutions 1 and 2, produce different confidence regions and parameter correlation. Therefore the reliability of the linearisation approach for the estimation of parameter confidence is not ensured and should be analysed for each individual case.

Table 8. Confidence intervals and correlation coefficients for all solutions

	$\bar{k}_{d_L}$	$\bar{k}_d$	$\bar{k}_{d_U}$	$\bar{\tau}_{c_L}$	$\bar{\tau}_c$	$\bar{\tau}_{c_U}$	ρ_{k_d,τ_c}
1	7.12E-9	7.22E-9	7.32E-9	29.58	29.58	25.59	0.0046
2	7.01E-9	7.22E-9	7.43E-9	27.99	29.60	31.21	0.9433
3	6.66E-9	7.21E-9	7.75E-9	27.67	29.50	31.34	0.9817
4	7.24E-9	7.30E-9	7.37E-9	29.70	29.95	30.20	-1.0000
5	7.21E-9	7.38E-9	7.55E-9	30.23	30.24	30.24	0.0052

4. Conclusions

This study developed and tested a method for the inverse calculation of the erosion parameters of refractory materials in liquid slags. Investigations with a test problem proved that the problem is well suited for gradient-based solvers, and the NL2SOL solver can be employed. With the exact problem, identification of the true erosion parameters is achievable for both $m = 3$ and $m = 2$; however, the determinants of the Hessian matrix for $m = 3$ proves the difficulties associated with this approach.

An analysis with noisy generated erosion profiles revealed an ill-conditioning of the problem for $m = 3$. In these cases, multiple solutions were obtained and were equally acceptable; thus, erosion parameters could not be uniquely identified. This may be a result of the low variation in the WSS distribution along the axial coordinate. These results highlight the irrelevance of exact problems in the analysis of inverse-problem capabilities. The conclusions are confirmed by the determinant values of the Hessian matrices, which were close to singular for all cases with $m = 3$.

For the case of $m = 2$, where parameter a is set to 1, unambiguous identification was possible. However, local subminima were also encountered in the solution process, which suggest the necessity for using multiple random starting points. The results for the test problem were validated using the chi-square test.

Finally, the methodology was successfully applied to real experiments, in which the erosion parameters for a linear erosion rate could be identified. Confidence regions and intervals were also calculated; however, their reliability was not guaranteed because similar solutions produced dissimilar confidence regions. The methodology developed in this study is suitable for the inverse calculation of erosion parameters for refractory erosion in liquid slags and can guide further investigations of refractory erosion.

Future investigations might concern the application of the method for different material/ slag systems. Further, the evaluation with erosion profiles obtained from service conditions is

of interest but it presents further challenges associated to the resolution of the flow-field for the given processes, where turbulence and other process associated phenomena not included in this work may also be relevant.

Acknowledgements

The authors gratefully acknowledge the funding support of K1-MET GmbH, metallurgical competence center. The research programme of the K1-MET competence center is supported by COMET (Competence Center for Excellent Technologies), the Austrian programme for competence centers. COMET is funded by the Federal Ministry for Climate Action, Environment, Energy, Mobility, Innovation and Technology, the Federal Ministry for Digital and Economic Affairs, the Federal States of Upper Austria, Tyrol and Styria as well as the Styrian Business Promotion Agency (SFG) and the Standortagentur Tyrol. Furthermore, we thank Upper Austrian Research GmbH for the continuous support. In addition to the public funding from COMET, this research project is partially financed by the scientific partners the Chair of Ceramics of the Montanuniversität Leoben and the industrial partners voelstalpine Stahl GmbH, RHI Magnesita GmbH and Böhler Edelstahl GmbH.

Data Availability Statement

The data that support the findings of this study are available on reasonable request from the corresponding author.

References

[1] Vollmann S, Harmuth H. CFD simulation of mass transfer coefficients relevant for refractory wear. Interceram: Int Ceram Rev/Refractories 2012:19–21.

[2] Guzmán AM, Martínez DI, González R. Corrosion–erosion wear of refractory bricks in glass furnaces. Engineering Failure Analysis 2014;46:188–95. https://doi.org/10.1016/j.engfailanal.2014.09.003.

[3] Partheniades E. Erosion and Deposition of Cohesive Soils. Journal of the Hydraulics Division 1965;91:105–39. https://doi.org/10.1061/JYCEAJ.0001165.

[4] Al-Madhhachi A-ST, Hanson GJ, Fox GA, Tyagi AK, Bulut R. Measuring Soil Erodibility Using a Laboratory "Mini" JET. Transactions of the ASABE 2013;56:901–10. https://doi.org/10.13031/trans.56.9742.

[5] Hanson GJ, Simon A. Erodibility of cohesive streambeds in the loess area of the midwestern USA. Hydrological Processes 2001;15:23–38. https://doi.org/10.1002/hyp.149.

[6] Weidner K, Petrie J, Diplas P, Nam S, Gutierrez M, Ellenberg M. Numerical Simulation of Jet Test and Associated Soil Erosion, Paris: 2012.

[7] G. J. Hanson, K. R. Cook. APPARATUS, TEST PROCEDURES, AND ANALYTICAL METHODS TO MEASURE SOIL ERODIBILITY IN SITU. Applied Engineering in Agriculture 2004;20:455–62. https://doi.org/10.13031/2013.16492.

[8] Karmaker T, Das R. Estimation of riverbank soil erodibility parameters using genetic algorithm. Sādhanā 2017;42:1953–63. https://doi.org/10.1007/s12046-017-0733-6.

[9] Wan CF, Fell R. Laboratory tests on the rate of piping erosion of soils in embankment dams. Geotechnical Testing Journal 2004;27:295–303. https://doi.org/10.1520/gtj11903.

[10] Briaud JL, Ting FCK, Chen HC, Cao Y, Han SW, Kwak KW. Erosion Function Apparatus for Scour Rate Predictions. Journal of Geotechnical and Geoenvironmental Engineering 2001;127:105–13. https://doi.org/10.1061/(ASCE)1090-0241(2001)127:2(105).

[11] Kircher V, Burhanuddin, Harmuth H. Design, operation and evaluation of an improved refractory wear testing technique. Measurement 2021;178:109429. https://doi.org/10.1016/j.measurement.2021.109429.

[12] Taylor GI. Stability of a Viscous Liquid Contained between Two Rotating Cylinders. Philosophical Transactions of the Royal Society A: Mathematical, Physical and Engineering Sciences 1923;223:289–343. https://doi.org/10.1098/rsta.1923.0008.

[13] DiPrima RC, Eagles PM, Ng BS. The effect of radius ratio on the stability of Couette flow and Taylor vortex flow. Physics of Fluids 1984;27:2403. https://doi.org/10.1063/1.864544.

[14] Astill KN. Studies of the developing flow between concentric cylinders with the inner cylinder rotating. Journal of Heat Transfer 1964;86:383–91. https://doi.org/10.1115/1.3688703.

[15] Chandrasekhar S. Hydrodynamic and Hydromagnetic Stability. New York: Dover Publications, Inc.; 1961. https://doi.org/10.1017/S0022112062210592.

[16] Andereck CD, Liu SS, Swinney HL. Flow regimes in a circular Couette system with independently rotating cylinders. Journal of Fluid Mechanics 1986;164:155–83. https://doi.org/10.1017/S0022112086002513.

[17] Ansys ®. Ansys Fluent 12.0 Theory Guide 2009.

[18] Demirdžić I, Perić M. Space conservation law in finite volume calculations of fluid flow. International Journal for Numerical Methods in Fluids 1988;8:1037–50. https://doi.org/10.1002/fld.1650080906.

[19] ANSYS I. ANSYS Fluent User's Guide 2017.

[20] Versteeg H, Malalasekera M. An introduction to computational fluid dynamics: The finite volume method, 2nd Edition. Pearson; 2007.

[21] Ferziger JH, Peric M, Street RL. Computational methods for fluid dynamics, Fourth Edition. Springer; 2020.

[22] Dennis JE, Gay DM, Walsh RE. An Adaptive Nonlinear Least-Squares Algorithm. ACM Transactions on Mathematical Software 1981;7:348–68. https://doi.org/10.1145/355958.355965.

[23] Aster RC, Borchers B, Thurber CH. Parameter estimation and inverse problems. Elsevier Inc.; 2013. https://doi.org/10.1016/C2009-0-61134-X.

[24] Guarco J, Harmuth H, Vollmann S. Method for determination of mass transfer coefficients for dissolution of dense ceramics in liquid slags. International Journal of Heat and Mass Transfer 2022;186:122494. https://doi.org/10.1016/j.ijheatmasstransfer.2021.122494.

[25] Donaldson JR, Schnabel RB. Computational experience with confidence regions and confidence intervals for nonlinear least squares. Technometrics 1987;29:67–82. https://doi.org/10.1080/00401706.1987.10488184.